Ammonia effects on hydrogen embrittlement mitigation and induction -Experiment and theoretical understanding of the mechanisms-

張, 楠

出版情報：Kyushu University, 2022, 博士（工学）, 課程博士
バージョン：
権利関係：

Ammonia effects on hydrogen embrittlement mitigation and induction
-Experiment and theoretical understanding of the mechanisms-

Nan Zhang

Department of Mechanical Engineering
Graduate School of Engineering
Kyushu University

Ammonia effects on hydrogen embrittlement mitigation and induction -Experiment and theoretical understanding of the mechanisms-

by

Nan Zhang

Department of Mechanical Engineering
Graduate School of Engineering
Kyushu University

Dissertation Committee

Prof. Masanobu Kubota, Supervisor and Examiner
International Institute for Carbon-Neutral Energy Research (WPI-I2CNER),
Kyushu University
Assoc. Prof. Aleksandar Staykov, Co-Examiner
International Institute for Carbon-Neutral Energy Research (WPI-I2CNER),
Kyushu University
Prof. Shigeru Hamada, Co-Examiner
Graduate School of Engineering, Kyushu University
Assoc. Prof. Motonori Watanabe, Co-Examiner
International Institute for Carbon-Neutral Energy Research (WPI-I2CNER),
Kyushu University

Fukuoka, Japan, July 2022

Abstract

The objective of this study is to obtain a mechanistic insight into the NH_3 effects on hydrogen embrittlement (HE) in order to enable the safety of NH_3 utilization for carbon-neutral purposes. Transitioning to a hydrogen-powered society is one of the promising directions to decrease carbon dioxide emissions. However, steels and alloys used for hydrogen gas containment systems can suffer from hydrogen embrittlement, which is the degradation of material strength due to the hydrogen. Ammonia (NH_3) has been considered a hydrogen carrier and non-CO_2 fuel. It is expected that NH_3 will play an essential role in a carbon-neutral society.

In this study, fracture toughness tests of SCM440 low-alloy steel were carried out in H_2 and NH_3-added H_2 gases to characterize the HE mitigation effect by NH_3. In addition, the experiments in the N_2 and NH_3-added N_2 gases were also performed to examine the interaction of NH_3 with the Fe surface. As a result, we determined two NH_3 effects conflicting with each other, which are HE mitigation and HE induction. Regarding the HE mitigation effect, it was more pronounced by increasing the NH_3 concentration. Regarding the HE induction effect, an inverse NH_3 concentration dependence that the HE was reduced by the increase in the NH_3 concentration was found. The mechanisms were elucidated by theoretical considerations using the density functional theory (DFT). For the Fe (110) surface, the NH_3 adsorption rate, NH_3 decomposition rate, H_2 dissociation rate, and hydrogen atom coverage were calculated.

In chapter 1, the background and objective of this thesis were described. First, the role of NH_3 in the recent world energy situation was explained following introduction of the physical properties of NH_3. Second, general trends in the HE during the fracture toughness test and state-of-the-arts of the mitigation of HE by impurities mixed in hydrogen gas were introduced. Third, applications of DFT calculations regarding the interaction of gaseous species and solid surfaces were described. Finally, the motivation and objective of this study were identified.

In chapter 2, fracture toughness tests of JIS SCM440 low-alloy steel were conducted in H_2 and 1,000 volume ppm (vppm) or 10,000 vppm NH_3-added H_2 gases. As a result, it was confirmed that NH_3 had a mitigation effect on the HE. According to the

DFT calculations, the NH_3 reaction rate on the Fe (110) surface was 2.77×10^{19} s^{-1} at 11.11% NH_3 coverage, while the H_2 reaction rate on the Fe (110) surface was 5.88×10^{9} s^{-1}. As the result that NH_3 has a significantly higher reaction rate, NH_3 was preferentially adsorbed on the Fe surface. According to the Langmuir adsorption model, when 25.00% of the Fe surface is covered by NH_3, only 0.01% of the Fe surface is available for hydrogen atoms. These are the mechanisms by which NH_3 mitigates the HE.

In chapter 3, fracture toughness tests were conducted in N_2 and 1,000 vppm NH_3 added H_2 gases. In the NH_3-added N_2 gas, a significant reduction in the fracture toughness was found. The cause was determined as HE by examination of the fracture surface. This NH_3 effect of the HE induction was strongly affected by the loading rate. For its expression, a 2×10^{-5} mm/s loading rate, which is extremely low, was required. By comparing the NH_3 adsorption rate coefficient ($k = 3.14 \times 10^{20}$ s^{-1}) with the NH_3 decomposition rate coefficient ($k = 1.36 \times 10^{8}$ s^{-1}), which were obtained by the DFT calculations, it was found that the NH_3 decomposition was a relatively very slow reaction. Therefore, NH_3 induces the HE only if the loading rate is sufficiently low.

In chapter 4, 10,000 vppm NH_3 in N_2 gas was added to the fracture toughness test in order to investigate the NH_3 concentration dependence on the HE induction effect. Interestingly, the HE by NH_3 decomposition diminished as the NH_3 concentration increased. This was opposite to the prediction based on the theoretical result that atomic hydrogen coverage on the Fe surface increased with an increase in the NH_3 concentration. The main reason for this reverse trend was the change in the NH_3 decomposition rate with the NH_3 concentration. The DFT revealed that NH_3 can achieve ($NH_2 \rightarrow NH + H$) following ($NH_3 \rightarrow NH_2 + H$) when the NH_3 concentration was sufficiently low, whereas it can achieve only ($NH_3 \rightarrow NH_2 + H$) when the NH_3 concentration was high because the NH_3 decompositions require vacant sites on the Fe surface. A higher NH_3 concentration limits the NH_3 decomposition resulting in a reduction of the hydrogen supply.

Furthermore, for the NH_3 and H_2 competitive coadsorption on the Fe (110) surface, a kinetic model, which can quantitatively determine the coverage of each species on the Fe surface, was established. It was revealed that the hydrogen atom coverage on the Fe (110) surface was 8.42% for the H_2 + 1,000 vppm NH_3 gas and 15.20% for the H_2 + 10,000 vppm NH_3 gas, if NH_3 can undergo total decomposition. However, the NH_3

decomposition rate decreased as the NH_3 concentration increased resulting in hindering the NH_3-derived hydrogen supply. As a result, the hydrogen atom coverage on the Fe (110) surface was 8.42% for the H_2 + 1,000 vppm NH_3 gas and 4.37% for the H_2 + 10,000 vppm NH_3 gas. This was the reason for the NH_3 concentration dependence on the NH_3 mitigation effect.

In chapter 5, the obtained results of this study were summarized and conclusions listed.

Acknowledgment

This thesis is a summary of the research that I carried out during the doctoral course at the Department of Mechanical Engineering in the Graduate School of Engineering of Kyushu University. There are plenty of impressive memories flashing back to the past three years and there are a lot of people I would like to be grateful for.

First and foremost, I would like to express my deepest and sincerest appreciation to my main supervisor Professor Masanobu Kubota who led me into the Material Science research field, patiently taught me the knowledge, frankly shared your precious experiences, and provided me with extraordinary help and supported me throughout my entire research. This thesis could not be stand up here without you. I am extremely grateful for your faithful education, encourage and the experience I gained during this period will be a great mentor for my future research career. Meanwhile, as a foreigner studying and living in Japan and during this specific pandemic duration since 2020, you always took care of my health and safety and offered your help and kindness all the time, I have no words that can describe my gratitude for my deep heart and I will engrave in mind.

I would like to extend my deeply indebted and appreciation to my co-supervisor Professor Aleksandar Staykov who led me into the chemistry field, taught me a lot about DFT and surface chemistry and catalysis, cheer me up even the darkest time of mine and I would not be able to accomplish this thesis without you. I very much appreciate your kind support and insightful comments during every talk and discussion with you all the time. All of the nice talks with you will be kept in my mind.

I would like to express my deep appreciation to Professor Ryosuke Komoda, who taught me a lot about the knowledge, paper, experiment, presentation, and the fun of research and gave me a lot of insightful advice and suggestions on this research, and gave thoughtful encouragement. I appreciate it that you allow me to use the experiment equipment at Fukuoka University and I had very rewarding experiences because of you.

I am grateful to have received extensive support and help from many people. I would like to express my appreciation to Professor Shigeru Hamada and Professor Motonori Watanabe for giving me insightful comments and advice on this thesis. I would

like to thank technical staff Mr. Katsuya Shimada and Mr. Shoyo Maeda for machining many specimens. I must also thank you for your teaching me how to use machine tools detailly and experience. I am also grateful to technical staff Mr. Takashi Soejima who helped charge specimen hydrogen. I also would like to thank my fellow lab mates Dr. Daisuke Takazaki, Mr. Kazuki Yamada, Ms. Nguyễn Xuân Thi, and everyone in my lab for the discussions and many moments of support.

This work was supported by JST SPRING, Grant Number JPMJSP2136.

This study was supported by the International Institute for Carbon-Neutral Energy Research (WPI-I2CNER), sponsored by the World Premier International Research Center Initiative (WPI), MEXT, Japan. Kyushu University Platform of Inter-transdisciplinary Energy Research (Q-PIT), Japan.

Finally, I would like to thank my family for their grateful support and education. Special thanks go to my parents, who keep on my side forever.

This thesis is dedicated to all of them.

Fukuoka, July 2022

Nan Zhang

Contents

List of Figures

List of Tables

Nomenclature

k	reaction rate coefficient	COD	crack opening displacement
E_a	activation energy	Δa	crack extension
A	pre-exponential factor	J_{IC}	plane-strain fracture toughness
R	universal gas constant	p_T	total environmental gas pressure
T	temperature	V	cross head displacement rate
K_{eq}^{A}	equilibrium constant	$vppm$	volume parts per million
p_A	partial pressure	r_r	rate of reaction
θ_A	fractional occupancy of the adsorption sites		

1 Introduction

1.1 Ammonia and its properties

Ammonia occurs in nature, primarily produced by anaerobic decay of plant and animal matter, and it also has been detected in outer space [1 - 1]. Some plants, mainly legumes, combine with rhizobia to fix atmospheric nitrogen to produce ammonia [1 - 2]. Ammonia has been known by its odor since antiquity. Gaseous ammonia was first isolated in 1774 by the English chemist, Joseph Priestly [1 - 3]. Its composition was determined in 1785 by the French chemist, Claude Louis Berthollet [1 - 4]. The commercial production of ammonia was developed in 1909 by German chemists, Fritz Haber and Carl Bosch, over Fe/Ni catalyst the reaction of nitrogen and hydrogen at high temperatures and pressure. The Nobel Prize in chemistry 1918 was awarded to Fritz Haber for the synthesis of ammonia from its elements and Bosch in 1931[1 - 5]. The fundamental Haber–Bosch process is still in use today.

NH_3 is a compound of nitrogen and hydrogen with chemical formula NH_3. It is a colorless, toxic gas with a pungent noxious odor at room temperature [1 - 6]. NH_3 is an irritant and the irritation increases with concentration; the permissible exposure limit is 25 ppm, and lethal is above 500 ppm [1 - 7]. A solution of NH_3 is alkaline and NH_3 can be used as a cleaner because of dissolves grease [1 - 8]. NH_3 is easily soluble in water and lighter than air. Gaseous NH_3 is neither combustible nor a supporter of combustion [1 - 9]. The properties of NH_3 as shown in the Table. 1.1 [1 - 10].

Table. 1.1 The properties of NH_3 [1 - 10]

Molar mass	Boiling point	Melting point	Water solubility	Density
17.03 g/mol	-33.3 °C	- 77.73 °C	530 g/L (20 °C)	0.73 kg/m^3 (1.013 bar at 15 °C)

The global NH_3 capacity was 176 million metric tons by 2016 [1 - 11]. NH_3 is a key ingredient in fertilizer production and is one of the world's most prolific synthetic chemicals [1 - 12]. Most NH_3 production (about 85%) is directly or indirectly used in agriculture, such as ammonium nitrate or ammonium sulfate. These provide nitrogen to the soil, and NH_3 can be injected directly into the soil as fertilizer. NH_3 is also used in the production of plastics, fibers, explosives, nitric acid, and intermediates in dyes and pharmaceuticals [1 - 13]. NH_3 already had complete production conditions in the world, which provide completely produce.

1.2 Recent world energy situation and ammonia role in the world energy

Before the Covid-19, several world energy scenarios published in 2019 [1 - 14 - 1 - 18] described three feasible paths for transforming the energy sector by 2040 and gave a quantitative outlook to 2060. The development of the past 40 years before 2019 are outlined as below: (1) The global population in 2018 is increased by 77% compared to the level of 4.30 billion in 1978, and the global energy demand surged; (2) Global primary energy consumption has more than doubled from 270.5 Exajoule (EJ, 10^{18} J) in 1978 to 580 EJ in 2018, fossil fuels have always been the main feedstock. In 2018, although the share of fossil fuels in global primary energy consumption was 7% lower than in 1978, the oil and natural gas still accounted for 85% of total primary energy consumption; (3) The CO_2 emission increased from 18.0 billion tonnes (bn tonnes) in 1978 to 33.7 bn tonnes in 2018, the environmental problems are becoming more and more serious.

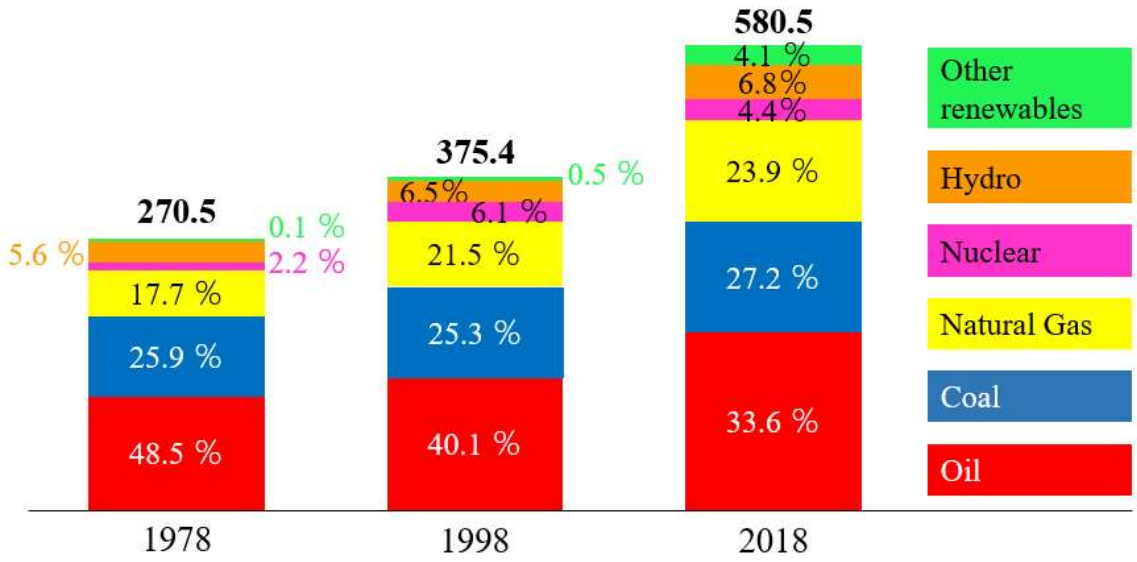

Fig. 1.1 BP Statistical Review of World Energy June 2019 [1 - 17]. Redrawn by the author

As Fig. 1.1 shows, although the renewable energy sources are increasing, the main contents of the global primary energy consumption are still oil, coal, and natural gas. Fossil fuels are non-renewable at the present and produces CO_2. Considering we will run out of fossil fuel one day and the CO_2 has already brought us severe global climate change, the world health organization (WHO) calls climate change the greatest threat to global health in the 21st century [1 - 19-1 - 21]. The impacts of climate change include sea level rise, global warming, and more acidic oceans [1 - 22]. Under the 2015 Paris agreement, nations collectively agreed to keep warming "under 2°C". The USA broke away from this agreement in 2019, however, they have been back to the Paris agreement from January 2021. It is critically important to develop renewable energy for protecting the whole world and our future generations. As Fig. 1.2 shows, if we do nothing, it will bring us more serious environmental problems due to CO_2 emissions.

The Covid-19 pandemic had profound impacts on energy demand in 2020, reducing the global CO_2 emission by 5.2%. However, the world has experienced an extremely rapid

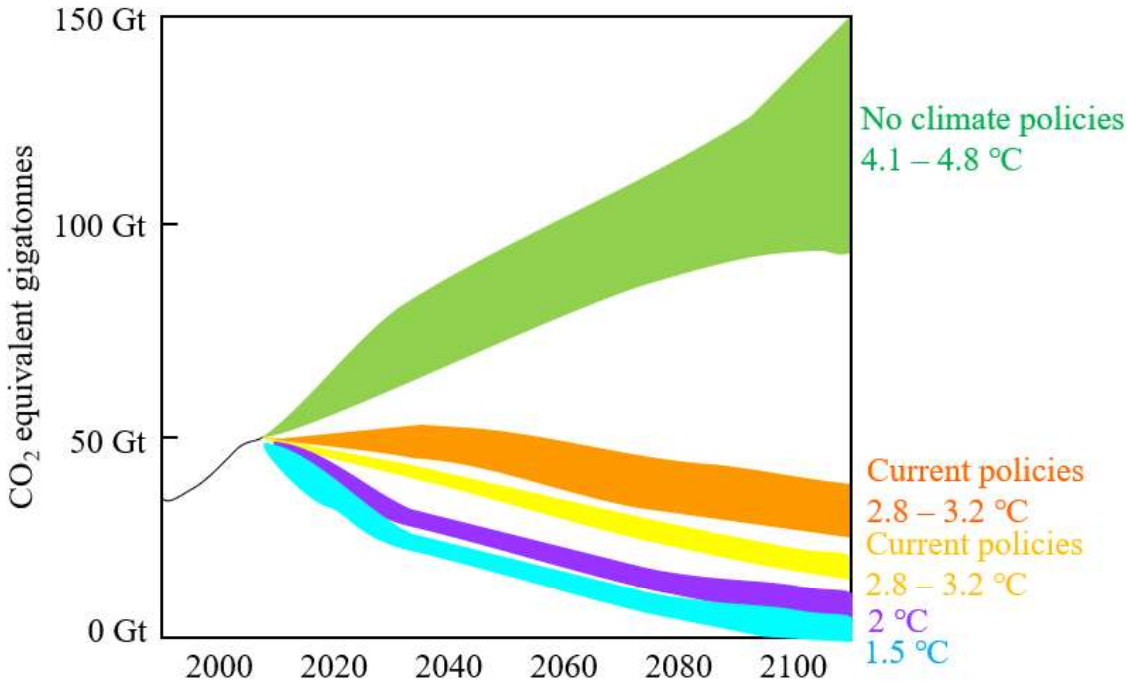

Fig. 1.2 Global greenhouse gas emission pathways [1 - 23]. Redrawn by the author

economic recovery since then, driven by unprecedented fiscal and monetary stimulus [1 - 24]. The recovery in energy demand in 2021 will be exacerbated by worsening environmental and energy market conditions. Coal burning remains at a high level of growth despite the largest ever annual increase in renewable power generation. That puts energy-related CO_2 emissions in 2021 ahead of 2010 as the largest on record. The CO_2 emission in 2021 is about 180 Megattones (Mt) higher than pre-pandemic levels in 2019. Based on the International renewable energy agency data publication, fossil fuels still dominated the world's energy complex [1 - 24]. Considering the fossil fuel-based non-renewable energy infrastructure, and has severe environmental effects, it is imperative to accelerate the establishment of a carbon-neutral society.

Hydrogen is a clean energy source having high energy content (122 kJ/g) [1 - 25] when it is produced in a green way. One of the potential paths to a carbon-neutral economy is hydrogen energy. However, issues associated with hydrogen storage and distribution are currently one of the most serious barriers leading to high cost of H_2 to its implementation. Hence, other indirect storage media storage is needed.

As the previous section mentioned, NH_3 is the most well-known nitrogen feedstock for agriculture or as a refrigerant. It is the second-largest chemical (after sulfuric acid) produced in the world. Recently, NH_3 has been considered as a fuel because of its carbon-free substance, high octane number, and good economic benefits, for example, NH_3 is the cheapest fuel per 100 km driving range [1 - 26]. It is shown that a medium-size hydrogen car converted to NH_3 became more effective per range cost and fuel tank compactness. The reason can be considered as follows: Firstly, NH_3 has a high-octane rate of 110 -130 [1 - 27], thus it is a good fuel for internal combustion engines. Secondly, it can be thermally cracked into hydrogen and nitrogen using low energy, 12% from the higher heating vale (HHV) to produce hydrogen for fuel-cells [1 - 28]. Thirdly, the distribution infrastructure already exists for ammonia to deliver in amounts larger than 100 million tons yearly or more [1 - 29]. However, using the combustion of NH_3 as car fuel can cause another problem, as the production, NOx can be produced. The term NOx describes a mixture of nitric oxide (NO)

and nitrogen dioxide (NO_2), which can cause damage to the human respiratory tract pollution problems, decreasing growth or reducing crop yields [1 - 30]. On the other hand, considering the toxicity of ammonia gas at very low concentrations can cause harm to humans. As a result, it is an important research field for forwarding to a carbon-neutral society regarding correctly, reasonably, safely, and effectively using NH_3.

1.3 Hydrogen-assisted degradation of fracture toughness

Fracture toughness tests measure the resistance ability of a material to further crack growth and propagation to failure. The construction of aircraft, buildings, and bridges are usually suffering from both high and low cycle fatigue, which can cause the initiation of fatigue cracking, crack is everywhere in our daily life. Engineers use fracture toughness tests to determine the load capacity of structural components. This allows the establishment of component lifespans, along with inspection and maintenance criteria. The well-known technical term "hydrogen embrittlement" (HE) expresses the effects due to hydrogen on metallic material strength properties such as ductility loss, decreased fracture toughness, and degradation of fatigue properties [1 - 31, 1 - 32]. Therefore, the fracture toughness test was conducted in this study. In this thesis, the effects of ammonia in the presence of hydrogen and the absence of hydrogen on fracture toughness were studied. Therefore, the state-of-arts on the hydrogen effect on fracture toughness is summarized in the following, which has many factors, for example, gas pressure, loading rate, material strength, and so on [1 - 33-1 - 43].

Firstly, fracture toughness can be reduced in hydrogen gas. The stress-intensity factor is used to represent the fracture toughness of most materials. The hydrogen effect is pronounced by an increase in hydrogen gas pressure [1 - 33-1 - 37]. Walliams and Nelson reported that the crack growth (ductile stable) rate increased with increased hydrogen gas pressures from 100 torr to 1000 torr [1 - 33]. Birenis et al. reported that gaseous hydrogen-induced embrittlement in the pure iron at room temperature during elastic-plastic fracture toughness tests [1 - 34]. As shown in Fig. 1.3, the crack-growth resistance curves in air occupied a higher position than that in hydrogen gas, which represents the degradation of crack growth resistance in the hydrogen gas environment. They also reported that with increasing the gas pressure from 0.7 MPa to 90 MPa, the resistance of the material further decreased. In other words, an increase in gas pressure enhances HE. Loginow and Phelps reported that the stress intensity factor (K_{IH}) decreased as hydrogen gas pressure decreased [1 - 35]. The gas pressure dependence has been considered by Sievert's law [1 - 36], which

expresses the thermodynamic equilibrium between hydrogen gas and dissolved atomic hydrogen. The equation is as below:

$$C = S\sqrt{f},$$

Where C is the concentration of dissolved H atom, f is the fugacity, and S is the solubility. Thus, as the pressure increased, the fugacity increased resulting in an increase in the quantity of H atom dissolved in material [1 - 37].

Secondary, Matsumoto et al reported that the hydrogen affects carbon steel (SM490B) had a loading rate dependence under 0.7 MPa gas pressure. The results showed that the fracture toughness of the material decreased with a decrease in the loading rate from 2.0×10^{-3} mm/s to 2.0×10^{-5} mm/s [1 - 38]. The same tendency is also reported by Komoda et al. The fracture toughness of the ASTM A333 grade 6 pipelines in 0.6 MPa hydrogen gas was significantly reduced when the loading rate was decreased from 2.0×10^{-3} mm/s to 2.0×10^{-5} mm/s because of sufficient time for hydrogen entering material [1 - 39].

Thirdly, HE by fracture toughness degradation is more pronounced with the increased yield strength of the material. Sandoz reported that the threshold (crack initiation) stress intensity factors of martensitic AISI 4340 steel decreased with an increased yield strength of the material in hydrogen gas [1 - 40]. Nibur found the same tendency and reported that the threshold stress intensity factors of HY-130, Ni-Cr-Mo steels, and Cr-Mo steel in 103 MPa hydrogen gas decreased with an increased yield strength of the material [1 - 41].

There are a lot of researchers who reported that the fracture surface was changed in hydrogen gas. S. Matsuoka et al. reported that the fracture toughness of austenitic stainless steels (Types 304, 316) was decreased in hydrogen gas as shown in Fig. 1.4. The fracture surface during the J_{IC} test in the air at room temperature was covered with dimples (D). In contrast, the fracture surface in hydrogen gas was covered with quasi-cleavages (QC) [1 - 42]. G. Alvarez et al. have investigated the effect of the displacement rate on the fracture surface of two different structural steels (S355 steel and H8 steel). They reported that

decreased displacement rate reduced the fracture toughness of the material and enhanced hydrogen embrittlement as shown in Fig. 1.5. The decreased displacement rate gives rise to a modification of the fracture micromechanics from ductile micromechanics (microvoid coalescence) in the absence of hydrogen to brittle micromechanics (cleavage or plasticity related hydrogen induced cracking) due to hydrogen induced decohesion of interphases when a certain hydrogen concentration is achieved. The fracture surface was changed as shown in Fig. 1.6. [1 - 43].

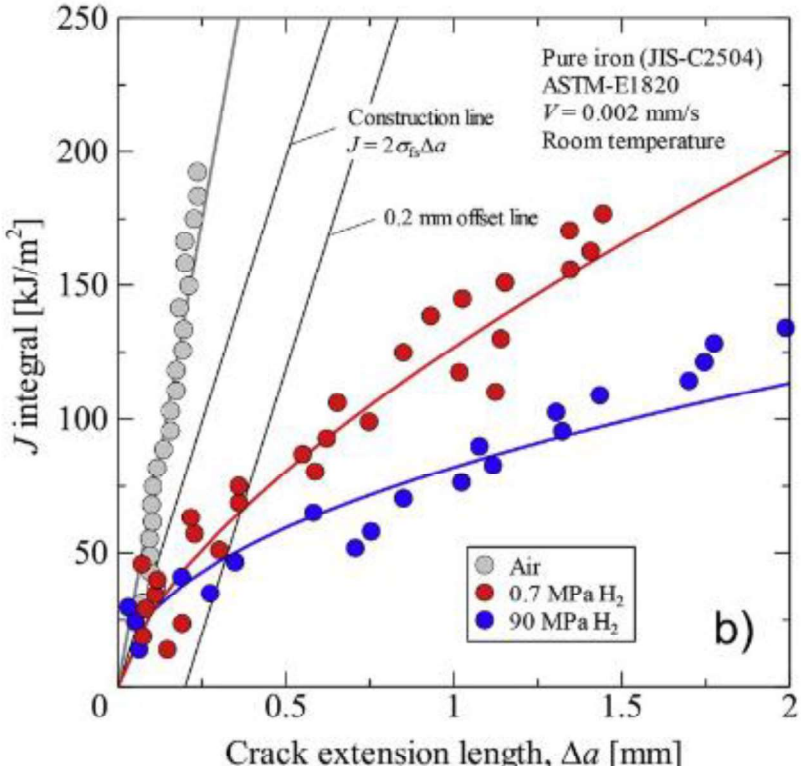

Fig. 1.3 The corresponding crack-growth resistance curve for specimens tested in air and in 0.7 MPa and 90 MPa hydrogen gas at room temperature by D. Birenis et al. [1 - 34]

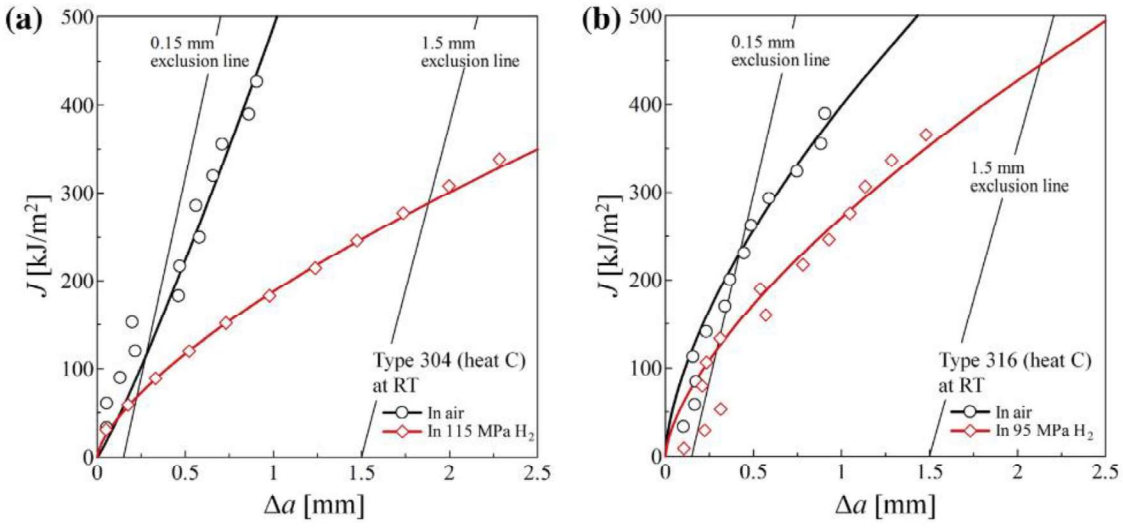

Fig. 1.4 *J*-Δ*a* curves in air and in hydrogen gas at room temperature by S. Matsuoka et al. [1 - 42]

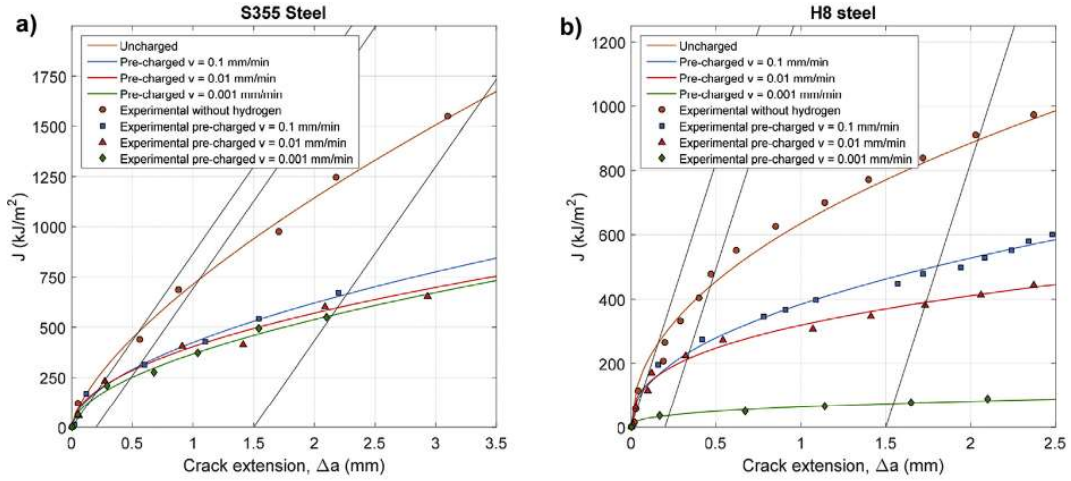

Fig. 1.5 Fracture toughness versus crack growth *J*-Δ*a* curves by G. Alvarez et al. [1 - 43]

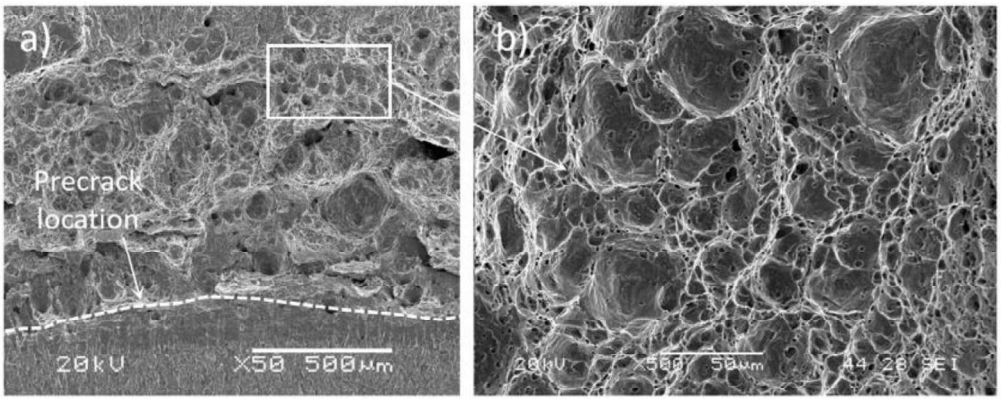

(a)

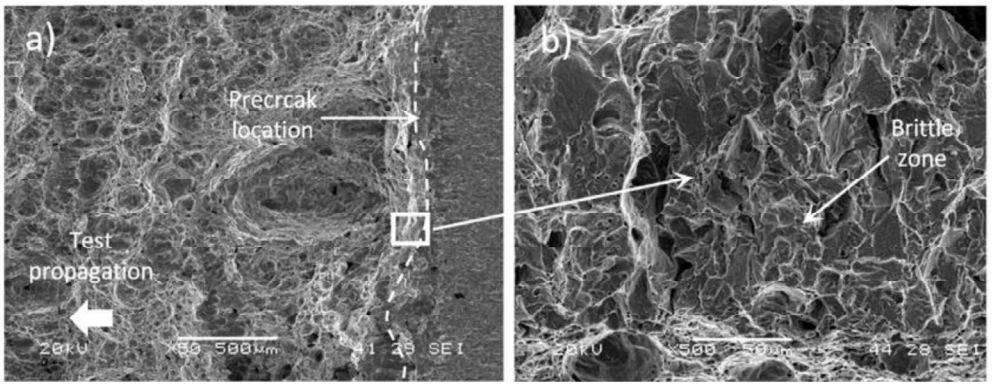

(b)

Fig. 1.6 Fracture surface (a) S355 fracture surface of uncharged specimens
(b) S355 fracture surface of hydrogen pre-charged specimens by G. Alvarez et al. [1 - 43]

1.4 Past study on impurities contained in hydrogen gas and their mitigation effect on hydrogen embrittlement in H_2 gas

Hydrogen embrittlement (HE) firstly requires hydrogen uptake from the environment into the material. As Nagao et al. experimentally demonstrated that exposure of the SCM435 low-alloy steel, whose surface is covered by a natural oxide layer, to 120 MPa H_2 gas at room temperature caused no increase in the hydrogen concentration in the material [1 - 44]. It implies that hydrogen uptake from H_2 gas into steel at room temperature requires a fresh iron (Fe) surface, which can act as a catalytic site for the dissociation of molecular hydrogen into atomic hydrogen, which is created by crack propagation [1 - 45]. Staykov et al. explained the role of the Fe surface as a catalyst for the dissociation of H_2 molecules by density functional theory (DFT) simulations [1 - 46]. The Fe surface should be clean in order to act as a catalyst for the H_2 dissociation. In other words, preadsorbed oxygen (O_2) on the Fe surface hinders the catalytic action. Somerday et al. considered that the hydrogen uptake from hydrogen gas occurs at the newly created surfaces during crack propagation. They experimentally confirmed both the hydrogen uptake through the surfaces created during crack propagation and the blocking of hydrogen uptake by preadsorbed O_2 based on their crack propagation tests of X52 steel as shown in Fig. 1.7 [1 - 47].

Gas impurities contained in H_2 gas can work as a poison for the catalytic action of Fe surfaces when the impurity gases have a higher affinity with the Fe surface than the H_2 molecule. Carbon monoxide (CO) is one of the gas species that can act as a mitigator of the HE [1 - 48, 1 - 49]. Komoda et al. clarified the mitigation effects of CO and O_2 on the HE focusing on their reaction rates with the Fe surface. Staykov et al. theoretically calculated the ratio of the impurity-occupied site and impurity-free site on the Fe surface in order to interpret the result of the fracture toughness tests were conducted as shown in Fig. 1.8 [1 - 48]. They showed that O_2 coverage is 100% and the CO one is at most 75% [1 - 48, 1 - 49]. These results are useful to understand the different HE mitigation properties between the O_2 and CO impurities.

Regarding the effect of NH_3, NH_3 induces stress corrosion cracking, which is one of the forms of hydrogen embrittlement [1 - 50]. Also, degradation of the tensile strength properties is induced in the NH_3 environment [1 - 51]. On the other hand, NH_3 added to H_2 gas significantly mitigated the hydrogen-assisted crack growth of 4340 steel as shown in Fig. 1.9 [1 - 52].

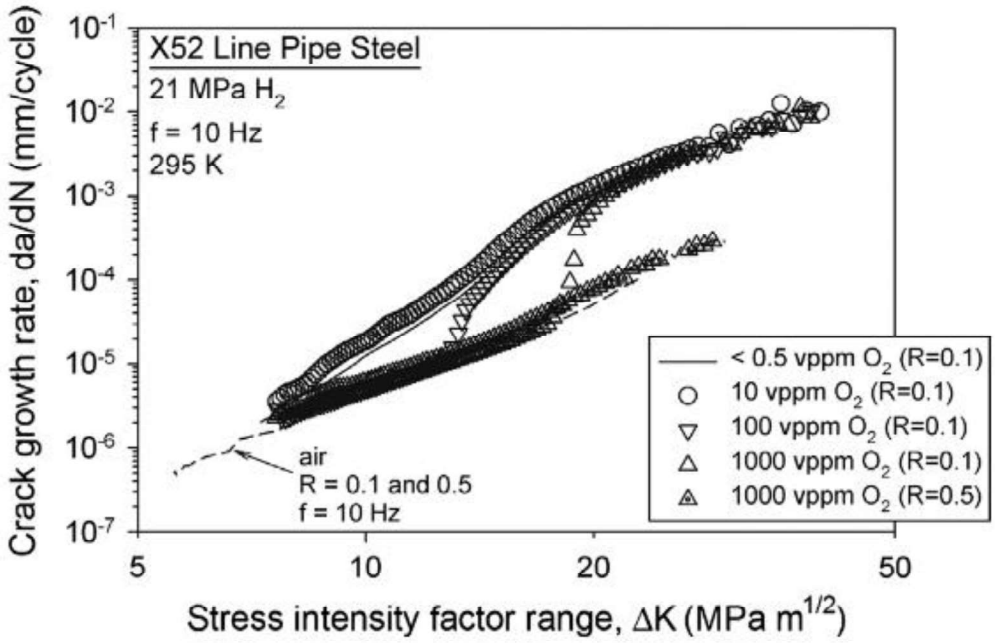

Fig. 1.7 Fatigue crack growth rate (da/dN) vs. stress intensity factor range (ΔK) relationships for X52 line pipe steel in mixed H_2 and O_2 by BP Somerday et al. [1 - 47]

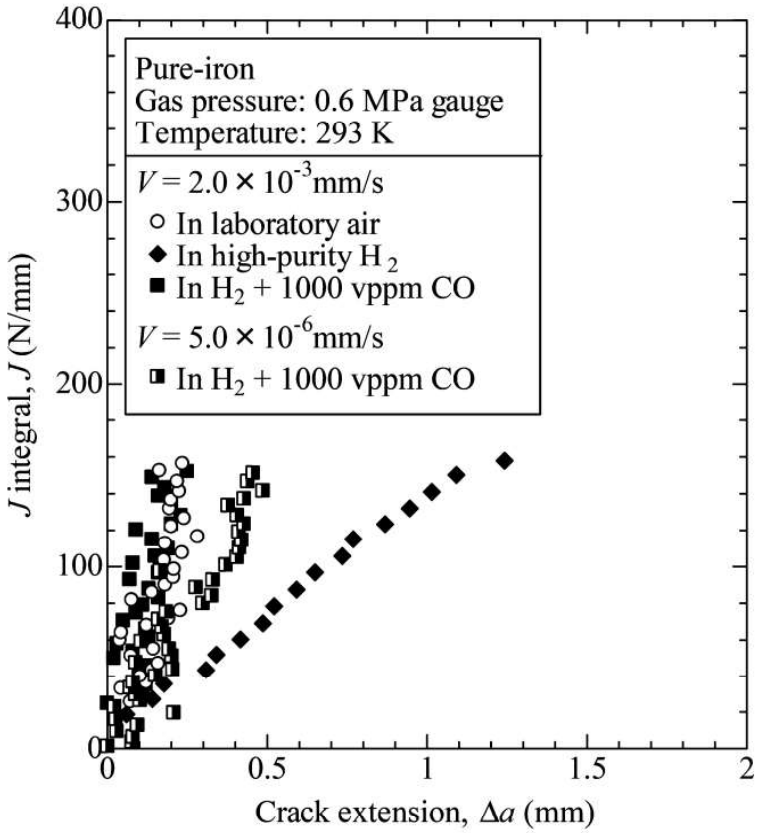

Fig. 1.8 Inhibitory effect of CO on hydrogen embrittlement and its loading rate dependency by R. Komoda et al. [1 - 48]

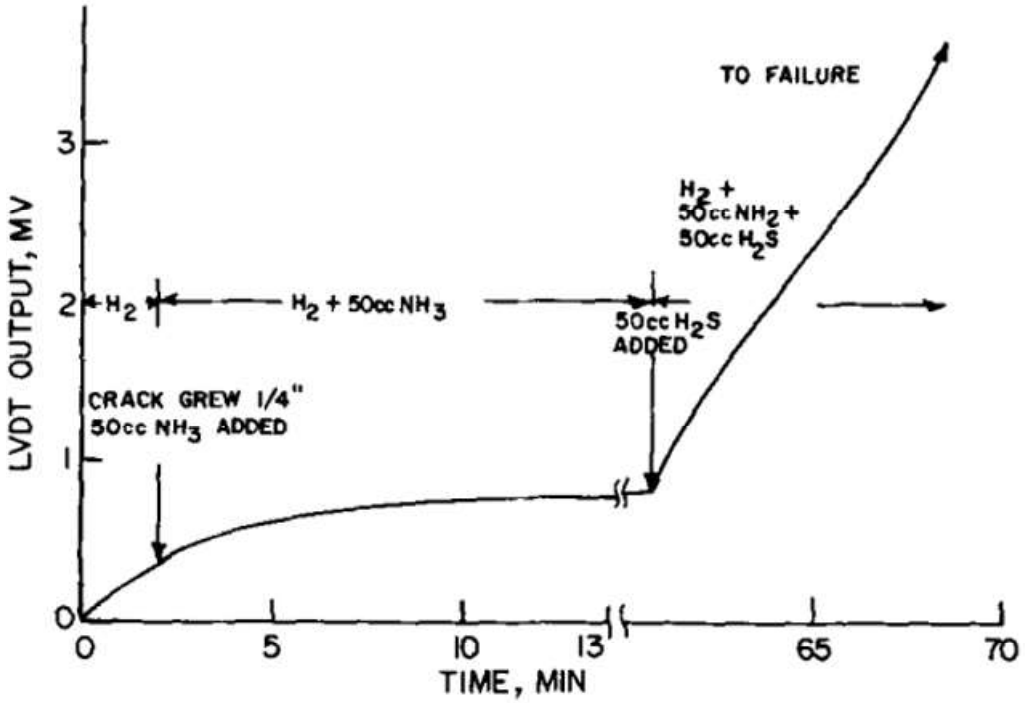

Fig. 1.9 Crack extension vs. time for hydrogen-oxygen mixture by Srikrishnan, V. et al. [1 - 52]

1.5 Density functional theory calculation and theoretical understanding

1.5.1 Density functional theory history and applications

Modern computational modeling of materials from first principles relies on a variety of theoretical and computational techniques, which is called density functional theory (DFT) [1 - 53]. The first principle DFT is the main tool for modern materials simulations and it is a very effective method for studying molecules, nanostructure, solids, surfaces, and interfaces by directly solving approximate versions of the Schrodinger equation. The essence of the DFT method is to take the electron density as the carrier of all the information in the ground state of the molecule (atom), rather than the wave function of a single electron so that the multi-electron system can be transformed into a single-electron problem for solving. Assuming that the number of electrons is *N*, the number of variables in the wave function is 3*N*, and the density functional theory reduces the number of variables to three spatial variables, which not only simplifies the calculation process but also ensures the calculation accuracy.

The development of density functional theory can be divided into three stages. The first stage was in 1927. Thomas and Fermi proposed the Thomas-Fermi model based on the assumption of the uniform electron gas in an ideal state [1 - 55]. The concept of density functional was introduced for the first time, which became the prototype of the later DFT method. The starting point of the Thomas-Fermi model is to assume that there is no interaction between electrons and no external force interference, then the Schrödinger equation of electron motion can be expressed as:

$$-\frac{h}{2m}\nabla^2\varphi(r) = E\varphi(r)$$

Solved as:

$$\varphi_k(r) = \frac{1}{\sqrt{V}}\exp(ik \cdot r)$$

Considering the electron arrangement law at 0 K, the electron density, the total energy of a single electron and the kinetic energy density of the system are respectively:

$$\rho = \frac{1}{3\pi^2}(\frac{2m}{h^2})^{\frac{3}{2}}E_F^{\frac{3}{2}}$$

$$T_e = \frac{3E_F}{5}$$

$$t[\rho] = \rho T_e = \frac{3}{5}\frac{h^2}{2m}(3\pi^2)^{\frac{2}{3}}\rho^{\frac{5}{3}} = C_k\rho^{\frac{5}{3}}$$

Considering the description of the Coulomb potential between electrons and the external field, the total energy expression of the electron system can be deduced only by the electron density function. Although this model simplifies the calculation form and process, it does not consider the interaction between electrons and does not accurately describe the kinetic energy term, so it is not applicable in many systems. However, inspired by this novel research idea, related scholars basically perfected the content of density functional theory in the 1960s after years of hard work, and finally established a strict density functional calculation theory.

Hohenberg-Kohn Theorem and Kohn-Sham equation play a key role in the formation and improvement of DFT method, and are known as the two cornerstones of DFT [1 - 56].

(1) Hohenberg-Kohn Theorem

The main concept of Hohenberg-Kohn theorem is that all physical quantities in the system can be uniquely determined by the variable containing only the electron density, and the realization method is to obtain the ground state of the system through the variational principle. The theory is mainly aimed at the non-uniform electron gas model and consists of two sliver theorems. i) a spin - ignoring electron system in an external potential (except for

the potential of electron interaction) whose external potential can be uniquely determined by electron density; ii) For a given external potential, the ground state energy of the system is the minimum value of the energy functional. Thus, the energy functional of the system can be described as:

$$\mathrm{E}(\rho,\mathrm{V}) = \int V(r)\rho(r)dr + T[p(r)] + \frac{e^2}{2}\int \frac{\rho(r)\rho(r')}{|r-r'|}drdr'$$

Where the right side of the equation are electron potential energy, kinetic energy term, coulomb interaction between electrons and exchange associated potential energy in the outer field respectively. However, this theorem does not give the specific expression of electron density function, kinetic energy function and exchange correlation function, so the specific solution cannot be carried out.

(2) Kohn-Sham equation

Until 1965, the Kohn-Sham equation was established and gave the specific description of each term, which made the density functional theory enter the stage of practical application. For the kinetic energy functional, they propose to use the particle kinetic energy functional without mutual influence to approximate the replacement, and the difference between the two is included in the unknown term of the exchange correlation functional. The density function is defined as: $\rho(\mathrm{r}) = \sum_i^n |\emptyset_i(r)|^2$, the variation of ρ is replaced by the variation of $\emptyset_i(r)$, and the Lagrange multiplier is replaced by E_i. Thus, the single-electron equation is:

$$\{-\nabla^2 + V_{KS}[\rho(r)]\}\emptyset_i(r) = E_i\emptyset_i(r)$$

Where,

$$V_{KS}[\rho(r)] = v(\mathrm{r}) + V_{coul}[\rho(r)] + V_{xc}[\rho(r)]$$

$$= v(\mathrm{r}) + \int dr' \frac{\rho(r')}{|r-r'|} + \frac{\delta E_{xc}[\rho(r)]}{\delta\rho(r)}$$

This is the Kohn-Sham equation.

Kohn-sham equation gives explicit expression to all the items (independent particle model, Hartree potential and exchange correlation) except exchange correlation functional, and also merges the complex items in this item. At this point, the difficulty of calculation has been greatly simplified, and all the work began to focus on how to describe the exchange correlation functional. At the same time, the approximate form of exchange correlation potential also directly determines the precision of density functional theory.

The Local Density Approximation (LDA) method was also proposed by Kohn et al in 1965. The purpose of LDA is to approximate the unknown exchange correlation item so that DFT method can be used in practical calculation. LDA uses the density function of uniform electron gas to calculate the exchange correlation item of non-uniform electron gas. Assuming that the electron density in the system changes very little with space, the exchange correlation item of non-uniform electron gas can be expressed as:

$$E_{xc}^{LDA}[\rho(R)] = \int \rho(r)\varepsilon_{xc}[\rho(r)]dr$$

The corresponding exchange correlation potential can be expressed as:

$$V_{xc}^{LDA}(r) = \frac{\delta E_{xc}^{LDA}}{\delta\rho(r)} = \varepsilon[\rho(r)] + \frac{\delta\varepsilon_{xc}(\rho)}{\delta\rho}\rho(\mathrm{r})$$

In order to calculate the actual material system more accurately, Becke, Perdew and Wang et al. proposed the Generalized Gradient Approximation (GGA) in 1986, which is also the most widely used method in density functional calculation and performed in this study.

GGA is to rewrite the original representation term into a functional form containing electron density and gradient function, plus the description of spin, and the obtained exchange correlation functional is as follows:

$$E_{xc}^{GGA}[\rho] = \int f_{xc}(\rho_\alpha(r), \rho_\beta(r), \nabla\rho_\alpha(r), \nabla\rho_\beta(r))dr$$

In GGA, exchange correlation potential can also be disassembled into exchange energy and correlation energy. Beckc et al. argued that the concrete functional form could be constructed arbitrarily in principle without considering the actual physical meaning, such as GGA-PW91; However, Perdew et al. advocated to return to pure quantum mechanical calculation theory as far as possible, and all physical quantity calculation should only start from basic constants such as electronic static mass, Planck constant and speed of light, and functional expressions should not contain too many empirical parameters. For example, GGA-PBE (Perdew-Burke-Enzerhoff) is commonly used in condensed matter physics and other fields. Past studies by GGA-PBE have shown well agreement with experiments [1 - 57-1 - 59] and the block diagram of DFT program as shown in Fig. 1.10.

The popularity of density functional theory has significantly increased in the recent 20 years as shown in Fig. 1.11 [1 - 55]. The density functional theory is an incredible success story. The application of DFT calculation is rapidly becoming a great tool to investigate the mechanism and reveal the property of the material. Plenty of researchers study the surface reaction between gaseous species and the solid surface by DFT [1 - 45, 1 - 47, 1 – 56 - 1 - 59].

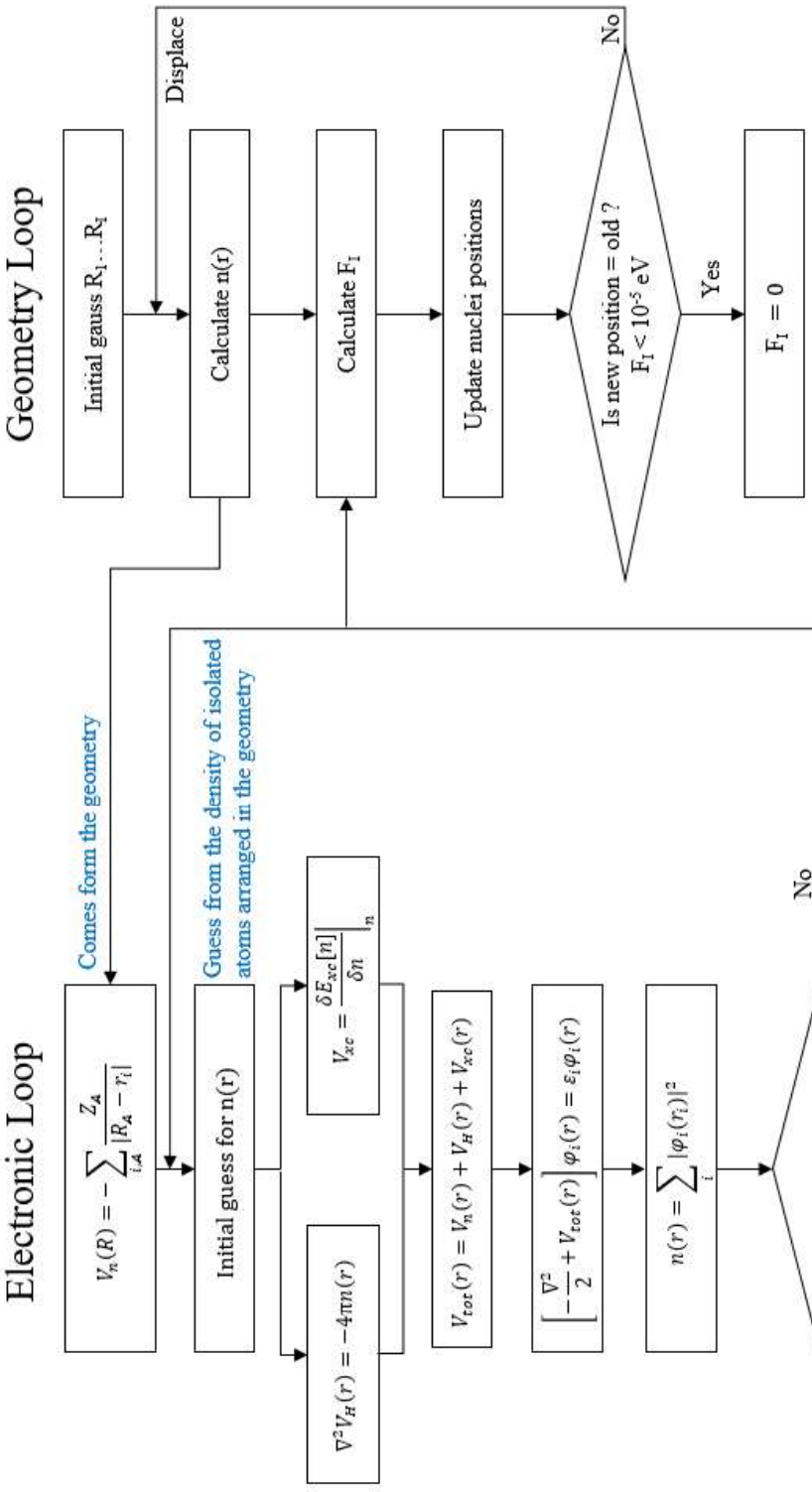

Fig. 1.10 Block diagram of DFT program.

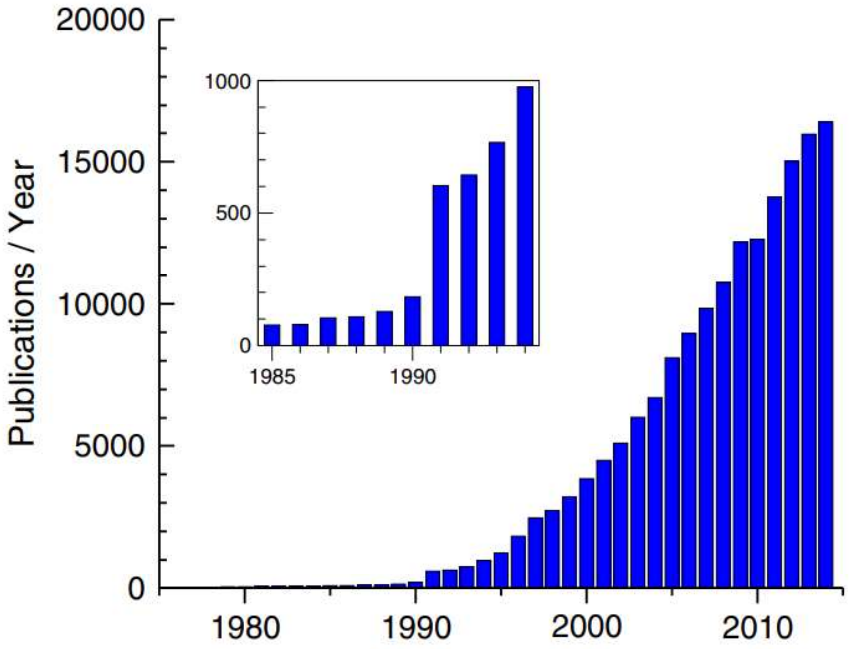

Fig. 1.11 Number of publications per year on topics of DFT according to the Web of Science Core Collection [1 - 55]

1.5.2 Methods of investigation: Basic setting

Periodic, DFT was performed with the Linear Combination of Atomic Orbitals (LCAO), which is built from quantum mechanics principles and can be used to investigate the structural and electronic properties of materials [1 - 65]. The GGA Perdew-Burke-Ernzerhof (PBE) exchange-correlation functional was applied using Fritz-Haber-Institute (FHI) pseudopotentials. Electron energies were converged to 10^{-6} eV and using Fermi smearing with sigma = 0.1 eV, which is suitable accuracy for geometry optimization. The calculations were performed with a 400eV cutoff energy (largest amount of energy, necessary to describe orbitals) and Monkhorst-Pack k-point mesh of 8×8×8 (properly describe properties of one unit cell for the BCC bulk iron lattice and 4×4×1 for the (110) terminated iron slab. The relaxation was performed until the forces converged to values below 0.05 eV/A, which is suitable accuracy for geometry optimization. For bulk systems, relaxation was performed for the cell volume, cell shape, and atomic positions. For slab models, relaxation was performed for the atomic positions only. Slabs were constructed using 6 alternating iron layers. The coordinates of the atoms in the middle two layers were fixed, while the coordinates of the top two and bottom two were fully relaxed. Activation barriers for various reaction mechanisms were obtained using the climbing image-nudged elastic band method (CI-NEB). In the process of NEB calculations, eight to ten images were used between the starting and the ending geometries of reactions. Throughout this study, we used the graphical visualization Quantum ATK [1 - 66].

1.5.3 Kinetic derivation of the Langmuir Theory

A finish of a chemical reaction does not mean there are no reactants left, the reaction might just achieve equilibrium and there are some remaining reactants: the reaction is said to have reached equilibrium. The concept of chemical equilibrium was developed in 1803 [1 - 67]. For any reaction mixture to exist at equilibrium, the rates of the forward and backward (reverse) reactions must be equal. In the following chemical equation, arrows point both ways to indicate equilibrium.

For molecules in contact with a solid surface at a fixed temperature, the Langmuir Isotherm, developed by Irving Langmuir in 1916 [1 - 68], describes the partitioning between the gas phase and adsorbed species as a function of applied pressure. Langmuir was awarded the Nobel Prize in 1932 for his work concerning surface chemistry. The basic assumption of this theory is: 1) assume the surface is homogeneous (no corrugations); 2) All sites are energetically equivalent and the energy of adsorption is equal for all sites; 3) The adsorbing gas adsorbs into an immobile state; 4) mono-layer coverage only; 5) No interactions between adsorbate molecules on adjacent sites. He published two papers to confirm that the adsorbed films do not exceed one molecule in thickness [1 - 69, 1 - 70].

The Langmuir theory consisted of different adsorption models, in which basic model with only one adsorbed species, the competitive model, the dissociative model, and the most complicated one competitive and dissociative model. In this study, the competitive and dissociative model was studied for investigating the NH_3 competitive with H_2 on the Fe (110) surface.

For the single adsorbate case, the model assumes adsorption and desorption as being elementary processes, where the rate of adsorption r_{ad} and the rate of desorption r_d are given by

$$r_{ad} = k_{ad} p_A [S]$$

$$r_d = k_d[A_{ad}]$$

Where p_A is the partial pressure of A over the surface, $[S]$ is the surface concentration of the free site, $[A_{ad}]$ is the surface concentration of adsorbed specie A, and the k_{ad} and k_d are the constants of forward adsorption reaction and backward desorption reaction in the above reaction.

At equilibrium, the rate of the adsorption equal to the rate of desorption. Setting $r_{ad} = r_d$, thus, the equilibrium constant

$$K_{eq}^{A} = \frac{[A_{ad}]}{p_A[s]} = \frac{k_{ad}}{k_d} \tag{1.1}$$

In eqs 1.1, the rate is given by the Arrhenius equation. The equilibrium constant is the independence of the pressure of the system, or of the concentration of the reacting substance. Adding a catalyst will affect both the forward reaction and the backward reaction in the same way and will not have an effect on the equilibrium constant. The catalyst will speed up both reactions thereby increasing the speed at which equilibrium is reached.

Considering the entire surface is covered by adsorbed specie A and free site, applied to the previous equation that combined site balance and equilibrium, yields the Langmuir adsorption isotherm,

$$\theta_A = \frac{P_A K_A}{1 + P_A K_A}$$

For the competitive adsorption, there are two distinct adsorbates present in the system (species A and B) that compete for the same adsorption sites. The assumption of this model is: all sites on the surface are equivalent; each site can hold one molecule A or B, however it not both simultaneously; there are no interactions between adsorbate molecules on adjacent sites. Based on kinetic consideration, the equilibrium constant for A and B are given by equations as below:

$$K_{eq}^{A} = \frac{[A_{ad}]}{p_A[s]}$$

And

$$K_{eq}^{B} = \frac{[B_{ad}]}{p_B[s]}$$

The surface is covered by *A*, *B*, and free sites, therefore, the expressions for θ_{A} and θ_{B} are as below:

$$\theta_{\mathrm{A}} = \frac{P_A K_A}{1+P_A K_A+P_B K_B} \tag{1.2}$$

$$\theta_{\mathrm{B}} = \frac{P_B K_B}{1+P_A K_A+P_B K_B} \tag{1.3}$$

However, in the case of dissociation adsorption, the molecule D_2 will dissociate into two adsorbed atoms. The 1/2 exponent on p_{D_2} arises because one gas phase molecule produces two adsorbed species.

In this study, we have performed surface coverage estimation based on the Langmuir theory. The H_2 molecule dissociates into two H atoms can be solved by the 1/2 exponent on p_{H_2}. The full NH_3 decomposition on the Fe surface is into a N atom and three H atoms, the processing on the surface is way more complicated than in H_2. The Kinetic derivation of NH_3 decomposition on the Fe surface, and NH_3 decomposition competitive with H_2 dissociation on the Fe surface are studied in chapters 3 and 4, respectively.

1.5.4 Arrhenius equation and Transition-state theory

In this study, we analyzed the reaction rate using the Arrhenius equation [1 - 71]. In the Arrhenius equation, k is the reaction rate constant, A is the pre-exponential factor which represents the frequency that atoms and molecules collide in a way that leads to a reaction, E_a is the activation energy barrier for the reaction, R is the universal gas constant, and T is the absolute temperature. The equation is commonly given as in equation 1.4,

$$k = Ae^{-\frac{E_a}{RT}} \tag{1.4}$$

The equation is named after the Swedish chemist Svante Arrhenius. His research shows that the relationship is applicable to almost all kinds of reactions. He also provided a theoretical basis for the equation by an analogy with the expression for the thermodynamic equilibrium constant. The collision and transition state theories of chemical reactions showed numerical constants A and E_a to represent quantities indicating the fundamental process of chemical reactions.

Collision theory is used to predict the rate of chemical reactions, especially of gases. Collision theory assumes that a reaction occurs when the reacting substances (atoms or molecules) come together or collide with each other. But not all collisions bring about chemical changes. Collisions can effectively produce chemical changes only if the specie has a certain minimum internal energy equal to the activation energy of the reaction. Furthermore, the colliding species must be oriented in a way that favors the necessary rearrangement of atoms and electrons. Therefore, according to collision theory, the rate at which chemical reactions proceed is equal to the frequency of effective collisions.

Transition-state theory also known as activated-complex theory or absolute reaction rate theory, deals with chemical reactions and other processes as occurring through continuous changes in the relative positions and potential energies of constituent atoms and molecules. In the reaction path between the initial and final arrangement of an atom or

molecule, there exists an intermediate configuration that has the maximum value of potential energy, which is referred to as the transition state. The difference in energy between the transition state and the initial state is closely related to the experimental activation energy of the reaction. It represents the minimum energy that must be obtained for a reaction system or flow system to occur. Transition-state theory can also be formulated in thermodynamic terms. The transition state can be calculated by CI-NEB. Transition-state theory is directed to the calculation of the one-way rate constant at equilibrium.

1.5.5 Pre-exponential factor

In chemical kinetics, the pre-exponential factor or *A* factor is the pre-exponential constant in the Arrhenius equation, an empirical relationship between temperature and rate coefficient. According to transition state theory, *A* is the entropy of activation of the reaction.

In this study, the vibrational frequencies of normal modes of the decomposition reaction of NH_3 and dissociation reaction of H_2 were calculated by combining dynamical matrix and vibrational mode calculation of Quantum ATK. Initial and transition geometry were converged to 10^{-8} eV to ensure that the vibrational frequency calculation yield proper results because vibrational frequency calculation require well converged electron density. Each ion in the cell is then displaced by ±0.01 Å in all directions of the cartesian vector, then a Hessian matrix was constructed from the force which shows how atoms react to displacement. Force derivative tolerance is set to 10^{-3} eV/Å. Once the normal mode vibrational frequencies of the system were obtained, I multiplied all data (excluding the imaginary one) and divide the data from initial to transition frequency to get the attempt frequency.

$$A = \frac{\prod_{i=1}^{3N} v_i^O}{\prod_{i=1}^{3N} v_i^S} \tag{1.5}$$

Where $\prod_{i=1}^{3N} v_i^O$ is multiplying all vibrational frequencies at initial configuration, $\prod_{i=1}^{3N} v_i^S$ is multiplying all vibrational frequencies at transition state configuration (has one more imaginary frequency). Vibrational frequency from finite difference. And the vibrational frequency is calculated by constructing a matrix from the force exerted by a very small displacement of atoms going back to equilibrium.

1.6 Objective of this study

As described in the previous subsections, NH_3 can lead to the degradation of the mechanical properties of materials, and HE is one of the great obstacles to our transition to a carbon-neutral society. Meanwhile, it is significant to point out that NH_3 is considered a hydrogen carrier due to its higher hydrogen density than liquid hydrogen. Therefore, characterization and elucidation of the effect of NH_3 on HE plays a vital role to forward to a carbon-neutral society. It is critically important to note that in the past studies the mechanism of NH_3 mitigation and induction effect on HE is still unclear up to now. However, considering the practical application of NH_3 soon, such kind of research is indispensable.

Based on those reasons, the objective of this study is to characterize the effect of NH_3 added to H_2 gas as an impurity on the HE of the SCM440 low-alloy steel during a fracture toughness test and elucidate the mechanism by density functional theory. Particularly, this study elucidated the mechanism of the coadsorption of NH_3 and H_2 on an iron surface, NH_3 itself on an iron surface, and both their implication on the HE and the effect of loading rate and NH_3 concentration on it.

The material used in this study was JIS SCM440 Cr-Mo low-alloy steel. SCM440 is similar to the material used for the hydrogen cylinder at the hydrogen station (for example, SCM435), and also SCM440 is a kind of low-alloy steel that is also used for high-strength pipeline steel. Considering the impurity mitigation strategy on HE, the most economic benefit is it allows us to use the current equipment as hydrogen equipment, and the wide application area of SCM440 similar material, SCM440 was investigated in this study.

1.7 References

1. Glen R. R., Teresa G., Marcel M., et al, The nitrification process for nitrogen removal in biofloc system aquaculture, *Reviews in Aquaculture*, Vol. 12, **2020**, pp. 2228-2249.
2. Michael F. D., Key roles of microsymbiont amino acid metabolism in rhizobia-legume interactions, *Critical Reviews in Microbiology*, Vol. 41, **2015**, pp. 411-451.
3. Neville R. G., Steps leading to the discovery of oxygen 1774 - A bicentennial tribute to Joseph Priestley, *Journal of Chemical Education*, Vol. 51, **1974**, pp. 428-431.
4. Sutton M. A., Erisman J. W., Dentener F., Möller D., Ammonia in the environment: From ancient times to the present, *Environmental Pollution*, Vol 156, **2008**, pp. 583-604.
5. Erisman J., Sutton M., Galloway J., et al, How a century of ammonia synthesis changed the world. *Nature Geoscience*, Vol. 1, **2008**, pp. 636-639.
6. Farea M. A., Mohammed H. Y., Shirsat S. M., et al, Hazardous gases sensors based on conducting polymer composites: Review, *Chemical Physics Letters*, Vol. 776, **2021**, pp. 138703.
7. Toxic FAQ sheet for ammonia published by the Agency for Toxic Substances and Disease Registry (ATSDR), September **2004**.
8. Shirley N., Kathleen P., Rose M. T., et al, EC88-422 household cleaning and laundry products: which one for the job, *University of Nebraska-Lincoln*, **1988**, pp. 3-11.
9. William L. B., Howard W. H., Combustion properties of ammonia, *Chemical engineering progress*, Vol. 58, **1962**, pp. 81-84.
10. Overstreet R., Giauque W. F., Ammonia. The Heat Capacity and Vapor Pressure of Solid and Liquid. Heat of Vaporization. The Entropy Values from Thermal and

Spectroscopic Data, *Journal of the American Chemical Society*, Vol. 59, **1937**, pp. 254-259.

11. Fasihi M., Weiss R., Savolainen J., Breyer C., Global potential of green ammonia based on hybrid PV-wind power plants, *Applied Energy*, Vol. 294, **2021**, pp. 116-170.
12. Peter H. P., Towards sustainable agriculture: fossil-free ammonia, *Journal of Renewable and Sustainable Energy*, Vol. 9, **2017**.
13. Griffin P. W., Hammond G. P., Norman J. B., Industrial energy use and carbon emissions reduction in the chemicals sector: A UK perspective, *Applied Energy*, Vol. 227, **2018**, pp. 587-602.
14. World Energy Council, World Energy Scenarios 2019 – Exploring Innovation Pathways to 2040, in Collaboration with Accenture Strategy and, Paul Scherrer Institute, London, September **2019**.
15. World Energy Council, Global Energy Comparison Review, World Energy Insights Brief 2019, London, April **2019**.
16. Kober T., Schiffer H. W., Densing M., Panos E., Global energy perspectives to 2060 WEC's World Energy Scenarios 2019, *Energy Strategy Reviews*, Vol. 31, **2020**, pp. 1-19.
17. BP, BP Statistical Review of World Energy June 2019, London, **2019**.
18. BP, BP Energy Outlook – 2019 Edition, London, **2019**.
19. Nick W., et al. Health and climate change: policy responses to protect publish health, *The lancet commissions*, Vol. 386, **2015**, pp. 1861-1914.
20. Jonathan A. P., Diarmid C., et al, Impact of regional climate change on human health, *Nature*, Vol. 438, **2005**, pp. 310-317.
21. World Health Organization, A vision for primary health care in the 21st century: towards universal health coverage and the sustainable development goals, **2018**.
22. Hoegh G. O., Mumby P. J., Hooten A.J., et al, Coral reefs under rapid climate change and ocean acidification, *Science*, Vol. 318, **2007**, pp. 1737-1742.

23. Rogelj J., Elzen D. M., Höhne N., et al. Paris Agreement climate proposals need a boost to keep warming well below 2 °C, *Nature*, Vol. 534, **2016**, pp. 631–639.
24. International Energy Agency (IEA), Global energy review: CO_2 emissions in 2021-analysis, **2021**.
25. Neena R., Sonakya V., Vanita A., Kalia V. C., Waste Management and Production of Future Fuels, *Journal of Science and Industrial Research*, Vol. 61, **2002**, pp. 184-207.
26. Zamfirescu C., Dincer I., Ammonia as a green fuel and hydrogen source for vehicular applications, *Fuel Processing Technology*, Vol. 90, **2009**, pp. 729-737.
27. Feibelman P.J., Stumpf R., Comments on "Potential roles of ammonia in a hydrogen economy", **2008**.
28. Jensen J.O., Vestbø A.P., Li Q., Bjerrum N.J., The energy efficiency of onboard hydrogen storage, *Journal of Alloys and Compounds*, Vol. 446–447, **2007**, pp. 723-728.
29. Blarigan P.V., Advanced internal combustion engine research. Proceedings of the DOE Hydrogen Program Review, NREL/CP-570-28890.
30. Boningari T., Smirniotis P. G., Impact of nitrogen oxides on the environment and human health: Mn-based materials for the NOx abatement, *Current Opinion in Chemical Engineering*, Vol. 13, **2016**, pp. 133-141.
31. Johnson W. H. On some remarkable changes produced in iron and steel by the action of hydrogen and acids, *American Society for Metals*, Vol. 1, **1977**, pp. 168-179.
32. Beachem C. D., A new model for hydrogen-assisted cracking (hydrogen "embrittlement"), *Metallurgical and materials Transactions B*, Vol. 3, **1972**, pp. 441-455.
33. Williams D. P., Nelson H. G., Embrittlement of 4130 steel by low-pressure gaseous hydrogen. *Metallurgical and Materials Transactions B*, Vol. 1, **1970**, pp. 63–68.

34. Birenis D., Ogawa Y., Matsunaga H., Takakuwa O., et al, Hydrogen-assisted crack propagation in α-iron during elastic-plastic fracture toughness tests, *Materials Science and Engineering: A*, Vol. 756, **2019**, pp. 396-404.
35. Loginow A. W., Phelps E. H., Steels for Seamless Hydrogen Pressure Vessels, *Corrosion*, Vol. 31, **1975**, pp. 404-412.
36. Hirth J. P., Effects of Hydrogen on the Properties of Iron and Steel, *Metallurgical Transactions A*, Vol. 11, **1980**, pp. 861-890.
37. Somerday B. P., San M. C., Effects of hydrogen gas on steel, vessels and pipelines. Materials for the hydrogen economy, *CRC Press*, **2008**. pp. 157–179.
38. Matsumoto T., et al, Effect of Displacement Velocity on Elastic Plastic Fracture Toughness of SM490B Carbon Steel plate in 0.7 MPa hydrogen gas, *Nihon Kikai Gakkai Ronbunshu, A Hen/Transactions of the Japan Society of Mechanical Engineers, Part A*, Vol. 79, **2013**, pp. 1210-1225.
39. Komoda R., Kubota M., Staykov A., et al, Inhibitory effect of oxygen on hydrogen-induced fracture of A333 pipe steel, *Fatigue & Fracture of Engineering Materials & Structures*, Vol. 42, **2019**, pp. 1387-1401.
40. Sandoz G., A unified theory for some effects of hydrogen source, alloying elements, and potential on crack growth in martensitic AISI 4340 steel, *Metallurgical and Materials Transaction B*, Vol. 3, **1972**, pp. 1169-1176.
41. Nibur K. A., et al, Measurement and interpretation of threshold stress intensity factors for steels in high-pressure hydrogen gas, *Sandia National Laboratories (SNL)*, **2010**.
42. Matsuoka S., Yamabe J., Matsunaga H., Criteria for determining hydrogen compatibility and the mechanisms for hydrogen-assisted, surface crack growth in austenitic stainless steels, *Engineering Fracture Mechanics*, Vol. 153, **2016**, pp. 103-127.
43. Álvarez G., Peral L.B., Rodríguez C., T.E., et al, Hydrogen embrittlement of structural steels: Effect of the displacement rate on the fracture toughness of high-

pressure hydrogen pre-charged samples, *International Journal of Hydrogen Energy*, Vol. 44, **2019**, pp. 15634-15643.

44. Nagao A., Koga J., Takagi S., Ono H., Ishikawa N., Experimental and computational studies on hydrogen entry into steel exposed to high-pressure hydrogen gas. ISIJ conference, Tokyo, Japan, September 6-7, **2018**.
45. Bakhshi F., Farhadian N., Co-doped graphene sheets as a novel adsorbent for hydrogen storage: DFT and DFT-D3 correction dispersion study. *International Journal of Hydrogen Energy*, Vol. 43, **2018**, pp. 8355-8364.
46. Staykov A., Yamabe J., Somerday B. P., Effect of hydrogen gas impurities on the hydrogen dissociation on iron surface. *International Journal of Quantum Chemistry*, Vol. 114, **2014**, pp. 626– 635.
47. Somerday B. P., Sofronis P., Nibur K.A., et al, Elucidating the variables affecting accelerated fatigue crack growth of steel in hydrogen gas with low oxygen concentrations, *Acta Materialia*, Vol. 61, **2013**, pp. 6153-6170.
48. Staykov A., Komoda R., Kubota M., et al, Coadsorption of CO and H_2 on an Iron Surface and Its Implication on the Hydrogen Embrittlement of Iron. *The Journal of Physical Chemistry C*, Vol. 123, **2019**, pp. 30265 – 30273.
49. Gunasooriya G. T., et al, CO Adsorption on Pt (111): From Isolated Molecules to Ordered High-Coverage Structures, *ACS Catalysis*, Vol. 8. **2018**, pp. 10225-10233.
50. Louthan M. R., Swanson R. E., Material defects, gas purity and hydrogen embrittlement, *International Journal of Hydrogen Energy*, Vol. 10, **1985**, pp. 551-554.
51. Woodtli J., Kieselbach R., Damage due to hydrogen embrittlement and stress corrosion cracking, *Engineering Failure Analysis*. Vol. 7, **2000**, pp. 427-450.
52. Maksimovich G. G., Bichuya A. L., Nikiforov Y. D., Relationship of the strength properties of metals to their catalytic activity, *Materials Science*, Vol. 19, **1984**, pp. 393-397.

53. Srikrishnan V., Selective adsorption and hydrogen embrittlement. Metallurgical transactions. A, *Physical metallurgy and materials science*, Vol. 11, **1976**, pp. 1669-1675.
54. Giustino F., Materials Modelling Using Density Functional Theory: Properties and Predictions, *Oxford University Press*, New York, **2014**.
55. Kane E., Thomas-Fermi Approach to Impure Semiconductor Band Structure, *Physical Review Journals*, Vol. 131, **1963**, pp. 79-88.
56. Gilbert T. L., Hohenberg-Kohn theorem for nonlocal external potentials, *Physical Review B*, Vol.12, **1975**, pp. 2111-2120.
57. Shao X., et al, GGA-Level Subsystem DFT Achieves Sub-kcal/mol Accuracy Intermolecular Interactions by Mimicking Nonlocal Functionals, *Journal of Chemical Theory and Computation*, Vol.17, **2021**, pp. 3455-3461.
58. Grindy S., et al, Approaching chemical accuracy with density functional calculations: Diatomic energy corrections, *Physical Review B*, Vol. 87, **2013**, pp. 7-15.
59. Dubinin A., et al, Lattice dynamics and elastic properties of PbF_2 and BaF_2 from quantum mechanical calculations, *The European Physical Journal B*, Vol.39, **2004**, pp. 27-33.
60. Jones R.O., Density functional theory: Its origins, rise to prominence, and future, *Reviews of Modern Physics*, Vol. 87, **2015**, pp. 897-923.
61. Cong T. V., Lam K. H., Hung J. Y., Jiang J. C., Methanol adsorption and decomposition on ZnO surface: A density functional theory study, *Applied Surface Science*, Vol. 280, **2013**, pp. 219-224.
62. Wang T., Tian X. X., Li Y. W., et al, Coverage-Dependent CO Adsorption and Dissociation Mechanisms on Iron Surfaces from DFT Computations, *ACS Catalysis*, Vol. 4, **2014**, pp. 1991-2005.
63. Duan X. Z., Ji J., Qian G., et al, Ammonia decomposition on Fe (110), Co (111) and Ni (111) surfaces: A density functional theory study, *Journal of Molecular Catalysis A*: *Chemical*, Vol. 357, **2012**, pp. 81-86.

64. Sang C. Y., Sang S. H., Hyuck M. L., Mechanistic Investigation of the Catalytic Decomposition of Ammonia (NH_3) on an Fe (100) Surface: A DFT Study, *The Journal of Physical Chemistry C*, Vol. 118, **2014**, pp. 5309-5316.
65. Chelikowsky J. R., Louie S. G., First-principles linear combination of atomic orbitals method for the cohesive and structural properties of solids: Application to diamond, *Physical Review B*, Vol. 29, **1984**, pp. 6-15.
66. Smidstrup S., Markussen T., et al, Quantum ATK: an integrated platform of electronic and atomic-scale modelling tools, *Journal of Physics: Condensed Matter*, Vol. 32, **2019**, pp. 1-36.
67. Lindauer M. W., The evolution of the concept of chemical equilibrium from 1775 to 1923, *Journal of Chemical Education*. Vol.39, **1962**, pp. 384-390.
68. Langmuir I., The Adsorption of Gases on Plane Surface of Glass, Mica and Platinum, *Journal of the American Chemical Society*. Vol. 40, **1918**, pp. 1361-1402.
69. Langmuir I., "Part I" The Research Laboratory of the General Electric Company: 2221, **1916**.
70. Langmuir I., "Part II" The Research Laboratory of the General Electric Company: 1848, **1918**.
71. Arrhenius S. Quantitative relationship between the rate a reaction proceed and its temperature, *Journal of Physical Chemistry*, Vol. 4, **1889**, pp. 226-248.

2 Mitigation effect of ammonia on hydrogen-assisted degradation of fracture toughness

2.1 Introduction

In the reduction of CO_2 emissions through the increase of renewable energies, the use of hydrogen energy is one of the promising solutions and NH_3 is vital for a carbon-neutral society as described in the previous chapter [2 - 1, 2 - 2]. However, hydrogen causes degradation of material strength properties, which is generally termed hydrogen embrittlement (HE), such as ductility loss in tensile test, fatigue crack growth acceleration, and fracture toughness reduction [2 - 3-2 - 5]. In the gaseous hydrogen environment, hydrogen uptake from the environment into the material is the first step for HE. In the process of hydrogen uptake at room temperature, dissociation of hydrogen molecules into hydrogen atoms assisted by catalysis of iron (Fe) surface is necessary [2 - 6]. In this context, if the catalysis of the Fe surface is deactivated, it mitigates HE.

When some specific impurities that are having a higher affinity for Fe surface than hydrogen are contained in hydrogen gas, they preferentially adsorb on the Fe surface. The adsorbed impurities localize the electron density on the Fe surface resulting in the deactivation of catalysis of the Fe surface for the hydrogen dissociation [2 - 7, 2 - 9]. Consequently, hydrogen uptake is suppressed and then HE is mitigated [2 - 7 - 2 - 12]. Oxygen (O_2) and carbon monoxide (CO) are well known as the mitigator of HE [2 - 7, 2 - 8, 2 - 13]. Somerday et al. studied the mitigation effect of O_2 on hydrogen-accelerated fatigue crack growth of line pipe steel [2 - 7]. They clarified that the O_2 mitigation effect is governed by the competition between the rate of bare Fe surface creation by the crack growth and the rate of passivation of the bare Fe surface by O_2. They established an analytical predictive model of the onset of the hydrogen-accelerated fatigue crack growth in the presence of O_2. This is the first quantitative and predictive model for hydrogen embrittlement in the presence of O_2. It was known that CO has mitigation of hydrogen effect [2 - 8]. Komoda et al. carried out systematic experiments to clarify the influential factors in the CO's HE mitigation. Based

on the result, they discussed the difference between the mitigation effects of O_2 and CO [2 - 8, 2 - 11, 2 - 12, 2 - 16]. Thanks to the computational experiment, they clarified that the difference in the reaction rate of the impurities with the Fe surface is the key factor that controls the mitigation behavior. Staykov et al. showed that the CO mitigation effect decreased with a decrease in the loading rate [2 - 10]. They conducted density functional theory (DFT) calculations and elucidated that CO can suppress the hydrogen uptake but cannot completely prevent it due to its imperfect coverage (75% Max) of the Fe (110) surface. Decreasing the loading rate increases the time for hydrogen uptake. It results in HE even if CO reduces hydrogen flux.

Other than O_2 and CO, SO_2 [2 - 14], COS, C_2H_6, C_2H_4, CH_3SH, and CF_2CFCl [2 - 13] are reported to mitigate HE. On the other hand, H_2S induces HE by producing H atoms by its dissociation into S and 2 H atoms when an aqueous environment coexists [2 - 14]. The H-S bonding energy of the H_2S molecule is lower than the H-H one of the H_2 molecule [2 - 15]. Therefore, more amount of hydrogen can be provided to the material by H_2S than by H_2.

Regarding the mitigation effect of HE by NH_3, the number of studies is very limited. Srikrishnan et al. reported that NH_3 mitigated hydrogen-assisted crack growth of iron [2 - 14]. They carried out the crack growth experiment of 4340 steel under H_2 gas and H_2 gas mixed with 50 ppm in volume (vppm) NH_3 at 330 Pa of gas pressure, The result showed that the 50 vppm NH_3 significantly reduced the crack growth speed compared with that in the pure H_2. In this work, however, the NH_3's HE induction effect was not found.

The objective of this chapter is to characterize the effect of NH_3, which was added to H_2 gas as an impurity, on the HE of low-alloy steel and to elucidate the mechanism of NH_3 mitigation on HEE. To fulfill it, the fracture toughness tests of JIS SCM440 Cr-Mo low alloy steel were carried out in nitrogen (N_2), hydrogen (H_2), and NH_3 mixed H_2 gases at 0.1 MPa. The first-principal calculation on the molecular coadsorption of NH_3 and H_2 on the Fe (110) surface was carried out to examine the mechanism.

Furthermore, to gain a better understanding of NH_3, the effect of NH_3 itself on the fracture toughness was investigated by the fracture toughness test in $N_2 + NH_3$ mixture in the next chapter.

2.2 Experimental procedure

2.2.1 Material

The material used in this study was JIS SCM440 Cr-Mo low-alloy steel. The chemical composition is shown in Table 2.1. The heat treatments were quenching following heating at 1143 K for 2 h, sub-zero treatment, and tempering at 842 K for 5 h. The mechanical properties after the heat treatments are shown in Table 2.2. The microstructure of the material is shown in Fig. 2.1. It exhibits the tempered martensite microstructure.

Table 2.1. Chemical composition of SCM440 (mass %)

C	Si	Mn	P	S	Cu	Ni	Cr	Mo
0.40	0.22	0.63	0.008	0.004	0.02	0.02	0.94	0.15

Table 2.2. Mechanical properties of SCM440

0.2% proof strength (MPa)	Ultimate tensile strength (MPa)	Elongation	Reduction of area	Vickers Hardness
841	971	20%	54%	HV329

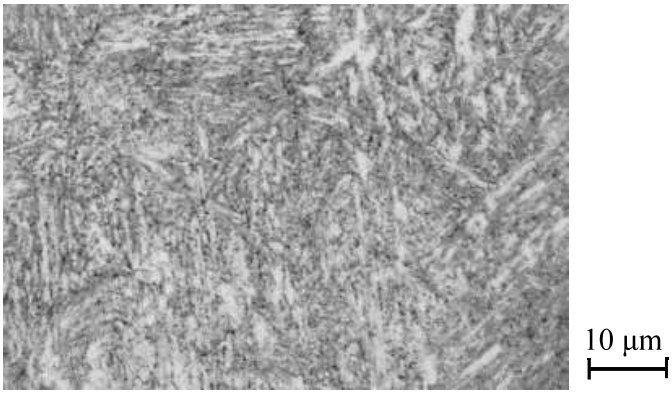

Fig. 2.1 Microstructure of the material

2.2.2 Fracture toughness test method and test environment

Fracture toughness tests were carried out in accordance with the ASTM E 1820 standard. Figure 2.2 shows the shape and sizes of the compact tension (CT) specimen. The CT specimen had a 30-mm width and 8-mm thickness. Side grooves, which are 1 mm in depth, 0.3 mm in root radius, and 60 degrees in opening angle, were machined in order to ensure a straight crack front. The effective thickness calculated in accordance with the standard was 7.5 mm. A pre-crack was introduced by a fatigue test in the air. The pre-crack length including the machined notch was 17 mm.

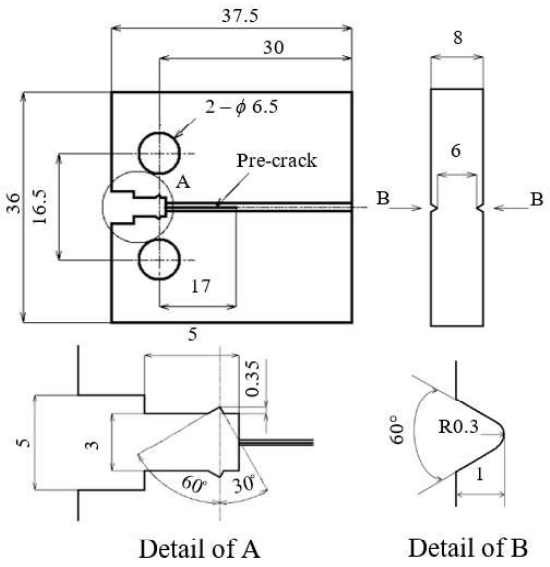

Fig. 2.2 Shape and sizes of CT specimen (dimensions are in mm)

Figure 2.3 shows the testing system. The test environments were H_2, N_2, and NH_3 added H_2 gases. The amount of NH_3 in the mixed gases was 1,000 and 10,000 vppm. The purity of the environment of gases was measured by a gas chromatograph installed at the outlet of the gas chamber. Since 1 vppm O_2 can work as a mitigator of the HEE [2 - 12], the amount of O_2 in these gases was limited to 0.1 vppm or less. The high purity gas condition

in the gas chamber was carefully produced by five sets of evacuation and N_2 gas purge. The measurement of impurity amount in the gas stored in the gas chamber was measured immediately before and after the test. Meanwhile, the gas flow was kept during the test to maintain gas purity. The continuous supply of high-purity gas is critically important. The load cell was installed inside the gas chamber to measure the load accuracy.

The total absolute gas pressure at which the fracture toughness tests were carried out, p_T, was 0.1 MPa. The gas temperature was controlled at 293 K by a thermocouple installed near the CT specimen and a heater and cooler system. The crosshead speed, V, was 2.0×10^{-3} mm/s.

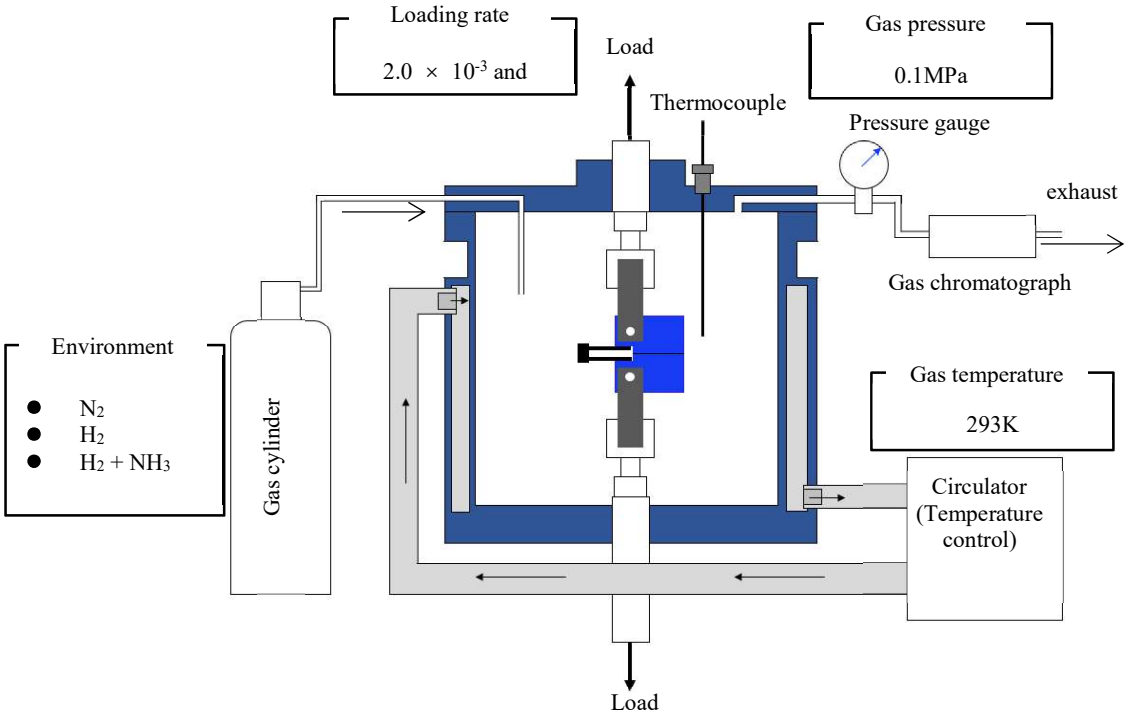

Fig. 2.3 Fracture toughness testing system

2.3 Test results

2.3.1 Test results

The results of the fracture toughness tests in the H_2, N_2, and NH_3 added H_2 gases are shown in Fig. 2.4. The elastic-plastic fracture toughness values, J_{IC}, for each condition are shown in Table 2.3. Figure 2.4 shows the J-Δa curves under the testing conditions of p_T = 0.1 MPa and $V = 2.0 \times 10^{-3}$ mm/s. The J-Δa curve in the H_2 gas (▲) was located at a lower level than that in the N_2 gas (●). As a result, the J_{IC} value in the H_2 gas was lower than that in the N_2 gas. The J-Δa curves in the NH_3 added H_2 gases (■, ◆), were initially almost the same as that in N_2 or located slightly lower level than that in the N_2 gas. Consequently, the J_{IC} values in both the 1,000 and 10,000 vppm NH_3 added H_2 gases. It was found that the addition of NH_3 to the H_2 gas effectively prevented the HE under the testing conditions of p_T = 0.1 MPa and $V = 2.0 \times 10^{-3}$ mm/s. The J-Δa curve in the NH_3 added H_2 gases approached the J-Δa curve in the H_2 gas after the start of the stable crack propagation. The effect of NH_3 addition to the H_2 gas during crack propagation should be separately investigated.

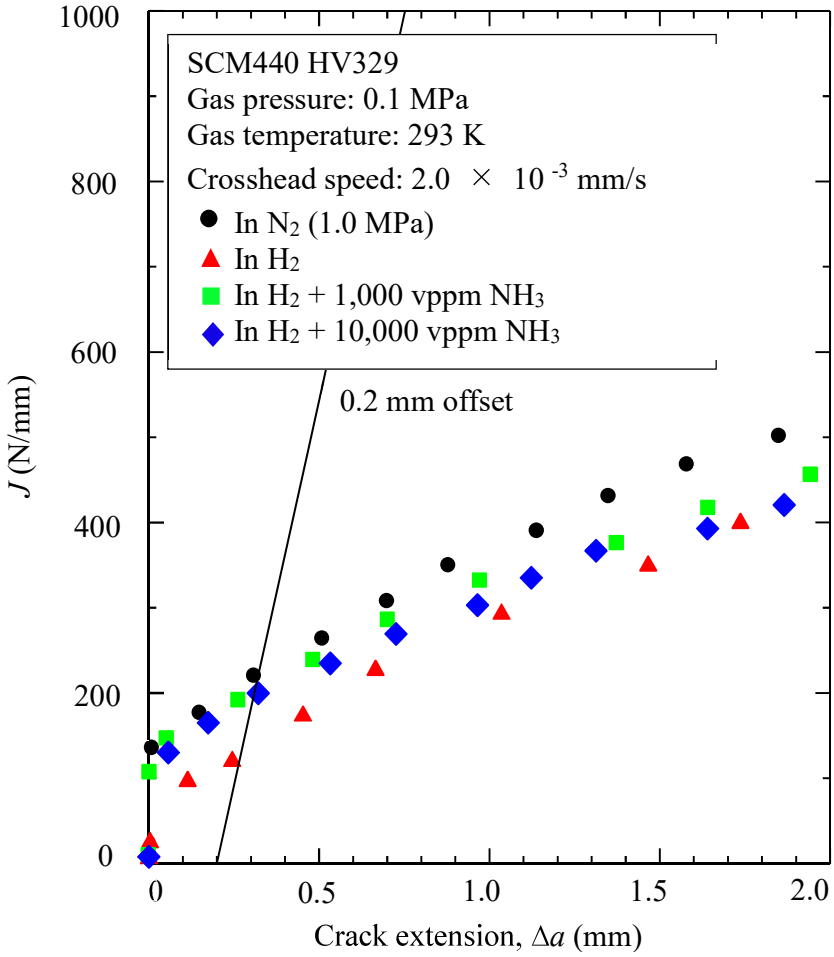

Fig. 2.4 Effect of NH_3 addition to H_2 environment on J-Δa curve at p_T = 0.1 MPa and $V = 2.0 \times 10^{-3}$ mm/s.

Table 2.3. J_{IC} value in each condition. [---]: Relative value to J_{IC} in N_2

Environment	N_2	H_2	H_2 + 1,000 ppmNH_3	H_2 + 10,000 ppmNH_3
p_T = 0.1 MPa, $V = 2.0 \times 10^{-3}$ mm/s	217 (1.0 MPa) [1]	128 [0.59]	202 [0.93]	197 [0.91]

p_T : Total environmental gas pressure

V : Cross head displacement rate

2.3.2 Fracture surface

Figure 2.5 shows the fracture surfaces created during the fracture toughness test. The photographs show the fracture surfaces at the middle of the specimen thickness and at the crack length corresponding to J_{IC}. Dimple fracture was observed in the N_2 as shown in Fig. 2.5 (a) and quasi-cleavage (QC) fracture was observed in the H_2 as shown in Fig. 2.5 (b). Similar results were observed in the same kind of low alloy steel having a comparable material strength [2 - 16, 2 - 17]. In the case when NH_3 fully mitigated the HEE, e.g., the fracture toughness test in the 1,000 vppm NH_3 added H_2 gas at p_T = 0.1 MPa with $V = 2 \times 10^{-3}$ mm/s, a dimple fracture surface was observed as shown in Fig. 2.5 (c). The morphology of the dimple was very similar to that in the N_2 gas. The change in the fracture surface in the H_2 gas by the addition of NH_3, which was from the QC to dimple, suggested that NH_3 prevented hydrogen entry followed by the deactivation of the catalytic action of the Fe surface for the dissociation of molecular H_2 into atomic hydrogen.

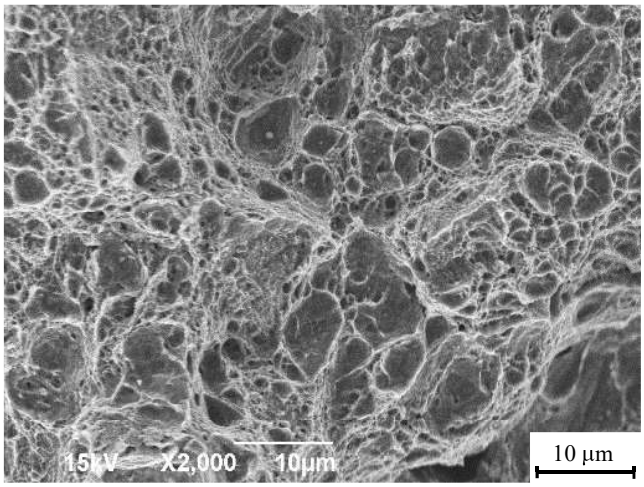

(a) In N_2, p_T = 1.0 MPa,
$V = 2.0 \times 10^{-3}$ mm/s, J_{IC} = 217 N/mm

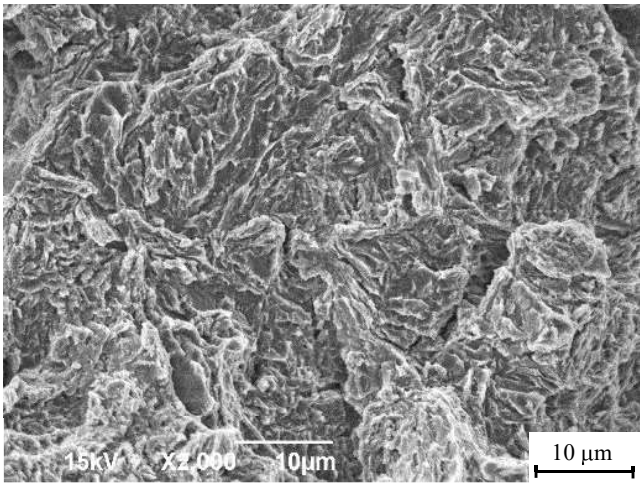

(b) In H_2, p_T = 0.1 MPa,
$V = 2.0 \times 10^{-3}$ mm/s, J_{IC} = 128 N/mm

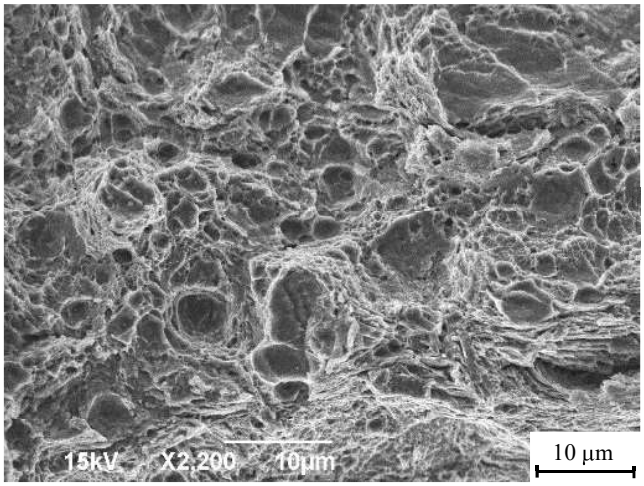

(c) In 1,000 vppm $NH_3 + H_2$, p_T = 0.1 MPa,
$V = 2.0 \times 10^{-3}$ mm/s, J_{IC} = 202 N/mm

Fig. 2.5 Fracture surfaces

2.4 Discussion on the mechanism of ammonia mitigation of hydrogen embrittlement based on density functional theory calculations

From the result of the fracture toughness test and fracture surface observation, it was found that NH_3 added to H_2 gas mitigated HE. By considering the mitigation effect of O_2 and CO [2 - 7 - 2 - 12], the mitigation effect of gas impurities on HE is achieved by deactivation of catalysis of Fe surface for hydrogen dissociation. In detail, gas impurities having a higher affinity for the Fe surface than H_2 molecules, such as O_2 and CO, preferentially adsorb on the Fe surface and then suppress electron donation from the Fe surface to the hydrogen molecule that is necessary for its dissociation [2 - 18]. Therefore, whether or not the mitigation effect of impurity appears depends on the competition of affinities between H_2 and impurity on the Fe surface.

As shown in Fig. 2.4, the mitigation effect of NH_3 at 0.1 MPa with the crosshead speed of 2.0×10^{-3} mm/s was not changed with the increase in the NH_3 concentration from 1,000 to 10,000 vppm. The same trend has been reported that the increase in the impurity concentration not increased the mitigation effect in O_2 [2 - 12] and CO impurities [2 - 8] after it reaches the maximum coverage on the surface. During material strength tests involving crack extensions, such as fracture toughness test and fatigue crack growth test, the mitigation effect of gas impurities is governed by the competition between the rate of fresh Fe surface creation by the crack extension and the rate of surface coverage by the impurity [2 - 7]. Thus, a higher adsorption rate of impurity brings a higher mitigation effect. The result that 1,000 vppm NH_3 completely prevented the HE at 0.1 MPa indicates that the adsorption rate of NH_3 was sufficiently higher than that of H_2. Thus, the increase in the NH_3 concentration had no effect on the NH_3 mitigation effect at 0.1 MPa even though the increase in the NH_3 concentration may increase NH_3 adsorption rate.

Above all, investigation of the competitive coadsorption reaction between H_2 and NH_3 with Fe (110) surface is the key to understanding NH_3 effects. Then, I investigated the

adsorption energy, electron density, and reaction rate of NH_3 and H_2 molecules adsorption by theoretical calculations, respectively. In addition, I calculated the coverage of competitive molecular coadsorption of NH_3 and H_2 on the Fe (110) surface by the computational experiment by DFT.

2.4.1 Adsorption site and adsorption energy of ammonia and hydrogen on Fe (110) surface

I optimize the lattice of Fe (110) surface and obtain a lattice constant of 2.63Å, which agrees with previous reports in the literature [2 - 20]. The surface optimization yields a slightly shorter distance between the first and second later and a slightly longer distance between the second and third layers.

I first investigate the surface geometry and surface occupation by NH_3 molecules. The Fe (110) surface offers three distinct adsorption positions for the NH_3 molecules as shown in Fig. 2.6 (a), (b), (c), and all the initial geometry end on the top site of the Fe (110) surface as shown in Fig. 2.6 (d) after optimizing the geometry. Those are the top position (as shown in Fig. 2.6(a)), bridge position (as shown in Fig. 2.6(b)), and hollow position (as shown in Fig. 2.6(c)). The NH_3 molecule interacts with the Fe (110) surface in an end-on configuration with the nitrogen atom facing-exposed Fe atoms on the top site (as shown in Fig. 2.7(d)). I examined the adsorption energy of NH_3 on Fe (110) to determine the effect of surface coverage. The adsorption energy of different coverage NH_3 on Fe (110) is shown in Table 2.4. The adsorption energy of NH_3 on the Fe (110) surface is decreased with NH_3 coverage increasing, therefore, NH_3 adsorbed on the Fe (110) surface is harder. The main reason for this phenomenon can be considered for two reasons: 1) previous adsorbed NH_3 withdrawn and localized the electron density of the Fe surface, thus the electron density of the adjacent site is no longer enough for the following NH_3 adsorption; 2) the repulsive interactions between the NH_3 molecules. The most stable surface geometry is NH_3 molecules occupying top sites from 11.11% coverage to 33.33% coverage. Thus, each NH_3 molecule interacts with one iron atom on the surface, while H_2 interacts with two iron atoms.

I further investigate the H_2 dissociation process on the pure Fe (110) surface and Fe (110) surface preferentially covered by NH_3 with different coverage, the geometry as shown in Fig. 2.7. The activation energy barrier and dissociation energy of H_2 on the Fe (110) surface is shown in Table 2.5. Without NH_3 pre-adsorbed on the Fe (110) surface, the H_2 directly dissociates on Fe (110) surface without an activation energy barrier. The dissociation

energy of H_2 is -1.56 eV. At 11.11% coverage, the activation energy barrier for H_2 dissociation on Fe (110) surface is 0.04 eV, and the dissociation energy of H_2 is -1.54 eV. Though the dissociation energy slightly increased, the activation energy barrier changed from 0.00 eV to 0.04 eV, which indicates that even at low coverage NH_3 can hinder the effect on H_2 dissociation. With the increase of NH_3 coverage on the Fe (110) surface from 11.11% to 33.33%, the activation energy barrier of H_2 dissociation is increased, and the dissociation energy of H_2 is decreased. The activation energy barrier would reduce the H_2 dissociation reaction rate. Decreasing the dissociation energy of H_2 would make H_2 molecule desorption on the Fe surface easier. As a result, an increased activation energy barrier and decreased dissociation energy would lead to a decrease in the hydrogen atom concentration on the surface. In the other words, the higher the coverage rate of NH_3 on Fe (110), the more difficult for the Fe surface to dissociate H_2, fewer hydrogen atoms permeate to Fe, and less HEE.

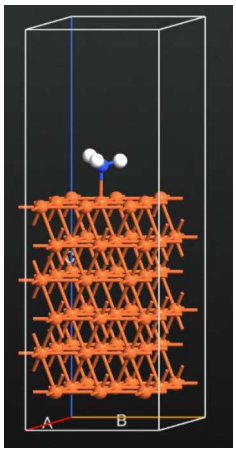

(a) Top

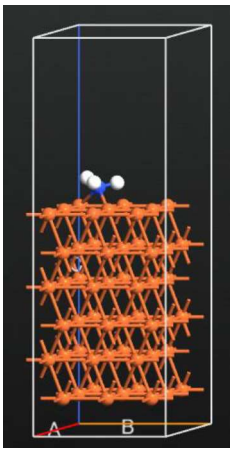

(b) Bridge

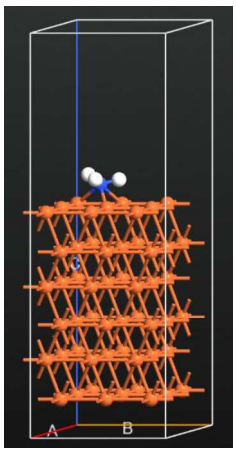

(c) Hollow

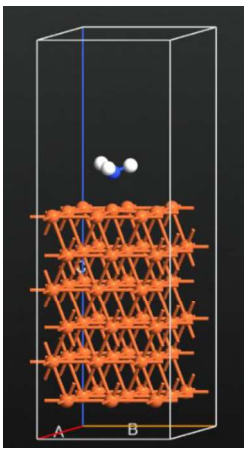

(d) Optimized end-on Top

Fig. 2.6 Adsorption geometry of NH_3 molecule at top (a), bridge (b), and hollow (c) as initial position. The top site is the end position (d).

Table 2.4 Adsorption energy of NH_3

Coverage	11.11% NH_3 Adsorbed on Fe (110)	25.00% NH_3 Adsorbed on Fe (110)	33.33% NH_3 Adsorbed on Fe (110)
Adsorption energy (eV)	-1.01	-0.94	-0.93

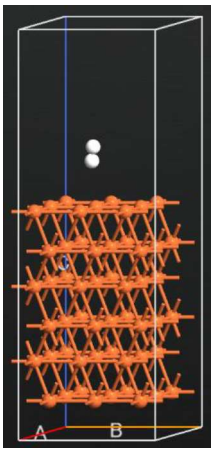

(a) H_2 dissociation on Fe (110) surface

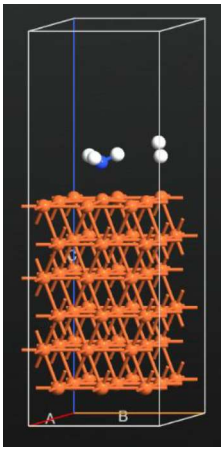

(b) H_2 dissociation on 11.11% NH_3 preferentially adsorbed Fe (110) surface

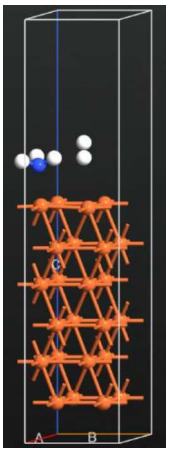

(c) H_2 dissociation on 25.00% NH_3 preferentially adsorbed Fe (110) surface

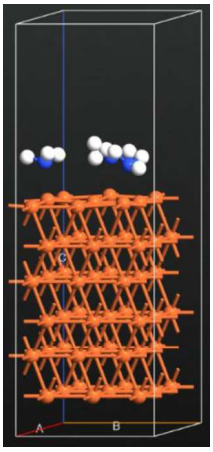

(d) H_2 dissociation on 33.33% NH_3 preferentially adsorbed Fe (110) surface

Fig. 2.7 Molecular hydrogen dissociation on the Fe (110) surface with (a) 0.00% NH_3 coverage, (b) 11.11% NH_3 coverage, (c) 25.00% NH_3 coverage, (d) 33.33% NH_3 coverage

Table 2.5 Dissociation energy of H_2

Coverage	0.00% NH_3 pre-adsorb Fe (110)	11.11% NH_3 pre-adsorb Fe (110)	25.00% NH_3 pre-adsorb Fe (110)	33.33% NH_3 pre-adsorb Fe (110)
Activation energy (eV)	0.00	0.04	0.06	0.07
Dissociation energy (eV)	-1.56	-1.54	-1.22	-1.17

2.4.2 Electron density of ammonia and hydrogen on Fe (110) surface

I investigate the electron density of NH_3 and H_2 on the Fe (110) surface, respectively. The electron density is an intuitive measure of the probability that an electron exists in an infinitesimal element around any point in space [2 - 21]. The electron density is the key to the bonding and geometry because the force holding the nuclei together in a molecule is the attractive force between the electron and nuclei. Thus, the higher electron density represents the higher attractive force. The electron density of NH_3 on the Fe (110) surface is 0.5 eV/Å^3, while the electron density of H_2 is 0.1 eV/Å^3. Therefore, the Fe (110) surface has a significantly higher electronic interaction for NH_3 than H_2.

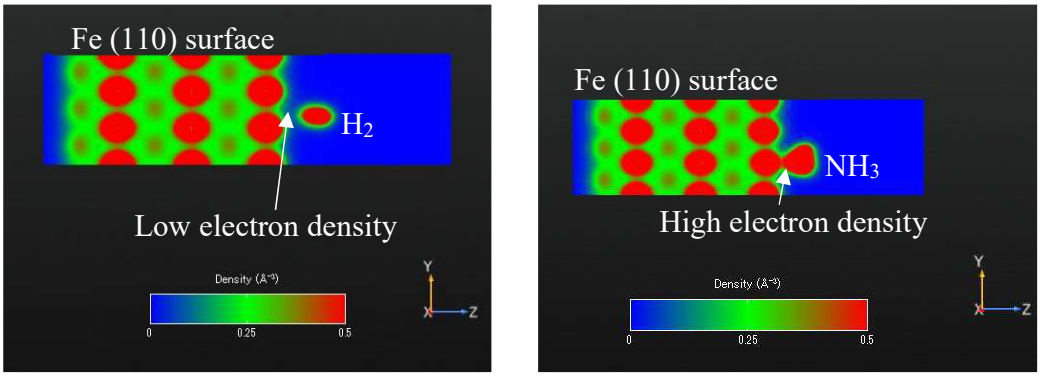

(a) H_2 (b) NH_3

Fig. 2.8 Electron density of H_2 (a) and NH_3 (b) on Fe (110) surface.

2.4.3 The Langmuir adsorption model for competitive adsorption of ammonia and hydrogen on Fe (110) surface

As described in chapter 1.5.3, I performed the Langmuir adsorption model, which assumes the adsorbate behaves as an ideal gas under isothermal conditions [2 - 10, 2 - 22]. According to the Langmuir competitive adsorption model in eqs 1.2 and 1.3, and because H_2 is dissociative adsorption on the Fe surface, a molecule of H_2 is dissociated into two hydrogen atoms. The 1/2 exponent on H_2 arises because it produces two species on the surface. I used the data in Tables 2.4 and 2.5 to modify the Langmuir competitive adsorption model for the competitive NH_3 and H_2 coadsorption on the Fe (110) surface. The surface coverage equation for NH_3 adsorption and H_2 dissociative adsorption is given below (eqs 2.1 and 2.2, respectively). In those equations, θ_{NH_3} and θ_{H} are denoted the fractional occupancy on the surface by NH_3 or atomic hydrogen, respectively. The activation barriers for different NH_3 coverage are taken from the DFT calculations, the temperature is set to 293K, and high-purity H_2 was considered with 1,000 ppm and 10,000 ppm of NH_3 to match the experiment conditions. I used two different coverage models to represent the different NH_3 concentrations on H_2 gas because increased partial pressure would increase the coverage [2 - 23]. Thus, 1 NH_3 on the 9 Fe model represents 1,000 ppm NH_3 in H_2, and 1 NH_3 on the 4 Fe model represents 10,000 ppm NH_3 in H_2.

$$\theta_{NH_3} = \frac{P_{NH_3}K_{NH_3}}{1+P_{NH_3}K_{NH_3}+\sqrt{P_{H_2}K_{H_2}}} \tag{2.1}$$

$$\theta_{\mathrm{H}} = \frac{\sqrt{P_{H_2}K_{H_2}}}{1+P_{NH_3}K_{NH_3}+\sqrt{P_{H_2}K_{H_2}}} \tag{2.2}$$

In eqs 2.1 and 2.2 K_{NH_3} and K_{H_2} denote the NH_3 and H_2 adsorption/desorption equilibrium constants for activation barriers listed in Tables 2.4 and 2.5, which were calculated by DFT. The equilibrium constants are computed as the ratio between the adsorption and the desorption rate constants. P_{NH_3} and P_{H_2} denote the partial pressure of NH_3 and H_2, respectively. The rate constants were estimated using the Arrhenius relation in eq 1.4, where A is a preexponential factor, R is the gas constant, T is the temperature, and the E_a is the activation barrier taken from Table 2.4 and 2.5 and computation with DFT.

From my cooperative adsorption/desorption/dissociation model in eqs 2.1 and 2.2, I calculated the NH_3 and atomic hydrogen coverage on the Fe surface with different NH_3 concentrations, the result is shown in Table 2.6. The hydrogen atom coverage on the Fe (110) surface is decreasing with increasing the NH_3 coverage, which is achieved by increasing NH_3 concentration. Though there is no study related to the threshold hydrogen atom coverage on the iron surface is able to induce HE. Prof. Staykov et al. reported that hydrogen atom coverage on the iron surface is 0.60%, which is a chained by CO 75.00% coverage at 2.0×10^{-3} mm/s loading rate, is able to mitigate the HE. For NH_3, when NH_3 achieved 25.00% coverage on the Fe (110) surface, atomic hydrogen coverage is 0.01%, which is less than 0.60%. Therefore, I can conclude that NH_3 is able to mitigate HE at 2.0×10^{-3} mm/s based on the condition that NH_3 has a faster adsorption rate than H_2. The reaction rate will be calculated in the next section.

Table 2.6 Coverage of NH_3 and atomic hydrogen on Fe (110) surface

Condition	H_2 + 1,000ppm NH_3	H_2 + 10,000ppm NH_3
θ_{NH_3}	10.00%	25.00%
θ_{H}	1.70%	0.01%

2.4.4 Reaction rate of ammonia and hydrogen on Fe (110) surface

Surface reactions can be classified into two generic types. The first includes reactions between two adsorbed species or between an adsorbed species and a vacant site (Langmuir-Hinshelwood process), which is fitting for my consideration of coadsorption between NH_3 and H_2. The second reaction is called the Eley-Rideal process, which is considering an adsorbed species to form a product.

Based on the Langmuir-Hinshelwood process, for randomly distributed adsorbates on a surface in the absence of adsorbate-adsorbate interactions, the rate of reaction is given by eq 2.3.

$$r_r = k\theta_A\theta_v \tag{2.3}$$

Where k is the rate coefficient, θ_A is the surface coverage of species A (B), and θ_V is the fraction of the vacant sites. If k follows an Arrhenius expression (eq 1.4), then I calculated the pre-exponential factor (frequency factor) of NH_3 and H_2 using DFT for calculating their reaction rate of them respectively (eq 1.5). Table 2.7 is shown the pre-exponential factor of NH_3 and H_2 on the Fe (110) surface. Table 2.8 is shown the reaction rate coefficient of NH_3 and H_2 on the Fe (110) surface based on equation 1.4. According to table 2.6, 2.8, and equation 2.3, the value of reaction rate of NH_3 and H_2 adsorption in Table 2.9.

Table 2.7 Pre-exponential factor of NH_3 and H_2

	NH_3	H_2
A (Hz)	3.18×10^{20}	3.90×10^{11}

Table 2.8 Reaction rate coefficient k of NH_3 and H_2 adsorption

	NH_3	H_2
k (s^{-1})	3.14×10^{20}	3.92×10^{11}

Table 2.9 Reaction rate of NH_3 and H_2 adsorption

	NH_3	H_2
$r_{r\ (11.11\%NH_3)}$ (s^{-1})	2.77×10^{19}	5.85×10^{9}
$r_{r(25.00\%NH_3)}$ (s^{-1})	5.88×10^{19}	2.92×10^{7}

With increasing the coverage of NH_3 from 11.11% to 25.00%, the reaction rate of H_2 with the Fe (110) surface is decreasing from 5.85×10^9 s^{-1} to 2.92×10^7 s^{-1}. It is indicated that the H_2 probability of hydrogen entry into the Fe was declined by NH_3 coverage increase. On the other hand, the reaction rate of NH_3 is significantly faster than H_2, which indicates that NH_3 preferentially adsorbs on the Fe (110) surface more than H_2. Considering the coverage calculation result in the previous section, in conclusion, NH_3 can mitigate HE.

2.5 Conclusion

Fracture toughness tests of low-alloy steel SCM440 were conducted in an NH_3 added H_2 gas environment in order to characterize the effect of the NH_3 addition to H_2 gas on the HE. To understand the mechanism that NH_3 mitigated HE, the adsorption site, adsorption energy, the electron density, the reaction rate, and the coverage of NH_3 and H_2 were calculated by DFT. The main results achieved in this chapter are as follows:

1. The electron density of NH_3 on the Fe (110) surface was 0.5 eV/Å^3, while the electron density of H_2 on the Fe (110) surface was 0.1 eV/Å^3. Therefore, the attractive force of the Fe (110) surface for NH_3 is higher than H_2, NH_3 has a stronger affinity with Fe (110) than H_2.
2. The reaction rate of 11.11% NH_3 on the Fe (110) surface is 2.77×10^{19} s^{-1}, while the reaction rate of H_2 on the Fe (110) surface is 5.88×10^{9} s^{-1}. Therefore, the reaction rate of NH_3 on the Fe (110) surface is significantly higher than H_2 on Fe (110) surface, which indicates that NH_3 is preferentially adsorbed on the Fe (110) surface compared with H_2.
3. When coverage of NH_3 on Fe (110) surface is reached 25.00%, the atomic hydrogen coverage on Fe (110) surface is 0.01%. Therefore, NH_3 can mitigate the HE at the loading rate was 2.0×10^{-3} mm/s by preferentially adsorbed on the Fe surface and hindering Hydrogen uptake.
4. The reaction rate of H_2 on the Fe (110) surface was decreased from 5.88×10^{9} s^{-1} to 2.92×10^{7} s^{-1} by increasing NH_3 concentration from 11.11% to 25.00%.

2.6 References

1. Otto I. M., Donges J. F., Cremades R., et al, Social tipping dynamics for stabilizing Earth's climate by 2050, *Proceedings of the National Academy of Sciences*, Vol. 117, **2020**, pp. 2354-2365.
2. Aziz M., Oda T., Kashiwagi T., Comparison of liquid hydrogen, methylcyclohexane and ammonia on energy efficiency and economy, *Energy Procedia*, Vol. 158, **2019**, pp. 4086 -4091.
3. Hardie D., Liu S., The effect of stress concentration on hydrogen embrittlement of a low alloy steel, *Corrosion Science*, Vol. 38, **1996**, 721-733.
4. Townsend H.E. Effects of zinc coatings on the stress corrosion cracking and hydrogen embrittlement of low-alloy steel. *Metallurgical and Materials Transactions A*, Vol. 6, **1975**, pp. 877-883.
5. Lam P. S., Sindelar R. L., Duncan A. J., Adams T. M., Literature Survey of Gaseous Hydrogen Effects on the Mechanical Properties of Carbon and Low Alloy Steels. *Journal of Pressure Vessel Technology*, Vol. 131, **2009**, pp. 1-14.
6. Gangloff R. P. Gaseous hydrogen embrittlement of high strength steels. Metallurgical transactions. A, *Physical metallurgy and materials science*, Vol. 8, **1977**, pp. 1043-1053.
7. Somerday B. P., Sofronis P., Nibur K. A., et al, Elucidating the variables affecting accelerated fatigue crack growth of steel in hydrogen gas with low oxygen concentrations, *Acta Materialia*, Vol. 61, **2013**, pp. 6153-6170.
8. Komoda R., Yamada K., Kubota M., et al, The inhibitory effect of carbon monoxide contained in hydrogen gas environment on hydrogen-accelerated fatigue crack growth and its loading frequency dependency, *International Journal of Hydrogen Energy*, Vol. 44, **2019**, pp. 29007-29016.
9. Staykov A., Yamabe J., Somerday B. P., Effect of hydrogen gas impurities on the hydrogen dissociation on iron surface, *International Journal of Quantum Chemistry*, Vol. 114, **2014**, pp. 626-635.

10. Staykov A., Komoda R., Kubota M., et al, Coadsorption of CO and H_2 on an Iron Surface and Its Implication on the Hydrogen Embrittlement of Iron, *The Journal of Physical Chemistry C*, Vol. 123, **2019**, pp. 30265-30273.
11. Komoda R., Kubota M., Yoshida S., et al, Inhibition of Hydrogen Embrittlement of Cr-Mo Steel by the Addition of Impurities to Hydrogen Environment and the Effect of Material Strength. *Paper presented at the The 28th International Ocean and Polar Engineering Conference*, Sapporo, Japan, June **2018**.
12. Komoda R., Kubota M., Staykov A., et al, Inhibitory effect of oxygen on hydrogen-induced fracture of A333 pipe steel, *Fatigue & Fracture of Engineering Materials & Structures*, Vol. 42, **2019**, pp. 1387-1401.
13. Holbrook J.H., Cialone H.J., Collings E.W., et al, 5 - Control of hydrogen embrittlement of metals by chemical inhibitors and coatings, Editor(s): Richard P. Gangloff, Brian P. Somerday, In Woodhead Publishing Series in Metals and Surface Engineering, Gaseous Hydrogen Embrittlement of Materials in Energy Technologies, *Woodhead Publishing*, Vol. 1, **2012**, pp. 129-153.
14. Srikrishnan V., Selective adsorption and hydrogen embrittlement. *Metallurgical transactions. A, Physical metallurgy and materials science*, Vol. 11, **1976**, pp. 1669-1675.
15. JANAF Thermochemical Tables, The Dow Chemical Corp., Midland Mich., Aug. **1965**.
16. Komoda R., Kubota M., Staykov A., et al, Effect of Gas Pressure on Hydrogen Environment Embrittlement of Carbon Steel A106 in Carbon Monoxide Mixed Hydrogen Gas, *Metallurgical and Materials Transactiona A*, Vol. 53, **2022**, pp. 74-85.
17. Cho L., Bradley P.E., Lauria D.S., et al, Effects of hydrogen pressure and prior austenite grain size on the hydrogen embrittlement characteristics of a press-hardened martensitic steel, *International Journal of Hydrogen Energy*, Vol. 46, **2021**, pp. 24425-24439.
18. Lennard J., Processes of adsorption and diffusion on solid surfaces, *Transactions of the Faraday Society*, Vol. 28, **1932**, pp. 333-359.

19. Chelikowsky J. R., Louie S. G., First-principles linear combination of atomic orbitals method for the cohesive and structural properties of solids: Application to diamond, *Physical Review Journal B*, Vol. 29, **1984**, pp. 6-15.
20. Yan J. A., Wang C. Y., Wang S. Y., Generalized-stacking-fault energy and dislocation properties in bcc Fe: A first-principles study, *Physical Review Journal B*, Vol. 70, **2000**, pp. 1-5.
21. Matta C. F., Gillespie R. J., Understanding and Interpreting Molecular Electron Density Distributions, *Journal of Chemical Education*, Vol. 79, **2002**, pp. 1141-1152.
22. Staykov A., Fukumori S., Yoshizawa K., et al, Interaction of SrO-terminated $SrTiO_3$ surface with oxygen, carbon dioxide, and water, *Journal of Materials Chemistry A*, Vol. 6, **2018**, pp. 22662-22672.
23. Pekridis G., Kalimeri K., Kaklidis N., et al, Study of the reverse water gas shift (RWGS) reaction over Pt in a solid oxide fuel cell (SOFC) operating under open and closed-circuit conditions, *Catalysis Today*, Vol. 127, **2007**, pp. 337-346.

3 Induction effect of ammonia on hydrogen-assisted degradation of fracture toughness

3.1 Introduction

For a long time since the discovery of the NH_3 compound, scientists have focused on the synthesis of NH_3. Because NH_3 has a wide range of applications as described in chapter 1. While in recent years, with the need to transition to a carbon-neutral society and the development of hydrogen energy, NH_3 is considered an important carrier of hydrogen production by its decomposition in a hydrogen economy [3 - 1 - 3 - 5]. Therefore, catalytic performance and surface chemistry of NH_3 decomposition on Fe surface have derived attention [3 - 6 - 3 - 9].

As described in chapter 2, NH_3 can mitigate the HE, simultaneously according to the past studies [3 - 6 - 3 - 10] on the NH_3 decomposition on the Fe surface, NH_3 produced hydrogen with Fe surface catalytic action. Walerian Arabczyk et al. reported that the reaction rate of Fe catalyst NH_3 decomposition is a proportional relationship with the concentration of NH_3, which indicates that the reaction of gaseous NH_3 decomposition on the Fe surface is the first-order reaction [3 - 6]. Jian Ji et al reported that Fe (111) surface is more active than Fe (110) and Fe (100) surface for catalyst NH_3 decomposition [3 - 10]. Considering the role of NH_3 mixed with gaseous H_2, both HE mitigation and HE induction can be present at the same time. However, based on the current status of the study on the NH_3 effect on HE the mechanism remain unclear. For example, the reaction rate of NH_3 on the Fe surface and the coverage of NH_3-derived hydrogen coverage on the Fe surface, which are salient factors to determine the NH_3 effect, are unclear yet. Hence, my motivation in this chapter is to investigate the effect of NH_3 on HE itself on the Fe (110) surface.

In this chapter, the fracture toughness test of the Cr-Mo steel SCM440 was carried out at 293K in N_2 and NH_3 mixed N_2 gaseous environments to characterize the role of NH_3. As a result, HE was observed even in NH_3 mixed N_2 gas. It was presumed that the source of hydrogen was the decomposition of NH_3 with the assistance of the Fe surface. Therefore, the process of NH_3 decomposition on the Fe (110) surface was investigated with first-principle

calculations. In addition, I divided free gaseous NH_3 decomposition into nitrogen atoms and hydrogen atoms on Fe (110) surface into four steps, and calculated NH_3-derived hydrogen atom coverage on Fe (110) surface for each step to investigate the mechanism of NH_3 inducing HE.

3.2 Experimental procedure

3.2.1 Material

The material used for this section was JIS SCM440 Cr-Mo low-alloy steel, which is the same material used in chapter 2. The heat treatment conditions are the same as that in chapter 2. The chemical composition and mechanical properties are shown in Tables 2.1 and 2.2 in chapter 2, respectively. The microstructure of the material exhibits the tempered martensite microstructure is shown in Fig. 2.1 in chapter 2.

3.2.2 Fracture toughness test method and test environment

The fracture toughness tests were conducted in the accordance with the ASTM E 1820 standard with the same fracture toughness test system in chapter 2. The fracture toughness test method and the CT specimen were the same as that used in chapter 2.

The test environments were N_2, H_2 and NH_3 added N_2 gases. The amount of NH_3 in the mixture was 1,000 vppm. The purity measurement of the testing environment and the method for keeping the high purity gas condition in the gas chamber were the same as described in chapter 2.

The total gas pressure at which the fracture toughness tests were carried out, p_T, was 0.1 MPa. The gas temperature was controlled at 293K by a thermocouple installed near the CT specimen and a heater and cooler system. It can be considered that NH_3 decomposition is a time-dependence phenomenon, a slower crosshead speed, which was 2.0×10^{-5} mm/s, was added to the crosshead speed used in chapter 2 (2.0×10^{-3} mm/s).

3.3 Test results

3.3.1 Test results

The results of the fracture toughness tests in the H_2, N_2, and NH_3 added N_2 gases are shown in Figs. 3.1 and 3.2. The elastic-plastic fracture toughness values, J_{IC}, for each condition are shown in Table 3.1.

Figure 3.1 shows the J-Δa curves under the testing conditions of p_T = 0.1 MPa and $V = 2.0 \times 10^{-3}$ mm/s. The J-Δa curve in the H_2 gas (▲) was located at a lower level than that in the N_2 gas (●). As a result, the J_{IC} value in the H_2 gas was lower than that in the N_2 gas. The J-Δa curve in the 1,000 ppm NH_3 added N_2 gases ( ) was initially almost the same as that in the N_2. As a result, the J_{IC} value in the NH_3 added to N_2 was almost the same as the J_{IC} value in the N_2, although the curve gradually shifted lower than that in the N_2. It was found that the addition of NH_3 to the N_2 gas had no effect on HE under the testing conditions of p_T = 0.1 MPa and $V = 2.0 \times 10^{-3}$ mm/s.

Figure 3.2 shows the J-Δa curves under the testing conditions of p_T = 0.1 MPa and $V = 2.0 \times 10^{-5}$ mm/s. The J-Δa curve in the H_2 gas with $V = 2.0 \times 10^{-5}$ mm/s was located at an even lower level than that in the H_2 with $V = 2.0 \times 10^{-3}$ mm/s. As a result, the reduction in J_{IC} became more significant by the decreased loading rate. These trends are consistent with past studies [3 - 11 - 3 - 13]. The J-Δa curve in the 1,000 ppm NH_3 and N_2 mixture is located higher than H_2 and significantly lower than that in the N_2. As described later, this significant reduction in the J_{IC} in the NH_3 added N_2 gas was due to HE. That is, the HE induction effect by NH_3 was significantly enhanced by decreased loading rate.

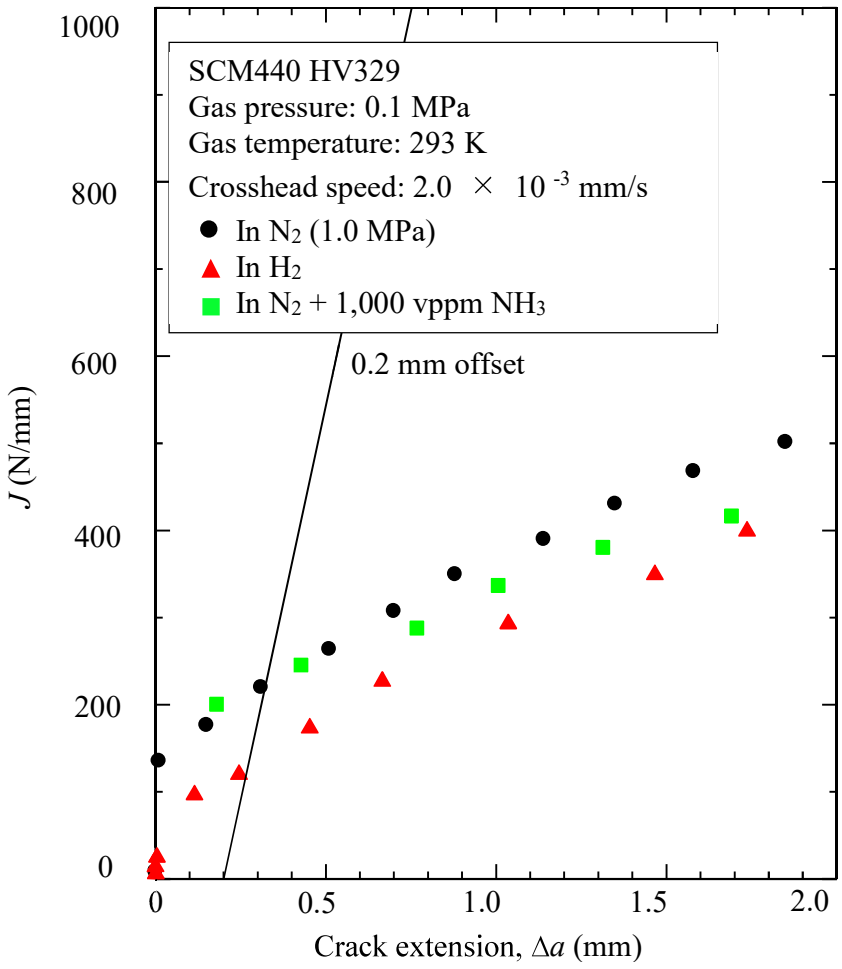

Fig. 3.1 Effect of NH_3 addition to N_2 environment on J-Δa curve at p_T = 0.1 MPa and $V = 2.0 \times 10^{-3}$ mm/s.

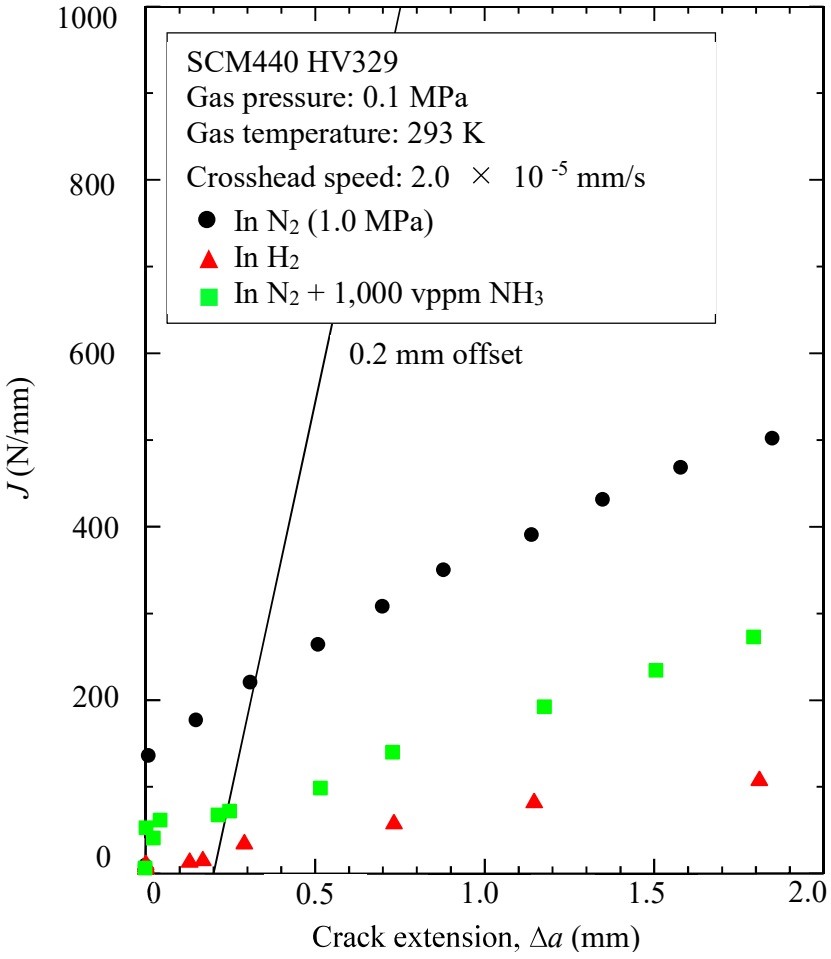

Fig. 3.2 Effect of NH_3 addition to N_2 environment on J-Δa curve at p_T = 0.1 MPa and $V = 2.0 \times 10^{-5}$ mm/s.

Table 3.1. J_{IC} value in each condition. [---]: Relative value to J_{IC} in N_2

Environment	N_2	H_2	N_2 + 1,000 ppmNH_3
p_T = 0.1 MPa, $V = 2.0 \times 10^{-3}$ mm/s	217 (1.0 MPa) [1]	128 [0.59]	211 [0.97]
p_T = 0.1 MPa, $V = 2.0 \times 10^{-5}$ mm/s		28 [0.13]	67 [0.31]

p_T : Total environmental gas pressure

V : Cross head displacement rate

3.3.2 Fracture surface

Figure 3.3 shows the fracture surfaces created during the fracture toughness test. The photographs show the fracture surfaces at the middle of the specimen thickness and at the crack length corresponding to J_{IC}. Dimple fracture was observed in the N_2 as shown in Fig. 2.5 (a) and quasi-cleavage (QC) fracture was observed in the H_2 as shown in Fig. 2.5 (b). Similar results were observed in the same kind of low alloy steel having a comparable material strength [3 - 14, 3 - 15]. In the case when NH_3 was not induced HE, e.g., during the fracture toughness test in the 1,000 vppm NH_3 added H_2 gas at p_T = 0.1 MPa with $V = 2 \times 10^{-3}$ mm/s, a dimple fracture surface was observed as shown in Fig. 3.3 (a). The morphology of the dimple was very similar to that in the N_2 gas. That is, there was no effect of the NH_3 addition to N_2. On the other hand, the fracture surface in the NH_3 added N_2 gas with the decreased loading rate $V = 2 \times 10^{-5}$ mm/s were QC and dimple (Fig. 3.3 (b)). This transition of the fracture surface morphology in the NH_3 added N_2 due to the decrease in loading rate, suggesting that NH_3 provided hydrogen entry followed by the decomposition reaction of NH_3 on the Fe surface.

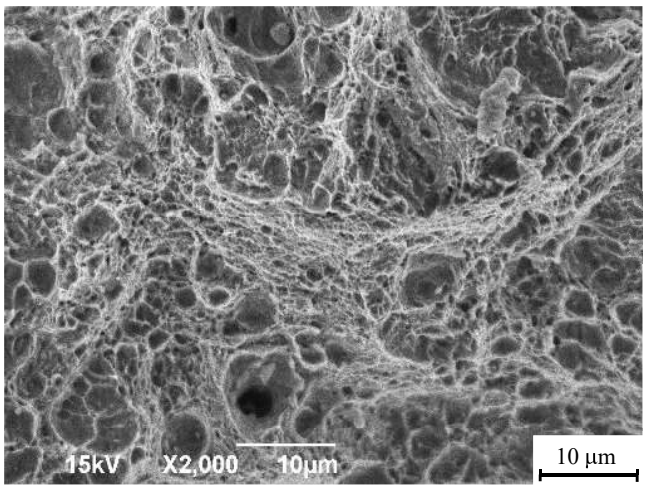

(a) In 1,000 vppm $NH_3 + N_2$, $p_T = 0.1$ MPa, $V = 2.0 \times 10^{-3}$ mm/s, $J_{IC} = 211$ N/mm

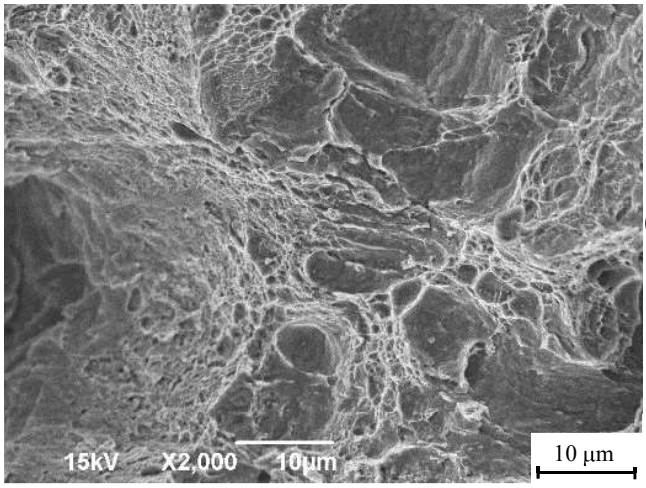

(b) In N_2 + 1,000 ppm NH_3, $p_T = 0.1$ MPa, $V = 2.0 \times 10^{-5}$ mm/s, $J_{IC} = 67$ N/mm

Fig. 3.3 Fracture surfaces

3.4 Discussion of mechanism of ammonia induction effect on hydrogen embrittlement on Fe (110) surface by density functional theory

The J_{IC} value in the 0.1 MPa NH_3 added N_2 gas agreed with that in the N_2 gas when $V = 2.0 \times 10^{-3}$ mm/s, however, the J_{IC} value was significantly reduced when $V = 2.0 \times 10^{-5}$mm/s. Although this environment initially did not contain hydrogen, this reduction is considered to be HE based on the examination of the fracture surface. It is presumed that hydrogen came from the decomposition of NH_3 on the Fe (110) surface, a body-centered cubic lattice, by the catalytic action of the Fe (110) surface [3 - 16 - 3 - 18].

The J_{IC} value in the 1,000 ppm NH_3 and N_2 mixture at $V = 2.0 \times 10^{-3}$ mm/s (J_{IC} = 211 N/mm) was significantly decreased when $V = 2.0 \times 10^{-5}$ mm/s (J_{IC} = 67 N/mm) at 0.1 MPa. One of the reasons why there was no reduction in the J_{IC} in the NH_3 and N_2 mixture when the loading rate was higher was the small amount of hydrogen produced by NH_3 due to the test duration was not enough for NH_3 further decomposition ($NH_3 \rightarrow H + NH_2$ may occur but $NH_2 \rightarrow H + NH$ and $NH \rightarrow H + N$ not occur). The rate of NH_3 decomposition is slow [3 - 19], which will be calculated by DFT. Thus, the amount of NH_3-derived hydrogen was small. Therefore, in the fracture toughness test with $V = 2.0 \times 10^{-3}$ mm/s, no HE occurred. On the other hand, the decrease in the loading rate to $V = 2.0 \times 10^{-5}$ mm/s provided sufficient times for the 1,000 ppm NH_3 decomposition ($NH_2 \rightarrow H + NH$ and $NH \rightarrow H + N$ may occur) and for hydrogen diffusion to the crack tip to cause the HE. Hence, the J_{IC} in the NH_3 and N_2 mixture was significantly reduced with the loading rate decreasing. Therefore, calculations for the reaction rate coefficient of NH_3, NH_2, and NH are necessary to investigate the decomposition reaction rate, which is significantly important to investigate the HE induction effect by NH_3 that has the lading rate dependence. On the other hand, it is also important to calculate the NH_3-derived hydrogen atom coverage on the Fe (110) surface to understand the mechanism of NH_3 inducing HE.

The NH_3 decomposition process is investigated with DFT. I considered the processing of NH_3 decomposition on the Fe (110) surface into four steps (I, II, III, IV) as shown below:

$$NH_3 + * \rightarrow NH_3* \quad \text{I}$$

$$NH_3* + * \rightarrow NH_2* + H* \quad \text{II}$$

$$NH_2* + * \rightarrow NH* + H* \quad \text{III}$$

$$NH* + * \rightarrow N* + H* \quad \text{IV}$$

Where NH_3 is the free gaseous status, * denote the vacant site on Fe (110) surface, NH_3*, NH_2*, NH*, N*, and H* denote the adsorbed species on Fe (110) surface.

3.4.1 Ammonia decomposition with Fe (110) surface catalysis

Based on the result of the investigation for the NH_3 adsorption site in chapter 2, the NH_3 molecule was adsorbed on the top site of the Fe (110) surface. In this section, I investigate the occupied site on Fe (110) surface and the activation energy (E_a) for NH_3 decomposition in each step (II, III, IV). For the first step (II), the adsorbed NH_3 decomposes one hydrogen atom on the Fe (110) surface. To investigate the occupied site for NH_3-derived hydrogen atom, I put the hydrogen atom to the top site, bridge site, and the hollow site to calculate the E_a, respectively. The initial geometry, transition geometry, and end geometry is shown in Figs. 3.4 - 3.6.

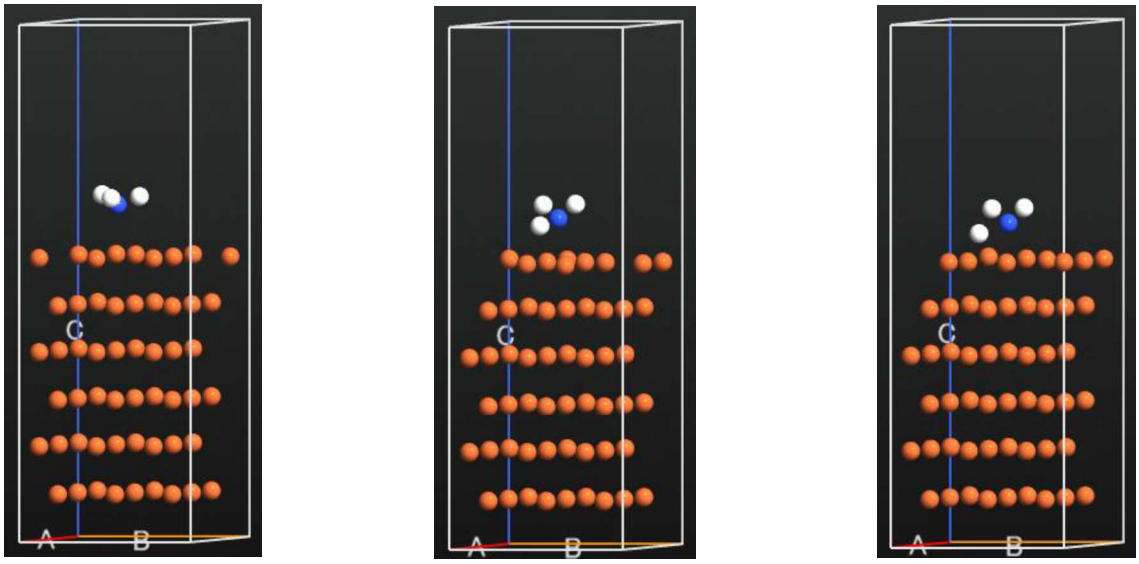

(a) Initial (b) Transition (c) End

Fig. 3.4 NH_3-derived hydrogen atom on Top site. (a) Initial, (b) Transition, (c) End.

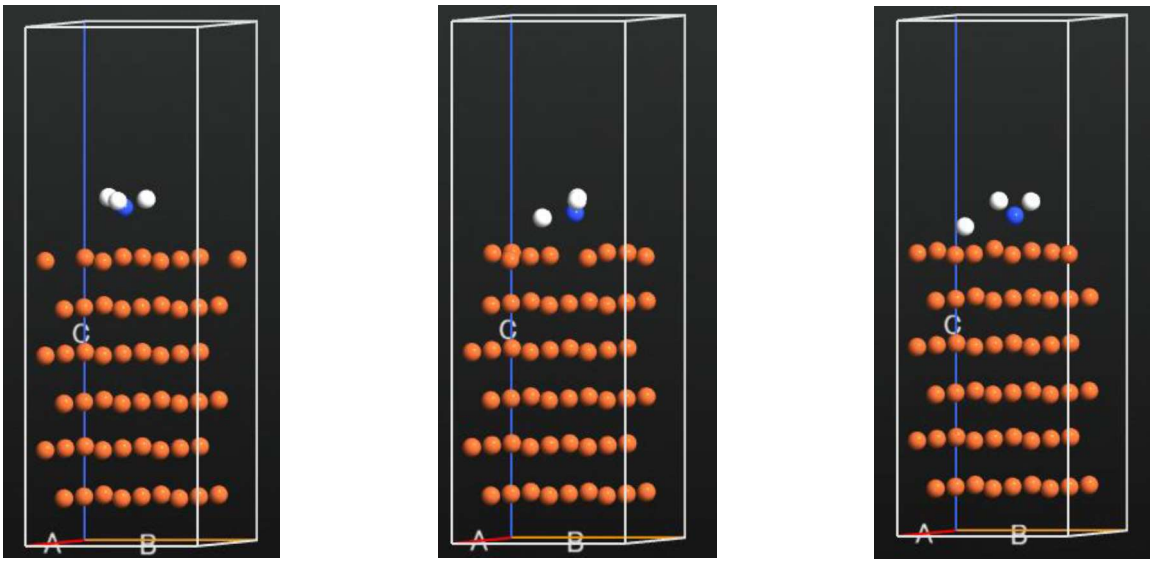

(a) Initial (b) Transition (c) End

Fig. 3.5 NH_3-derived hydrogen atom on Bridge site. (a) Initial, (b) Transition, (c) End.

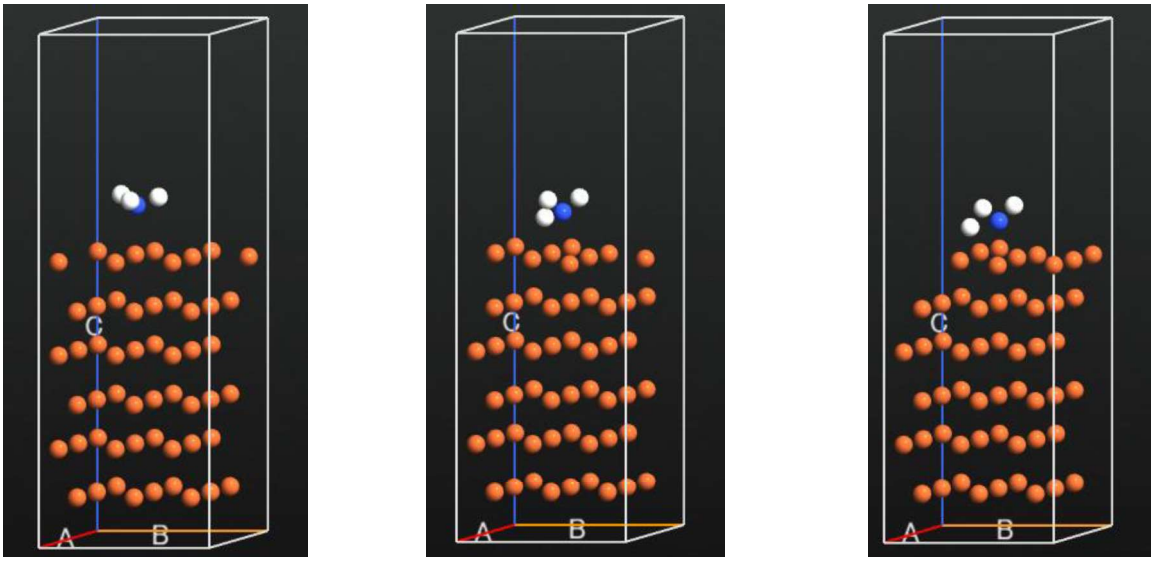

(a) Initial (b) Transition (c) End

Fig. 3.6 NH_3-derived hydrogen atom on Hollow site. (a) Initial, (b) Transition, (c) End.

The E_a for NH_3 decomposes hydrogen atom on the top site, bridge site, and hollow site is 0.94 eV, 0.71 eV, and 0.94 eV, respectively. The site which has the minimum E_a is the site the hydrogen atom prefers. Because it required the lowest energy barrier to overcome for reaction. Therefore, for NH_3 decomposing to NH_2 and H atom, the H atom occupied the bridge site, and the NH_2 occupied the bridge as well. The different occupied site represents different Fe atoms number for interacting with adsorbed species. The top site indicates adsorbed species interact with one Fe atom. The bridge site indicates adsorbed species interact with two Fe atoms. The hollow site indicates that adsorbed species interact with three Fe atoms.

Then I used the same method to investigate the NH, N, and H atoms occupied the site on Fe (110) surface respectively. The geometry of the minimum E_a site as shown in Figs. 3.7 and 3.8. The decomposition occupied the site of species and the E_a as shown in Table 3.2. In chemical kinetics, the overall rate of a reaction is approximately determined by the slowest step, and the step is named the rate-limiting step. Based on Table 3.2, the rate-limiting step of NH_3 decomposition is the last step (NH→N+H), which agrees with the previous report in the literature [3 - 21].

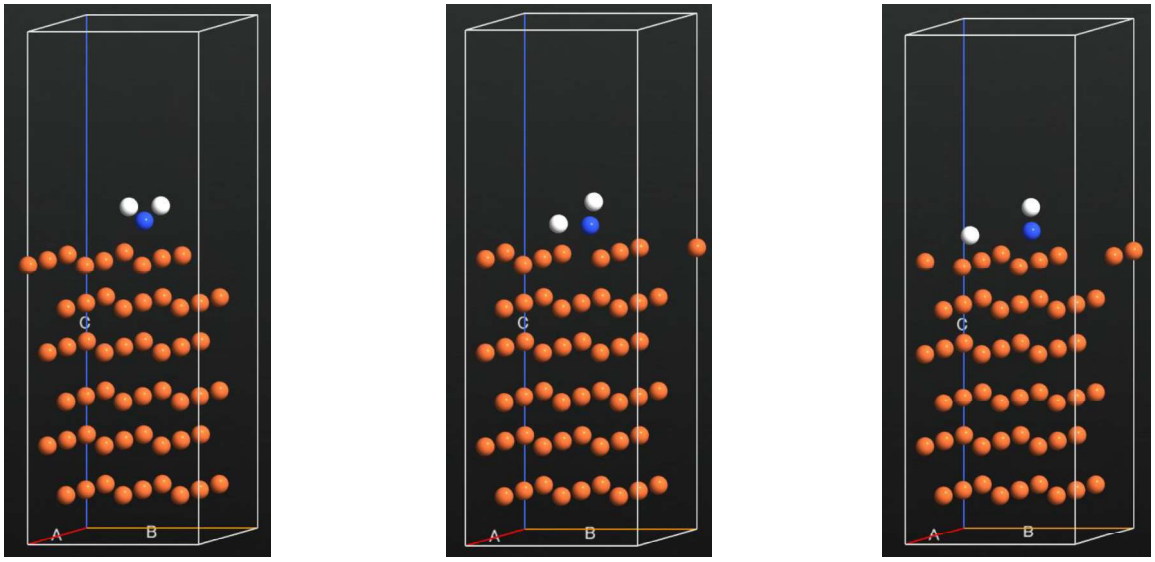

(a) Initial (b) Transition (c) End

Fig. 3.7 NH_2-derived hydrogen atom on bridge site. (a) Initial, (b) Transition, (c) End.

.

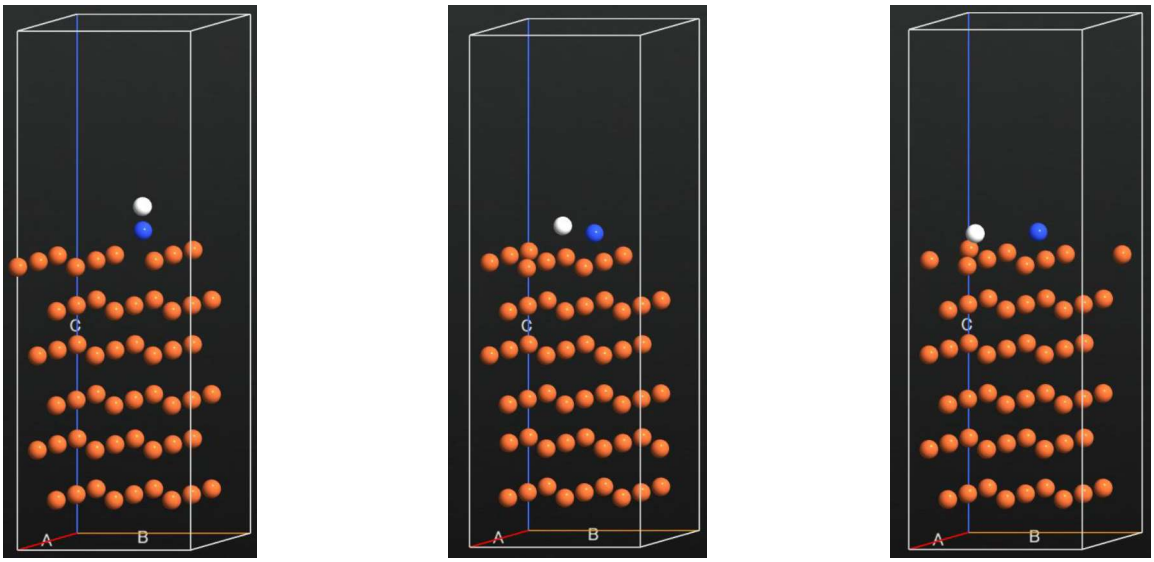

(a) Initial (b) Transition (c) End

Fig. 3.8 NH-derived hydrogen atom on bridge site. (a) Initial, (b) Transition, (c) End.

Table 3.2 Decomposition and desorption E_a of NH_3

	Decomposition activation barrier	Desorption activation barrier
$NH_3 \rightarrow NH_2 + H$	0.72 eV (Exo)	1.43 eV (Endo)
$NH_2 \rightarrow NH + H$	0.45 eV (Exo)	1.36 eV (Endo)
$NH \rightarrow N + H$	0.99 eV (Exo)	1.18 eV (Endo)

Exo = Exothermic reaction

Endo = Endothermic reaction

Table 3.3 Occupied site of different adsorbed species on Fe (110) surface

Adsorbed species	Occupied site
NH_3	Top
NH_2	Bridge
H atom derived by NH_3	Bridge
NH	Hollow
H atom derived by NH_2	Bridge
N	Hollow
H atom derived by NH	Bridge

3.4.2 Reaction rate coefficient of ammonia decomposition in each step

In eq 1.4, the A is taken from Table 3.4, the E_a is taken from Table 3.2, R is the universal gas constant, and T is 293K for fitting with the fracture toughness test condition. Using eq 1.4, the reaction rate coefficient of NH_3 decomposition in each step can be calculated as shown in Table 3.5. The reaction rate coefficient of NH_3, NH_2, and NH is decreasing, which indicates that the reaction rate of NH_3 decomposition is decreasing and decreasing. There is a great reduction in the reaction rate coefficient from NH_2 to NH, which demonstrates that the last step of NH_3 decomposition ($NH \rightarrow N + H$) is the slowest step, which is difficult to occur during the fracture toughness test. However, the first two decomposition steps ($NH_3 \rightarrow NH_2 + H$; $NH_2 \rightarrow NH + H$) are possible to occur during the test.

Table. 3.4 Pre-exponential factors (frequency factor) of nitrogen hydrides

	NH_3	NH_2	NH
A (Hz)	3.18×10^{20}	2.14×10^{13}	1.35×10^{16}

Table. 3.5 Reaction rate coefficient k of NH_3 decomposition

	NH_3	NH_2	NH
k (s^{-1})	1.36×10^{8}	7.28×10^{5}	2.13×10^{-1}

3.4.3 Equation establish of calculation NH_3-derived hydrogen atom coverage on Fe (110) surface: kinetic modeling of ammonia decomposition

The acknowledged decomposition mechanism of NH_3 includes the chemisorption of NH_3 on the catalyst surface [3 - 26 - 3 - 30]. Continuous dehydrogenation of NH_3 and nitrogen and hydrogen binding desorption. The adsorption of all the species follows the Langmuir isotherm model, therefore it is assumed that the surface sites are energetically equivalent and each site can hold at most one adsorbed species molecule. The mechanism can be described according to the following sequence of elementary reactions:

(I) $NH_3 + * \overset{\overrightarrow{k_1},\ \overleftarrow{k_1}}{\longleftrightarrow} NH_3*$

(II) $NH_3* + * \overset{\overrightarrow{k_2},\ \overleftarrow{k_2}}{\longleftrightarrow} NH_2* + H*$

(III) $NH_2* + * \overset{\overrightarrow{k_3},\ \overleftarrow{k_3}}{\longleftrightarrow} NH* + H*$

(IV) $NH* + * \overset{\overrightarrow{k_4},\ \overleftarrow{k_4}}{\longleftrightarrow} N* + H*$

The term * denotes a vacant site, and NH_3*, NH_2*, NH*, N*, and H* are the adsorbed species. If all the above reactions are equilibrium that the constants of equilibrium can be expressed in terms of concentration of adsorbed species as:

$$K_1 = \frac{\overrightarrow{k_1}}{\overleftarrow{k_1}} = \frac{[\mathrm{NH3*}]}{\rho_{NH3}[*]} \tag{3.1}$$

Where the $\overrightarrow{k_1}$ and $\overleftarrow{k_1}$ represent the rate constant coefficient of the reaction I of forward reaction and backward reaction, respectively. K_1 is the equilibrium constant of reaction I.

$$K_2 = \frac{\overrightarrow{k_2}}{\overleftarrow{k_2}} = \frac{[\mathrm{NH2*}][\mathrm{H*}]}{[\mathrm{NH3*}][*]} \tag{3.2}$$

Where the $\overrightarrow{k_2}$ and $\overleftarrow{k_2}$ represent the rate constant coefficient of the reaction II of forward reaction and backward reaction, respectively. K_2 is the equilibrium constant of reaction II.

$$K_3 = \frac{\overrightarrow{k_3}}{\overleftarrow{k_3}} = \frac{[\mathrm{NH*}][\mathrm{H*}]}{[\mathrm{NH2*}][*]} \tag{3.3}$$

Where the $\overrightarrow{k_3}$ and $\overleftarrow{k_3}$ represent the rate constant coefficient of the reaction III of forward reaction and backward reaction, respectively. K_3 is the equilibrium constant of reaction Ⅲ.

$$K_4 = \frac{\overrightarrow{k_4}}{\overleftarrow{k_4}} = \frac{[\mathrm{N*}][\mathrm{H*}]}{[\mathrm{NH*}][*]} \tag{3.4}$$

Where the $\overrightarrow{k_4}$ and $\overleftarrow{k_4}$ represent the rate constant coefficient of the reaction IV of forward reaction and backward reaction, respectively. K_4 is the equilibrium constant of reaction Ⅳ.

The reaction rate coefficient *k* ($\overrightarrow{k_1}$, $\overleftarrow{k_1}$, $\overrightarrow{k_2}$, $\overleftarrow{k_2}$, $\overrightarrow{k_3}$, $\overleftarrow{k_3}$, $\overrightarrow{k_4}$, $\overleftarrow{k_4}$) in each step is given by Arrhenius equation (eq 1.4). There is one thing that needs to be noted is that the model of coverage calculation elides the computation of the preexponential factor *A* (eq 1.5), while it will be calculated in the next section for calculating the reaction rate coefficient. Such an approximation is only partially justified in coverage calculation because the preexponential factors for adsorption and desorption (opposite reaction) processes would cancel.

The use of NH_3 as indirect hydrogen storage material is obviously entirely dependent on the process of efficiently converting NH_3 to hydrogen. In order to calculate the NH_3-derived hydrogen atom coverage on the Fe (110) surface. Establishing the equation is significantly important for it. Due to the fracture toughness test duration is limited, and we can't identify which step of NH_3 decomposition is able to occur during the test. Therefore, I investigate the hydrogen atom coverage on Fe (110) surface step by step and assumed I can reach each step and have equilibrium at this moment. The reaction rate coefficient of each step will be investigated in the next section.

Case A: The reaction of NH_3 decomposition reaches the state which has the NH_2 and H atom as products and has equilibrium was considered (reaction I, II). Therefore, the equilibrium equations will be given by the following eqs 3.5 and 3.6.

(I) $NH_3 + * \rightarrow NH_3*$

(II) $NH_3* + * \rightarrow NH_2* + H*$

$$\overrightarrow{k_1}\rho_{NH_3}\theta_v = \overleftarrow{k_1}\theta_{NH_3*} \tag{3.5}$$

$$\overrightarrow{k_2}\theta_{NH_3*}\theta_v = \overleftarrow{k_2}\theta_{NH_2*}\theta_{H*(NH_3)} \tag{3.6}$$

Where θ_{NH_3*}, θ_{NH_2*}, $\theta_{H*(NH_3)}$ denotes fractional coverage of NH_2, NH_2, and NH adsorbed species on the Fe (110) surface respectively. θ_{NH_2*} equal to $\theta_{H*(NH_3)}$ as equilibrium. ρ_{NH_3} is denote the partial pressure of NH_3. $\overrightarrow{k_1}$ and $\overleftarrow{k_1}$ are the reaction rate coefficient for decomposition and desorption, which is given by the Arrhenius equation (eq 1.4). The temperature is 293K to fit my test condition.

Based on the assumption that reactions I and II are achieved equilibrium, the adsorbed species on the Fe (110) surface in Case A are NH_3*, NH_2*, and $H*$ atom, and the remaining sites are vacant. Therefore, the entire surface can be considered into four parts, θ_{NH_3*} represents the fractional coverage of NH_3, θ_{NH2*} represents the fractional coverage of NH_2, $\theta_{H*(NH_3)}$ represents the fractional coverage of hydrogen atom, θ_v represents the fractional coverage of the vacant site. Thus, the entire surface will be given by the following equation 3.8.

$$\theta_{NH_3*} + \theta_v + \theta_{NH_2*} + \theta_{H*(NH_3)} = 1 \tag{3.7}$$

From eqs 3.5 - 3.7, the fractional coverage of all adsorbed species can be calculated as equations as follows:

$$\theta_v = \frac{1}{K_1\rho_{NH_3}+2\sqrt{K_1K_2\rho_{NH_3}}+1} \tag{3.8}$$

$$\theta_{NH_3*} = \frac{K_1\rho_{NH_3}}{K_1\rho_{NH_3}+2\sqrt{K_1K_2\rho_{NH_3}}+1} \tag{3.9}$$

$$\theta_{NH_2*} = \theta_{H*(NH_3)} = \frac{\sqrt{K_1K_2\rho_{NH_3}}}{K_1\rho_{NH_3}+2\sqrt{K_1K_2\rho_{NH_3}}+1} \tag{3.10}$$

Based on equations 3.8 - 3.10, the coverage of adsorbed species on the Fe (110) surface in Case A can be calculated. The coverage of adsorbed species in Case A is shown in Table 3.6.

Table 3.6 Adsorbed species coverage on Fe (110) in Case A

	Coverage
θ_{NH_3*}	9.51%
θ_{NH_2*}	0.79%
$\theta_{H*(NH_3)}$	0.79%

Case B: The reaction of NH_3 decomposition reaches the state which has the NH and H atom as products and has equilibrium was considered (reaction I, II, III). Therefore, the equilibrium equations will be given by the following eqs 3.11 - 3.13.

(I) $NH_3 + * \rightarrow NH_3*$

(II) $NH_3* + * \rightarrow NH_2* + H*$

(III) $NH_2* + * \rightarrow NH* + H*$

$$\overrightarrow{k_1}\rho_{NH_3}\theta_v = \overleftarrow{k_1}\theta_{NH_3*} \tag{3.11}$$

$$\overrightarrow{k_2}\theta_{NH_3*}\theta_v = \overleftarrow{k_2}\theta_{NH_2*}\theta_{H*(NH_3)} \tag{3.12}$$

$$\overrightarrow{k_3}\theta_{NH_2*}\theta_v = \overleftarrow{k_3}\theta_{NH*}\theta_{H*(NH_2)} \tag{3.13}$$

Where θ_{NH_3*}, θ_{NH_2*}, θ_{NH*}, $\theta_{H*(NH_3)}$, $\theta_{H*(NH_2)}$ denotes fractional coverage of NH_3, NH_2, NH, hydrogen atom (from NH_3 and NH_2 decomposition) adsorbed species on the Fe (110)

surface respectively. θ_{NH_2*} equal to $\theta_{H*(NH_3)}$ as equilibrium. θ_{NH*} equal to $\theta_{H*(NH_2)}$ as equilibrium. ρ_{NH_3} is denote the partial pressure of NH_3. $\overrightarrow{k_1}$, $\overleftarrow{k_1}$, $\overrightarrow{k_2}$, $\overleftarrow{k_2}$ $\overrightarrow{k_3}$ and $\overleftarrow{k_3}$ are the reaction rate coefficient for decomposition and desorption, which is given by Arrhenius equation (eq 1.4). The temperature is 293K to fit my test condition.

Based on the assumption that reactions I, II, and III are achieved the equilibrium, the adsorbed species on the Fe (110) surface in Case B are NH_3*, NH_2*, $NH*$, and $H*$ atom, the remaining sites are vacant. We have to note that the Hydrogen atom source in Case B, which is come from two sources (NH_3 and NH_2). Therefore, the entire surface can be considered into six parts, θ_{NH_3*} represents the fractional coverage of NH_3, θ_{NH_2*} represents the fractional coverage of NH_2, θ_{NH*} represents the fractional coverage of NH, $\theta_{H*(NH_3)}$ represents the fractional coverage of hydrogen atom, θ_v represents the fractional coverage of the vacant site. Therefore, the entire surface will be given by the following equation 3.14.

$$\theta_{NH_3*} + \theta_v + \theta_{NH_2*} + \theta_{H*(NH_3)} + \theta_{NH*} + \theta_{H*(NH_2)} = 1 \tag{3.14}$$

From eqs 3.11-3.14, the fractional coverage of all adsorbed species can be calculated as equations as follows:

$$\theta_v = \frac{1}{K_1\rho_{NH_3}+2\sqrt{K_1K_2\rho_{NH_3}}+2\sqrt{K_3\sqrt{K_1K_2\rho_{NH_3}}}+1} \tag{3.15}$$

$$\theta_{NH_3*} = \frac{K_1\rho_{NH_3}}{K_1\rho_{NH_3}+2\sqrt{K_1K_2\rho_{NH_3}}+2\sqrt{K_3\sqrt{K_1K_2\rho_{NH_3}}}+1} \tag{3.16}$$

$$\theta_{NH_2*} = \frac{\sqrt{K_1K_2\rho_{NH_3}}}{K_1\rho_{NH_3}+2\sqrt{K_1K_2\rho_{NH_3}}+2\sqrt{K_3\sqrt{K_1K_2\rho_{NH_3}}}+1} \tag{3.17}$$

$$\theta_{NH*} = \frac{\sqrt{K_3\sqrt{K_1K_2\rho_{NH_3}}}}{K_1\rho_{NH_3}+2\sqrt{K_1K_2\rho_{NH_3}}+2\sqrt{K_3\sqrt{K_1K_2\rho_{NH_3}}}+1} \tag{3.18}$$

$$\theta_{H*} = \theta_{H*(NH_3)} + \theta_{H*(NH_2)}$$

$$= \frac{\sqrt{K_1K_2\rho_{NH_3}} + \sqrt{K_3\sqrt{K_1K_2\rho_{NH_3}}}}{K_1\rho_{NH_3} + 2\sqrt{K_1K_2\rho_{NH_3}} + 2\sqrt{K_3\sqrt{K_1K_2\rho_{NH_3}}} + 1} \quad (3.19)$$

Based on eqs 3.15-3.19, the coverage of adsorbed species on the Fe (110) surface in Case B can be calculated. The coverage of adsorbed species in Case B is shown in Table 3.7.

Table 3.7 Adsorbed species coverage on Fe (110) in Case B

θ_{NH_3*}	3.00%
θ_{NH_2*}	0.25%
θ_{NH*}	3.80%
$\theta_{H*(NH_3+NH_2)}$	4.06%

Case C: The reaction of NH_3 decomposition reaches the state which has the N and H atom as products and has equilibrium was considered (reaction I, II, III, IV). So, the equilibrium equations will be given by the following eqs 3.20 - 3.23.

(I) $NH_3 + * \rightarrow NH_3*$

(II) $NH_3* + * \rightarrow NH_2* + H*$

(III) $NH_2* + * \rightarrow NH* + H*$

(IV) $NH* + * \rightarrow N* + H*$

$$\overrightarrow{k_1}\rho_{NH_3}\theta_v = \overleftarrow{k_1}\theta_{NH_3*} \quad (3.20)$$

$$\overrightarrow{k_2}\theta_{NH_3*}\theta_v = \overleftarrow{k_2}\theta_{NH_2*}\theta_{H*(NH_3)} \quad (3.21)$$

$$\overrightarrow{k_3}\theta_{NH_2*}\theta_v = \overleftarrow{k_3}\theta_{NH*}\theta_{H*(NH_2)} \quad (3.22)$$

$$\overrightarrow{k_4}\theta_{NH*}\theta_v = \overleftarrow{k_4}\theta_{N*}\theta_{H*(NH)} \quad (3.23)$$

Where θ_{NH_3*}, θ_{NH_2*}, θ_{NH*}, θ_{N*}, $\theta_{H*(NH_3)}$, $\theta_{H*(NH_2)}$, $\theta_{H*(NH)}$ denotes fractional coverage of NH_3, NH_2, NH, nitrogen and hydrogen atom (from NH_3 and NH_2 decomposition) adsorbed species on the Fe (110) surface respectively. θ_{NH_2*} equal to $\theta_{H*(NH_3)}$ as equilibrium. θ_{NH*} equal to $\theta_{H*(NH_2)}$ as equilibrium. θ_{N*} equal to $\theta_{H*(NH)}$ as equilibrium. ρ_{NH3} is denote the partial pressure of NH_3. $\overrightarrow{k_1}$, $\overleftarrow{k_1}$, $\overrightarrow{k_2}$, $\overleftarrow{k_2}$, $\overrightarrow{k_3}$, $\overleftarrow{k_3}$, $\overrightarrow{k_4}$ and $\overleftarrow{k_4}$ are the reaction rate coefficient for decomposition and desorption, which is given by Arrhenius equation (eq 1.4). The temperature is 293K to fit my test condition.

Based on the assumption that reactions I, II, III, and IV are achieved equilibrium, the adsorbed species on the Fe (110) surface in Case C are NH_3✻, NH_2✻, NH✻, N✻, and H✻ atom, the remaining sites are vacant. We have to note that the hydrogen atom source in Case C, which is come from three sources (NH_3, NH_2, and NH). Therefore, the entire surface can be considered into eight parts, θ_{NH_3*} represents the fractional coverage of NH_3, θ_{NH_2*} represents the fractional coverage of NH_2, θ_{NH*} represents the fractional coverage of NH, θ_{N*} represents the fractional coverage of nitrogen atom, θ_{H*} represents the fractional coverage of hydrogen atom, θ_v represents the fractional coverage of the vacant site. Therefore, the entire surface will be given by the following equation 3.24.

$$\theta_{NH_3*} + \theta_v + \theta_{NH_2*} + \theta_{H*(NH_3)} + \theta_{NH*} + \theta_{H*(NH_2)} + \theta_{N*} + \theta_{H*(NH)} = 1 \quad (3.24)$$

From eqs 3.20 - 3.24, the fractional coverage of all adsorbed species can be calculated as equations as follows:

$$\theta_v = \frac{1}{K_1\rho_{NH_3}+2\sqrt{K_1K_2\rho_{NH_3}}+2\sqrt{K_3\sqrt{K_1K_2\rho_{NH_3}}}+2\sqrt{K_4\sqrt{K_3\sqrt{K_1K_2\rho_{NH_3}}}}+1} \quad (3.25)$$

$$\theta_{NH_3*} = \frac{K_1\rho_{NH_3}}{K_1\rho_{NH_3}+2\sqrt{K_1K_2\rho_{NH_3}}+2\sqrt{K_3\sqrt{K_1K_2\rho_{NH_3}}}+2\sqrt{K_4\sqrt{K_3\sqrt{K_1K_2\rho_{NH_3}}}}+1} \quad (3.26)$$

$$\theta_{NH_2*} = \frac{\sqrt{K_1K_2\rho_{NH_3}}}{K_1\rho_{NH_3}+2\sqrt{K_1K_2\rho_{NH_3}}+2\sqrt{K_3\sqrt{K_1K_2\rho_{NH_3}}}+2\sqrt{K_4\sqrt{K_3\sqrt{K_1K_2\rho_{NH_3}}}}+1} \quad (3.27)$$

$$\theta_{NH*} = \frac{\sqrt{K_3\sqrt{K_1K_2\rho_{NH_3}}}}{K_1\rho_{NH_3}+2\sqrt{K_1K_2\rho_{NH_3}}+2\sqrt{K_3\sqrt{K_1K_2\rho_{NH_3}}}+2\sqrt{K_4\sqrt{K_3\sqrt{K_1K_2\rho_{NH_3}}}}+1} \quad (3.28)$$

$$\theta_{NH*} = \frac{\sqrt{K_4\sqrt{K_3\sqrt{K_1K_2\rho_{NH3}}}}}{K_1\rho_{NH3}+2\sqrt{K_1K_2\rho_{NH3}}+2\sqrt{K_3\sqrt{K_1K_2\rho_{NH3}}}+2\sqrt{K_4\sqrt{K_3\sqrt{K_1K_2\rho_{NH3}}}}+1} \quad (3.29)$$

$$\theta_{H*} = \theta_{H*(NH_3)} + \theta_{H*(NH_2)} + \theta_{H*(NH)} =$$

$$\frac{\sqrt{K_1K_2\rho_{NH_3}}+\sqrt{K_3\sqrt{K_1K_2\rho_{NH_3}}}+\sqrt{K_4\sqrt{K_3\sqrt{K_1K_2\rho_{NH_3}}}}}{K_1\rho_{NH_3}+2\sqrt{K_1K_2\rho_{NH_3}}+2\sqrt{K_3\sqrt{K_1K_2\rho_{NH_3}}}+2\sqrt{K_4\sqrt{K_3\sqrt{K_1K_2\rho_{NH_3}}}}+1} \quad (3.30)$$

Based on equations 3.25 - 3.30, the coverage of adsorbed species on the Fe (110) surface in Case C can be calculated. The coverage of adsorbed species in Case C is shown in Table 3.8.

Table 3.8 Adsorbed species coverage on Fe (110) in Case C

	Coverage
θ_{NH_3*}	3.00%
θ_{NH_2*}	0.25%
θ_{NH*}	3.80%
θ_{N*}	9.70×10^{-6}%
$\theta_{H*(NH_3+NH_2+NH)}$	4.06%

From Case A to Case B, following the process of NH_3 decomposition, the hydrogen atom coverage on Fe (110) significantly increased from 0.79% to 4.06%. According to Table 3.2 the activation energy barrier of the reaction II is higher than III, which indicates that once the reaction II occurred, the reaction III can occur. On the other hand, from Case B to Case C, the hydrogen atom coverage on Fe (110) surface is almost not increased and considering the reaction rate coefficient significantly decreased from Case B to Case C, which is indicated that the last step of NH_3 is very hard to occur under the test condition. Meanwhile, the last step of NH_3 decomposition is the rate-limiting step as shown in Table 3.2.

Though there is no investigation related to hydrogen atom coverage on Fe (110) surface to HE occurred or not. The past study of CO mitigation effect on HE released that with decreased the loading rate from 2.0×10^{-3} to 2.0×10^{-5} mm/s in fracture toughness test, even 0.60% hydrogen atom coverage is able to lead to HE [3 - 31]. Since the NH_3 decomposition derived hydrogen coverage in each case is greater than 0.60%, NH_3 can induce HE by its decomposition at the 2.0×10^{-5} mm/s loading rate.

3.5 Conclusion

Fracture toughness tests of low-alloy steel SCM440 were conducted in an NH_3 added N_2 gas environment in order to characterize the effect of the NH_3 on the HE. To understand the mechanism of the HE induction effect by NH_3, the DFT calculations were also conducted. The main results achieved in this chapter are as follows:

1. NH_3 induced the HE by its decomposition.

2. The rate-limiting step of NH_3 decomposition is the reaction IV, NH→N+H, which has almost no contribution to hydrogen coverage on Fe (110) surface.

3. Compared with the NH_3 adsorption rate ($k = 3.14\times10^{20}$ s^{-1}), the NH_3 decomposition rate ($k = 1.36\times10^{8}$ s^{-1}) was very slow. Therefore, NH_3 had no effect on HE at a relatively high loading rate (2.0×10^{-3} mm/s), however, NH_3 significantly decreased fracture toughness from 211 N/mm to 67 N/mm and induced HE at a relatively low loading rate (2.0×10^{-5} mm/s).

4. With 1 NH_3 adsorbed on 9 Fe (110) surface (11.11% NH_3 coverage), NH_3-derived hydrogen coverage on Fe (110) surface was 4.06% at a relatively slow loading rate (2.0×10^{-5}mm/s).

5. With 1 NH_3 adsorbed on 9 Fe (110) surface (11.11% NH_3 coverage), as NH_3 decomposition occurred, the NH_3-derived hydrogen coverage on Fe (110) was increased from 0.79% to 4.06%.

3.6 References

1. Yeo S. C., Han S. S., Lee H. M., Mechanistic Investigation of the catalytic decomposition of ammonia on an Fe (100) surface: A DFT Study, *Journal of Physical Chemistry C*, Vol. 118, **2014**, pp. 5309-5316.
   Christensen C. H., Johannessen T., Sørensen R. Z., et al, Towards an ammonia-mediated hydrogen economy, *Catalysis Today*, Vol. 111, **2006**, pp. 140-144.
2. Avci A. K., Trimm D. L., Onsan Z. I., Quantitative Investigation of Catalytic Natural Gas Conversion for Hydrogen Fuel Cell Applications, *Chemical Engineering Journal*, Vol. 90, **2002**, pp. 77-87.
3. Chein R. Y., Chen Y. C., Chang C. S., Chung J. N., Numerical Modeling of Hydrogen Production from Ammonia Decomposition for Fuel Cell Applications, *International Journal of Hydrogen Energy*, Vol. 35, **2010**, pp. 589-597.
4. Chellappa A. S., Fischer C. M., Thomson W. J., Ammonia Decomposition Kinetics over Ni-Pt/Al_2O_3 for Pem Fuel Cell Applications. *Applied Catalysis A*, Vol. 227, **2002**, pp. 231-240.
5. Arabczyk W., Zamlynny J., Study of the ammonia decomposition over iron catalysts, *Catalysis Letters*, Vol. 60, **1999**, pp. 167-171.
6. Mukherjee S., Devaguptapu S. V., Sviripa A., et al, Low-temperature ammonia decomposition catalysts for hydrogen generation, *Applied Catalysis B: Environmental*, Vol. 226, **2018**, pp. 162-181.
7. Bell T.E., Torrente M. L., H_2 Production via Ammonia Decomposition Using Non-Noble Metal Catalysts: A Review, *Topics in Catalysis*, Vol. 59, **2016**, pp. 438-1457.
8. Bozso F., Ertl G., Weiss M., Interaction of nitrogen with iron surfaces: II. Fe (110), *Journal of Catalysis*, Vol. 50, **1977**, pp. 519-529.
9. Ji J., Duan X., Gong X., et al, Promotional Effect of Carbon on Fe Catalysts for Ammonia Decomposition: A Density Functional Theory Study, *Industrial & Engineering Chemistry*, Vol. 52, **2013**, pp. 17151-17155.

10. Michler T., Naumann J., Microstructural aspects upon hydrogen environment embrittlement of various bcc steels, *International Journal of Hydrogen Energy*, Vol. 35, **2010**, pp. 821-832.
11. Stroh A. N., A theory of the fracture of metals. *Advances in Physics*, Vol. 6, **1957**, pp. 418-465.
12. Murakami Y., Matsuoka S., Effect of hydrogen on fatigue crack growth of metals. *Engineering Fracture Mechanics*, Vol. 77, **2010**, pp. 1926-1940.
13. Komoda R., Kubota M., Staykov A., et al, Effect of Gas Pressure on Hydrogen Environment Embrittlement of Carbon Steel A106 in Carbon Monoxide Mixed Hydrogen Gas, *Metallurgical and Materials Transactions A*, Vol. 53, **2022**, pp. 74-85.
14. Cho L., Bradley P.E., Lauria D.S., et al, Effects of hydrogen pressure and prior austenite grain size on the hydrogen embrittlement characteristics of a press-hardened martensitic steel, *International Journal of Hydrogen Energy*, Vol. 46, **2021**, pp. 24425-24439.
15. Lamb K. E., Dolan M. D., Kennedy D. F., Ammonia for hydrogen storage: A review of catalytic ammonia decomposition and hydrogen separation and purification, *International Journal of Hydrogen Energy*, Vol. 44, **2019**, pp. 3580-3593.
16. Itoh M., Masuda M., Machida K., Hydrogen Generation by Ammonia Cracking with Iron Metal-Rare Earth Oxide Composite Catalyst, *Materials Transactions*, Vol. 43, **2002**, pp. 2763-2767.
17. Benndorp C., Madey T. E., Johnson A. L., NH_3 adsorption and dissociation on a stepped Fe (100) surface, *Surface Science*, Vol. 187, **1987**, pp. 434-444.
18. Arabczyk W., Zamlynny J. Study of the ammonia decomposition over iron catalysts. *Catalysis Letters*, Vol. 60, **1999**, pp. 167-171.
19. James R., Chelikowsky and Steven G. Louie, First-principles linear combination of atomic orbitals method for the cohesive and structural properties of solids: Application to diamond, Physical Review B, Vol. 29, **1984**, pp. 6-15.

20. Lin R. J., Li F. Y., Chen H. L., Computational Investigation on Adsorption and Dissociation of the NH_3 Molecule on the Fe (111) Surface, *Journal of Physical Chemistry C*, Vol. 115, **2011**, pp. 521-528.
21. Arrhenius S., Quantitative relationship between the rate a reaction proceed and its temperature, *Journal of Physical Chemistry*, Vol. 4, **1889**, pp. 226-248.
22. Holmes F. L., From Elective Affinities to Chemical Equilibria: Berthollet's Law of Mass Action, *Historical Studies in the Physical Sciences*, Vol. 8, **1977**, pp. 105-145.
23. Lund E. W., Guldberg and Waage and the law of mass action, *Journal of Chemical Education*, **1965**, pp. 548-550.
24. Grote R. F., Hynes J. T., The stable states picture of chemical reactions. II. Rate constants for condensed and gas phase reaction models, *Journal of Physical Chemistry*, Vol. 73, **1980**, pp. 2715-2732.
25. Yin S.F., Xu B.Q., Zhou X.P., Au C.T., A mini-review on ammonia decomposition catalysts for on-site generation of hydrogen for fuel cell applications, *Applied Catalysis A: General*, Vol. 277, **2004**, pp. 1-9.
26. Tsai W., Weinberg W. H., Steady-State Decomposition of Ammonia on the Ru(001) Surface, *Journal of Physical Chem*istry, Vol. 91, **1987**, pp. 5302-5307.
27. Ertl G., Surface Science and Catalysis—Studies on the Mechanism of Ammonia Synthesis: The P. H. Emmett Award Address, *Catalysis Reviews*, Vol. 21, **1980**, pp. 201-223.
28. Kowalczyk Z., Sentek J., Jodzis S., Muhler M., Hinrichsen O., Effect of Potassium on the Kinetics of Ammonia Synthesis and Decomposition over Fused Iron Catalyst at Atmospheric Pressure, *Journal of Catalysis*, Vol. 169, **1997**, pp. 407-414.
29. Centi G., Perathoner S., Adsorption and Reactivity of No on Copper-on-Alumina Catalysts: II. Adsorbed Species and Competitive Pathways in the Reaction of No with NH_3 and O_2, *Journal of Catalysis*, Vol. 152, **1995**, pp. 93-102.

30. Staykov A., Komoda R., Kubota M., et al, Coadsorption of CO and H_2 on an Iron Surface and Its Implication on the Hydrogen Embrittlement of Iron, *The Journal of Physical Chemistry C*. Vol. 123, **2019**, pp. 30265-30273.

4 Reverse ammonia concentration effect on ammonia mitigated and induced hydrogen embrittlement at slower loading rate fracture toughness test

4.1 Introduction

As described in chapters 2 and 3, NH_3 has both mitigation and induction effects on hydrogen embrittlement by itself.

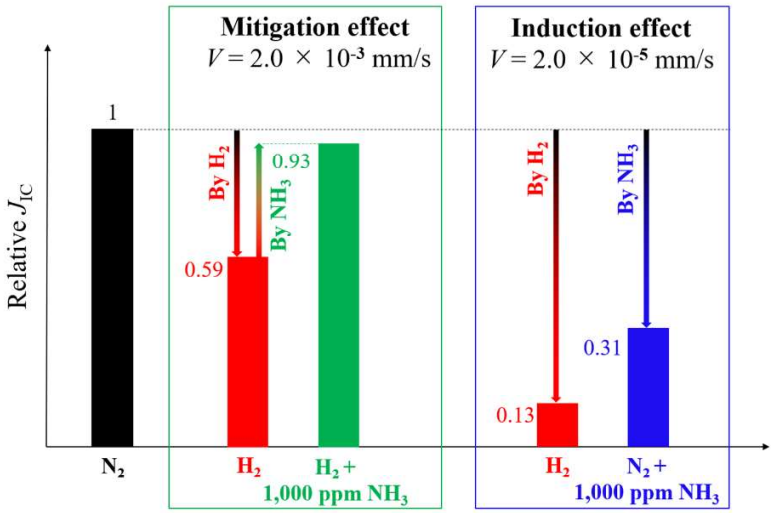

Fig. 4.1 Mitigation and induction effect of NH_3 on HE
(Relative J_{IC} = J_{IC}/J_{IC} in N_2)

In the chapter 2 (as shown in Fig. 4.1 green block), NH_3 showed the mitigation effect of HE in the fracture toughness test at the relatively higher loading rate, 2.0×10^{-5} mm/s. In the chapter 3 (as shown in Fig. 4.1 blue block), NH_3 showed the induction effect of HE in the fracture toughness test at the relatively lower loading rate, 2.0×10^{-5} mm/s. Based on these results, if the fracture toughness test is carried out in NH_3 added H_2 gas with a slower loading rate, it can be considered that the mitigation and induction effects simultaneously work and the fracture toughness test can characterize the phenomenon. Therefore, this chapter will investigate the competitive coadsorption of decomposed NH_3 and dissociated H_2 on the Fe

(110) surface. The effect of NH_3 concentration on the competitive reaction was investigated as well.

In the chapter 3, the decomposition effect of 11.11% NH_3 (1,000 ppm) coverage on the Fe (110) surface has been investigated, and the result showed that the coverage of hydrogen atoms on the Fe (110) surface was increased following the NH_3 decomposition occurred step by step as showed in the summary Table 4.1. In this chapter, the effect of NH_3 concentration on HE will be investigated. The point is that increase in the NH_3 concentration (1,000 vppm → 10,000 vppm) increases the NH_3 adsorption rate (2.77×10^{19} s^{-1}→ 5.88×10^{19} s^{-1}) and NH_3-derived hydrogen amount. Under such a situation, it seems that a higher amount of hydrogen atoms was created by the NH_3 decomposition. However, the fracture toughness test results showed the opposite effect as shown in Fig. 4.2, this chapter will clarify this phenomenon and mechanism by fracture toughness test and DFT calculations.

Table 4.1 Summary of NH_3-derived hydrogen coverage on Fe (110) surface (11.11% NH_3 coverage on Fe surface)

Reaction	NH_3-derived hydrogen coverage
$NH_3 \rightarrow NH_2 + H$ (Case A)	0.79%
$NH_3 \rightarrow NH + 2H$ (Case B)	4.06%
$NH_3 \rightarrow N + 3H$ (Case C)	4.06%

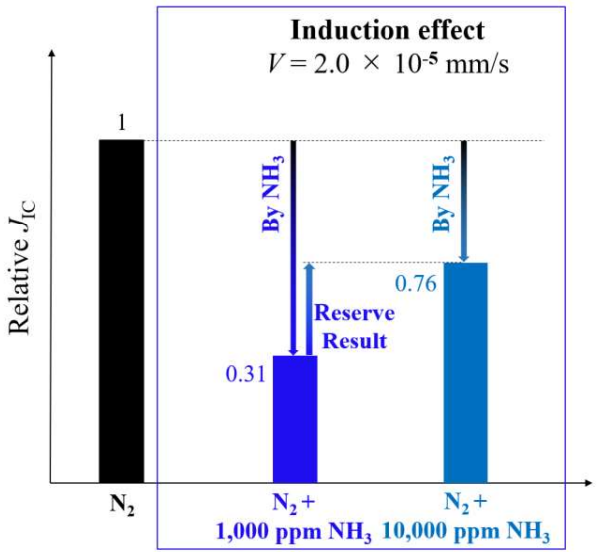

Fig. 4.2 Reserve result of NH_3 induced HE
(Relative J_{IC} = J_{IC}/J_{IC} in N_2)

4.2 Experimental procedure

4.2.1 Material

The material used in this chapter was JIS SCM440 Cr-Mo low-alloy steel, which is the same material used in the chapter 2. The heat treatment conditions are the same as that used in the chapter 2. The chemical composition and mechanical properties are shown in Tables 2.1 and 2.2, respectively. The microstructure of the material, which exhibits the tempered martensite microstructure, is shown in Fig. 2.1.

4.2.2 Fracture toughness test method and test environment

The fracture toughness tests were conducted in the accordance with the ASTM E 1820 standard with the same fracture toughness test system in the chapter 2. The fracture toughness test method and the CT specimen were the same used in the chapter 2.

The test environments were N_2, H_2, NH_3 added H_2 and NH_3 added N_2 gases. The amount of NH_3 in the mixture was 1,000 vppm and 10,000 vppm. The purity measurement of the testing environment and the method for keeping the high purity gas condition in the gas chamber were the same as described in the chapter 2.

The total absolute gas pressure at which the fracture toughness tests were carried out, p_T, was 0.1 MPa. The gas temperature was controlled at 293K by a thermocouple installed near the CT specimen and a heater and cooler system. The crosshead speed, V, was 2.0×10^{-5} mm/s.

4.3 Test results

The results of the fracture toughness tests in the H_2, N_2, NH_3 added H_2 gases and NH_3 added N_2 gases are shown in Figs. 4.3 and 4.5. The elastic-plastic fracture toughness values, J_{IC}, for each condition are shown in Table 4.2.

Figure 4.3 shows the J-Δa curve in the NH_3 added H_2 gases under the testing conditions of p_T = 0.1 MPa and $V = 2.0 \times 10^{-5}$ mm/s. The J-Δa curve in the H_2 (▲) at $V = 2.0 \times 10^{-5}$ mm/s was located significantly lower than that in N_2 (●). Regarding the J-Δa curve in H_2, the decreased loading rate caused further reduction as shown in Fig. 4.4. The J-Δa curve in the 1,000 ppm NH_3 and H_2 mixture (■) was slightly higher than H_2. The J-Δa curve in the 10,000 ppm NH_3 and H_2 mixture (◆) was slightly higher than the 1,000 ppm NH_3 and H_2 mixture. In H_2, the reduction in J_{IC} became more significant by the decreased loading rate. Regarding the effect of the NH_3, the J-Δa curves shifted upward compared with that in the H_2. Consequently, the J_{IC} values in the NH_3 added H_2 gases were greater than that in the H_2 gas. However, the HE mitigation by NH_3 was significantly weakened by the decreased loading rate.

Figure 4.5 shows the J-Δa curve in the NH_3 added N_2 gases under the testing conditions of p_T = 0.1 MPa and $V = 2.0 \times 10^{-5}$ mm/s. The J-Δa curve in the 1,000 ppm NH_3 and N_2 mixture (■) was located higher than that in H_2 (▲) and significantly lower than that in the N_2 (●). By comparing with Fig. 4.6, it can be recognized that the HE induction effect by NH_3 was significantly enhanced by the decreased loading rate. The J-Δa curve in the 10,000 ppm NH_3 and N_2 mixture (◆) was located obviously higher than that in the 1,000 ppm NH_3 and N_2 mixture. The HE induction effect by NH_3 was significantly enhanced by decreased NH_3 concentration.

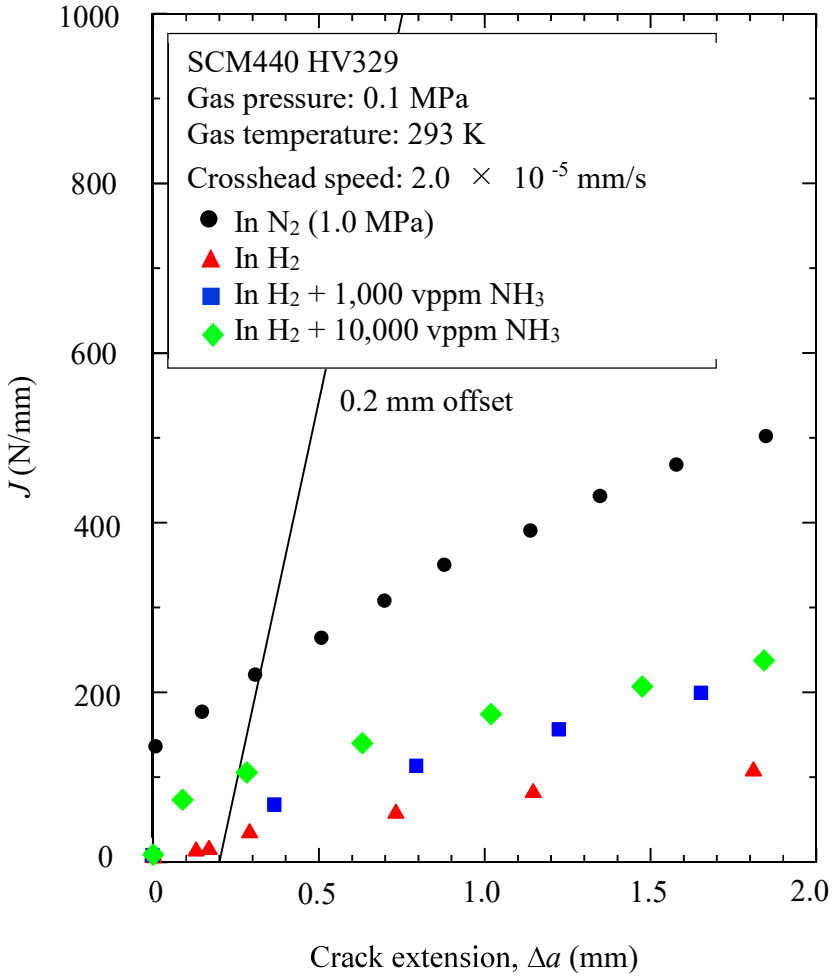

Fig. 4.3 Effect of NH_3 addition to H_2 environment on J-Δa curve at p_T = 0.1 MPa and $V = 2.0 \times 10^{-5}$ mm/s.

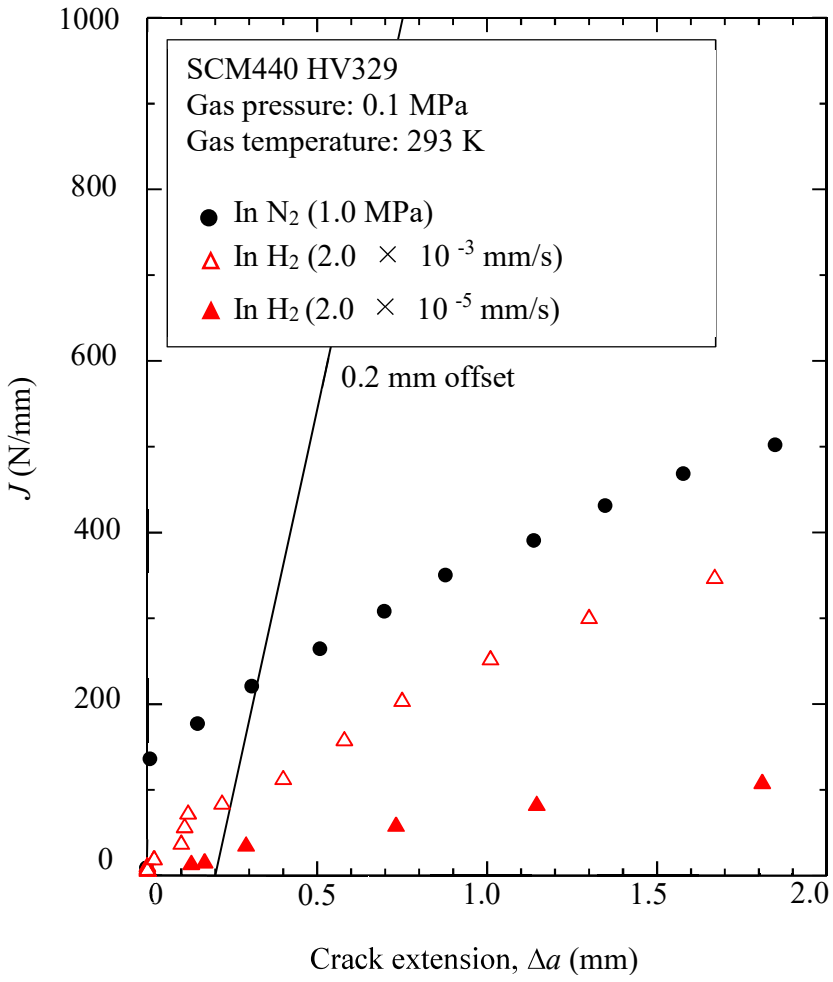

Fig. 4.4 Effect of loading rate reduction on HE by H_2 on J-Δa curve at p_T = 0.1 MPa.

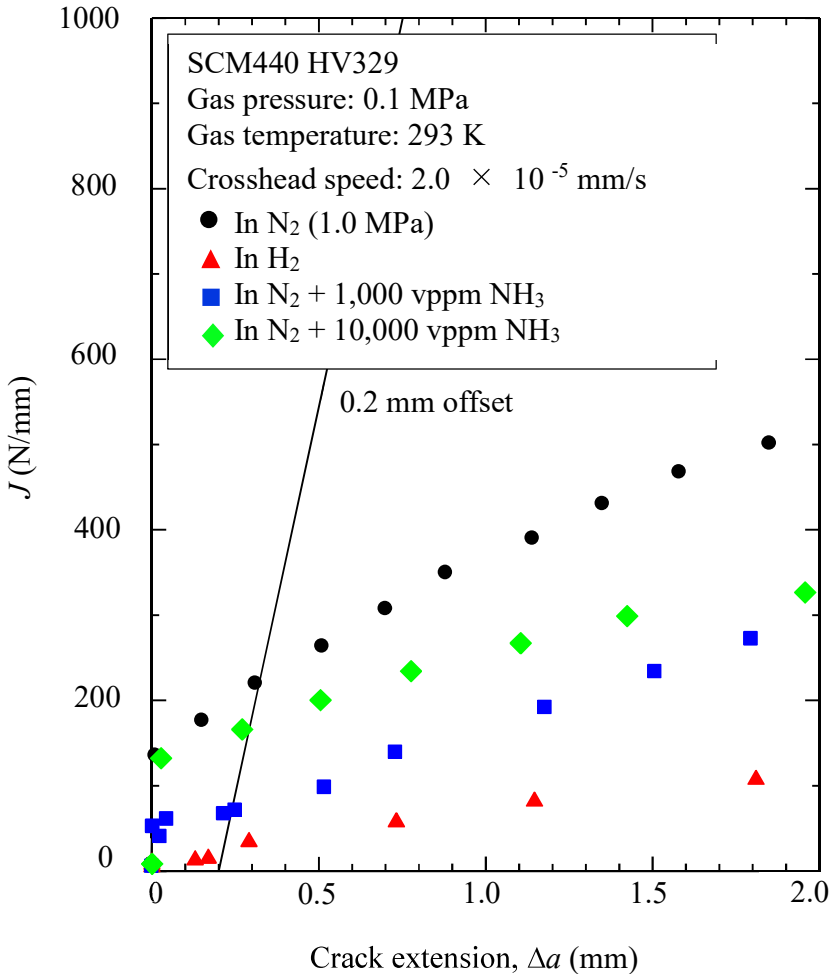

Fig. 4.5 Effect of NH_3 addition to N_2 environment on J-Δa curve at p_T = 0.1 MPa and $V = 2.0 \times 10^{-5}$ mm/s.

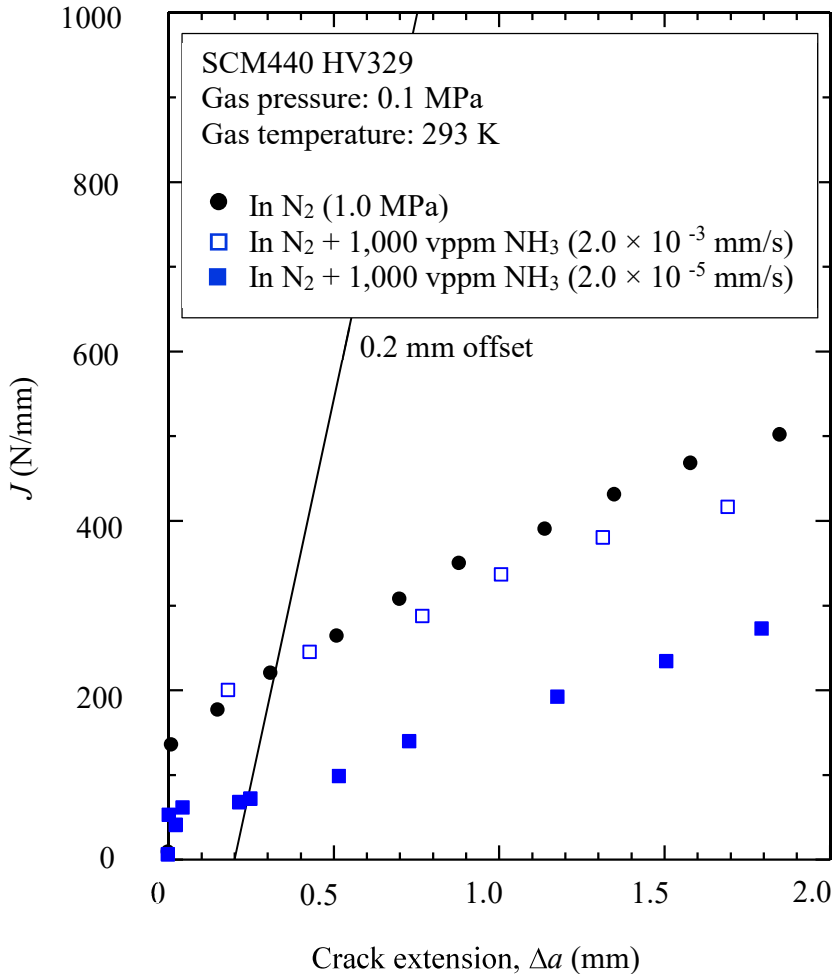

Fig. 4.6 Effect of loading rate reduction on NH_3 induction on J-Δa curve at p_T = 0.1 MPa.

Table 4.2. J_{IC} value in each condition. [---]: Relative value to J_{IC} in N_2

Environment	p_T = 0.1 MPa, V = 2.0×10^{-5} mm/s	p_T = 1.0 MPa, V = 2.0×10^{-3} mm/s
N_2		217 [1]
H_2	28 [0.13]	
H_2 + 1,000 ppmNH_3	47 [0.22]	
H_2 + 10,000 ppmNH_3	87 [0.40]	
N_2 + 1,000 ppmNH_3	67 [0.31]	
N_2 + 10,000 ppmNH_3	165 [0.76]	

p_T : Total environmental gas pressure

V : Cross head displacement rate

4.4 Discussion on the mechanism that reverse ammonia concentration effect on ammonia mitigates and induces hydrogen embrittlement on Fe (110) surface based on density functional theory

Regarding the loading rate dependency at 0.1 MPa of gas pressure, the J_{IC} value in the 1,000 vppm NH_3 added H_2 gas almost agreed with that in the N_2 when $V = 2.0 \times 10^{-3}$ mm/s as shown in Fig. 4.7, but was significantly reduced when $V = 2.0 \times 10^{-5}$ mm/s. The decreased loading rate reduced the NH_3's mitigation effect observed in the 1,000 vppm NH_3 added H_2. Meanwhile, hydrogen created by NH_3 decomposition assisted in decreasing the J_{IC} in the 1,000 vppm NH_3 added N_2 when $V = 2.0 \times 10^{-5}$ mm/s was also found in chapter 3. There are two possible reasons for the reduced mitigation effect in the 1,000 vppm NH_3 added H_2 due to lowered loading rate.

1) NH_3 molecule cannot cover the entire Fe surface, which has been investigated in the chapter 2. A similar loading rate dependency that the reduction in the loading rate reduces the mitigation effect was found in a paper studying the effect of CO on the HE mitigation [4 - 1]. In this paper, the CO adsorption behavior on a Fe surface was calculated by DFT simulations as a function of the CO coverage of the Fe surface. When the CO molecule adsorbs on the Fe surface, CO withdraws and localizes the electrons of the Fe surface. As a consequence, the electron density at the CO-free site is not enough to establish a chemical interaction with another CO molecule. As a result, CO achieved 75.00% maximum coverage of the Fe surface. On the other hand, hydrogen can adsorb on the CO-free sites. That is, the mitigation of the HE by CO is achieved by the reduced hydrogen uptake in conjunction with a higher loading rate. In this situation, the reduction in the loading rate means an increase in the amount of hydrogen entry into the material. Consequently, the mitigation of HE by CO is diminished by reducing the loading rate.

In contrast, O_2 adsorbs on the Fe surface through dissociation into oxygen atoms. Oxygen atoms on the Fe surface can diffuse into the material. An oxygen-free site is created again, then another oxygen atom adsorption occurs. Repeated these processes create an oxide layer. Thus, a perfectly covered Fe surface by the iron oxide results in the prevention of

hydrogen entry. Hence, no loading rate effect on the mitigation effect of O_2 after the oxygen atom achieved 100.00% coverage on the Fe surface [4 - 2, 4 - 3].

Regarding NH_3, the coverage of NH_3 adsorbs on the Fe (110) surface as a molecule could not reach 100.00% which has been calculated in the chapter 2. Therefore, the same mechanism of CO that the coverage of the Fe surface is not 100.00% can be also considered for NH_3.

2) NH_3 can produce hydrogen atoms by its decomposition and lead HE when $V = 2.0 \times 10^{-5}$ mm/s, which has been investigated in chapter 3.

The possible reason for the weakened NH_3 mitigation effect due to the reduction in the loading rate is hydrogen created by the NH_3 decomposition. The point is that the NH_3 first step decomposition rate was significantly lower than the NH_3 adsorption rate (k: 1.36×10^{8} $s^{-1} < 3.14 \times 10^{20}$ s^{-1}). Therefore, decreased loading rate supplied the time for NH_3 decomposition. On the other hand, even just 11.11% NH_3 covered Fe (110) surface can bring 4.06% hydrogen atom coverage when only considering NH_3 reaction with Fe surface. Such an amount of hydrogen coverage at $V = 2.0 \times 10^{-5}$ mm/s was possible to lead to HE [4 - 1]. Therefore, the weakening effect became tangible when the loading rate is reduced. However, in this case, the result cannot be interpreted only by the adsorption rate and coverage of NH_3 as a molecule on the Fe (110) surface. It is necessary to consider the adsorption and decomposition process of NH_3 on the Fe (110) surface, which competes with the hydrogen dissociation process. Therefore, the coverage of hydrogen atoms on Fe (110) surface when considering decomposed NH_3 and dissociated H_2 competitive reaction was investigated in this section.

In 0.1 MPa, the J_{IC} value in the 1,000 vppm NH_3 added N_2 significantly reduced when $V = 2.0 \times 10^{-5}$ mm/s (67 N/mm). The reduction is due to the NH_3-derived hydrogen-covered Fe surface, which has been studied in the chapter 3. However, the J_{IC} value was obviously increased when NH_3 concentration was increased to 10,000 vppm (165 N/mm). Because NH_3 is the only hydrogen source under this testing condition, it can be expected that the increased hydrogen supply by the increased NH_3 concentration led to a reduction in J_{IC} value. However, the result obtained by the experiment was opposite to this prediction. Therefore, the

mechanism that which NH_3 concentration affects HE induction has to be clarified. This mechanism will be investigated by DFT in this Chapter. The methods and theories for the investigation were the same as described in the chapter 1.5.

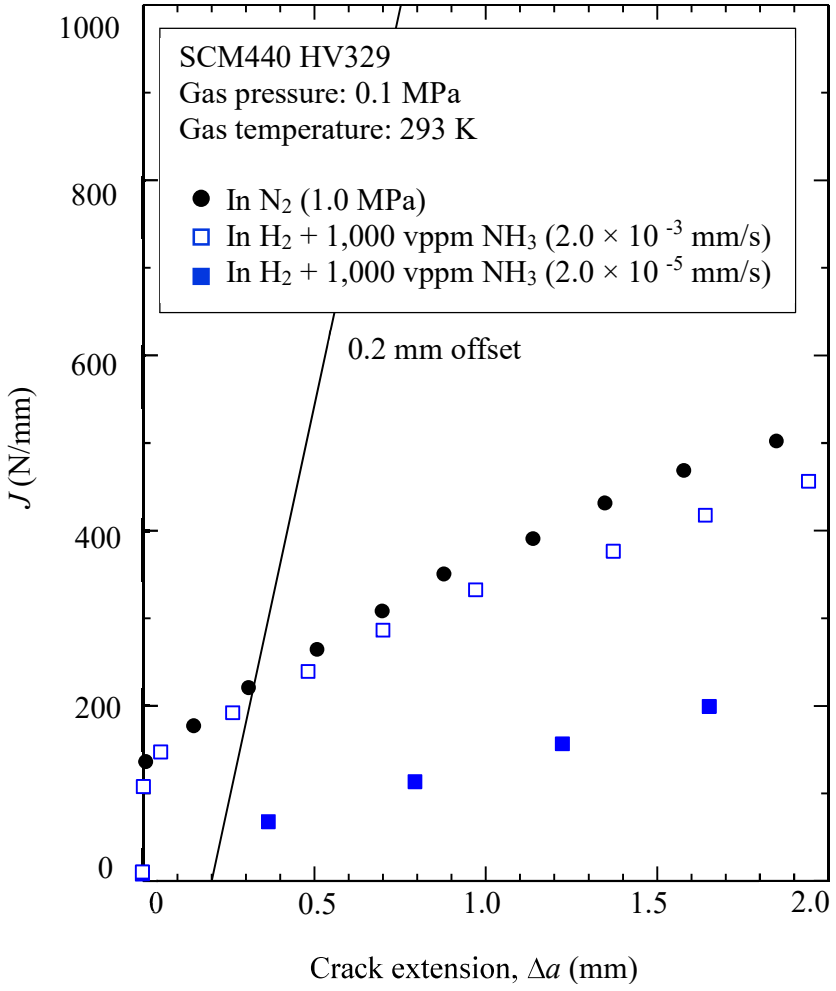

Fig. 4.7 Effect of loading rate reduction on NH_3 mitigation on J-Δa curve at p_T = 0.1 MPa.

4.4.1 Ammonia decomposition with Fe (110) surface catalysis under a higher NH_3 concentration

When gaseous species interact with the solid surface, which will establish an equilibrium between the gaseous phase, adsorbed species, and the surface of the solid. As with the chemical equilibrium, an increase in the gas concentration leads to an increasing the coverage of the gas on the solid surface at the constant temperature [4 - 4 - 4 - 6]. Thus, to investigate the effect of NH_3 concentration on HE, study in chapter 3.4.2 was further advanced, I investigate the decomposition of NH_3 with a higher NH_3 coverage (25.00%) on Fe (110) surface in this section. The method was the same as described in the chapter 3.4.1.

The minimum activation energy barrier (E_a) site of NH_3 decomposition in each step (initial geometry, transition geometry, and end geometry) is shown in Figs. 4.8 - 4.10. Though the decomposition occupied the site of species not changed as shown in Table 3.3 in the chapter 3. As shown in Table 4.3, The E_a of 25.00% NH_3 coverage on the Fe (110) surface, was greatly changed in the second step ($NH_2 \rightarrow NH + H$) and the third step ($NH \rightarrow N + H$) of NH_3 decomposition. The E_a of the second decomposition step almost doubled, whereas the reaction of the third decomposition step transformed from an exothermic reaction to an endothermic reaction. The exothermic reactions released energy while the endothermic reactions required energy. As a result, increased NH_3 concentration made NH_3 decomposition even harder.

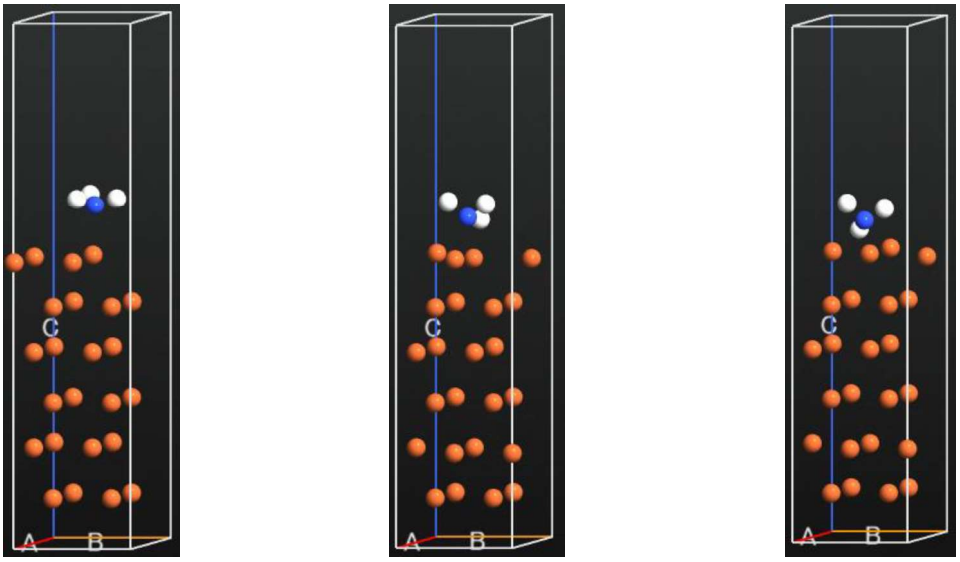

(a) Initial (b) Transition (c) End

Fig. 4.8 NH_3-derived hydrogen atom Fe (110) surface. (a) Initial, (b) Transition, (c) End.

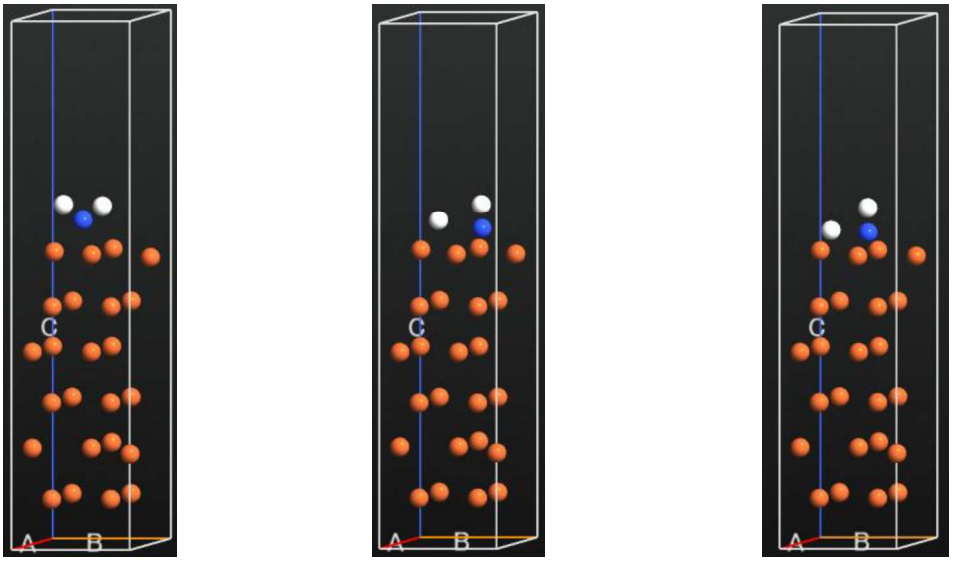

(a) Initial (b) Transition (c) End

Fig. 4.9 NH_2-derived hydrogen atom Fe (110) surface. (a) Initial, (b) Transition, (c) End.

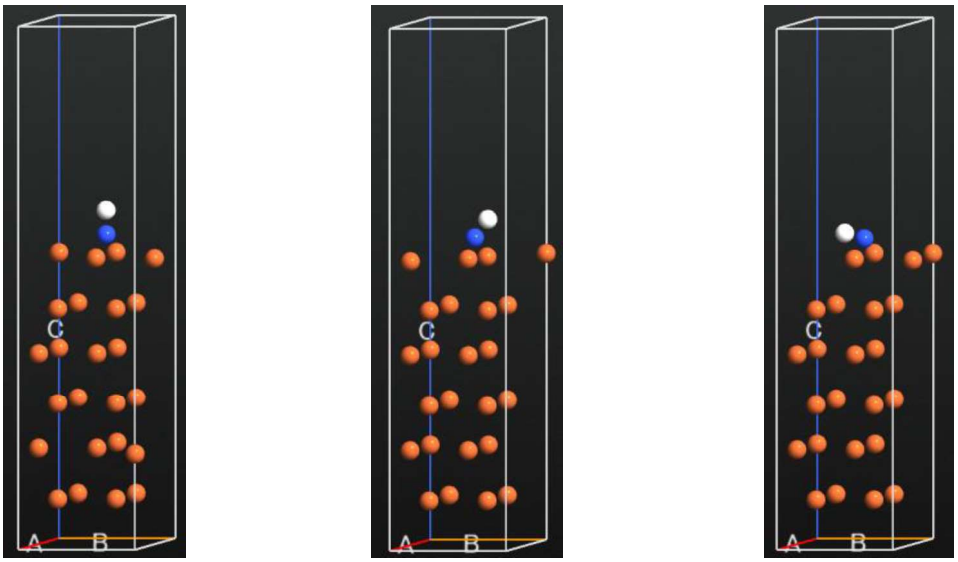

(a) Initial (b) Transition (c) End

Fig. 4.10 NH-derived hydrogen atom Fe (110) surface. (a) Initial, (b) Transition, (c) End.

Table 4.3 Decomposition and desorption E_a of NH_3

	Decomposition activation barrier	Desorption activation barrier
$NH_3 \rightarrow NH_2 + H$	0.68 eV (Exo)	1.39 eV (Endo)
$NH_2 \rightarrow NH + H$	0.84 eV (Exo)	1.70 eV (Endo)
$NH \rightarrow N + H$	1.05 eV (Endo)	0.98 eV (Exo)

Exo = Exothermic reaction

Endo = Endothermic reaction

4.4.2 Equation establish of calculation ammonia decomposition and hydrogen dissociation on Fe (110) surface: kinetic modeling of competitive coadsorption between NH_3 and H_2

The concept of chemical equilibrium was described in the chapter 3.4.4. In this section, I investigated the NH_3 decomposition in the same way in the chapter 3 and divided the process of NH_3 decomposition into four steps, but considered the dissociation of H_2 simultaneously.

(I) $NH_3 + * \overset{\overrightarrow{k_1},\ \overleftarrow{k_1}}{\longleftrightarrow} NH_3*$

(II) $NH_3* + * \overset{\overrightarrow{k_2},\ \overleftarrow{k_2}}{\longleftrightarrow} NH_2* + H*$

(III) $NH_2* + * \overset{\overrightarrow{k_3},\ \overleftarrow{k_3}}{\longleftrightarrow} NH* + H*$

(IV) $NH* + * \overset{\overrightarrow{k_4},\ \overleftarrow{k_4}}{\longleftrightarrow} N* + H*$

To establish the kinetic modeling of competitive coadsorption between NH_3 and H_2 on the Fe (110) surface, considering the H_2 dissociation process is also needed. The reaction of H_2 dissociation on the Fe surface can be considered as the chemical equation (V) below:

(V) $H_2 + 2* \leftrightarrow 2H*$

The term $*$ denotes a vacant site, and NH_3*, NH_2*, $NH*$, $N*$, and $H*$ are the adsorbed species. NH_3 and H_2 represent the free gaseous state. If all the above reactions are equilibrium that the constants of equilibrium can be expressed in terms of concentration of adsorbed species as:

$$K_1 = \frac{\overrightarrow{k_1}}{\overleftarrow{k_1}} = \frac{[\mathrm{NH3*}]}{\rho_{NH3}[*]} \tag{4.1}$$

Where the $\overrightarrow{k_1}$ and $\overleftarrow{k_1}$ represent the rate constant coefficient of the reaction I of forward reaction and backward reaction, respectively. K_1 is the equilibrium constant of reaction I.

$$K_2 = \frac{\overrightarrow{k_2}}{\overleftarrow{k_2}} = \frac{[\mathrm{NH2*}][\mathrm{H*}]}{[\mathrm{NH3*}][*]} \tag{4.2}$$

Where the $\overrightarrow{k_2}$ and $\overleftarrow{k_2}$ represent the rate constant coefficient of the reaction II of forward reaction and backward reaction, respectively. K_2 is the equilibrium constant of reaction II.

$$K_3 = \frac{\overrightarrow{k_3}}{\overleftarrow{k_3}} = \frac{[\mathrm{NH*}][\mathrm{H*}]}{[\mathrm{NH2*}][*]} \tag{4.3}$$

Where the $\overrightarrow{k_3}$ and $\overleftarrow{k_3}$ represent the rate constant coefficient of the reaction III of forward reaction and backward reaction, respectively. K_3 is the equilibrium constant of reaction Ⅲ.

$$K_4 = \frac{\overrightarrow{k_4}}{\overleftarrow{k_4}} = \frac{[\mathrm{N*}][\mathrm{H*}]}{[\mathrm{NH*}][*]} \tag{4.4}$$

Where the $\overrightarrow{k_4}$ and $\overleftarrow{k_4}$ represent the rate constant coefficient of the reaction IV of forward reaction and backward reaction, respectively. K_4 is the equilibrium constant of reaction Ⅳ.

$$K_5 = \frac{\overrightarrow{k_5}}{\overleftarrow{k_5}} = \frac{[\mathrm{H*}]^2}{\rho_{NH3}[*]^2} \tag{4.5}$$

Where the $\overrightarrow{k_5}$ and $\overleftarrow{k_5}$ represent the rate constant coefficient of the reaction Ⅴ of forward reaction and backward reaction, respectively. K_5 is the equilibrium constant of reaction Ⅴ.

The reaction rate coefficient *k* ($\overrightarrow{k_1}$, $\overleftarrow{k_1}$, $\overrightarrow{k_2}$, $\overleftarrow{k_2}$, $\overrightarrow{k_3}$, $\overleftarrow{k_3}$, $\overrightarrow{k_4}$, $\overleftarrow{k_4}$) in each step is given by Arrhenius equation in equation 1.4.

There is one thing that needs to be noted is that the model of coverage calculation elides the computation of the preexponential factor *A,* while it will be calculated in the next section to calculate the reaction rate coefficient. Such an approximation is only partially justified in coverage calculation because the preexponential factors for adsorption and desorption (opposite reaction) processes would cancel.

Then, I investigate the hydrogen atom coverage on Fe (110) surface step by step competing with H_2 dissociation and assumed the reaction can stop at each step, and assumed the equilibrium state at that moment.

Case A: I assumed the reaction of NH_3 decomposition reaches the state which has the NH_2 and H atom as products and has equilibrium (reaction I, II) competing with H_2 dissociation (V). Therefore, the equilibrium equations will be given by the following equations 4.6, 4.7, and 4.8.

(I) $NH_3 + * \rightarrow NH_3*$

(II) $NH_3* + * \rightarrow NH_2* + H*$

(V) $H_2 + 2* \leftrightarrow 2H*$

$$\overrightarrow{k_1}\rho_{NH_3}\theta_v = \overleftarrow{k_1}\theta_{NH_3*} \tag{4.6}$$

$$\overrightarrow{k_2}\theta_{NH_3*}\theta_v = \overleftarrow{k_2}\theta_{NH_2*}\theta_{H*(NH_3)} \tag{4.7}$$

$$\overrightarrow{k_5}\rho_{H_2}{\theta_v}^2 = \overleftarrow{k_5}{\theta_{H*(H_2)}}^2 \tag{4.8}$$

Where θ_{NH_3*}, θ_{NH_2*}, $\theta_{H*(NH_3)}$, and $\theta_{H*(H_2)}$ are denoted fractional coverage of NH_3, NH_2, and H atom adsorbed on the Fe (110) surface respectively. θ_v is denoted fractional coverage of the vacant site. θ_{NH_2*} equal to $\theta_{H*(NH_3)}$ as equilibrium. ρ_{NH_3} is denoted the partial pressure of gaseous NH_3. $\overrightarrow{k_1}$, $\overleftarrow{k_1}$, $\overrightarrow{k_2}$, $\overleftarrow{k_2}$, $\overrightarrow{k_5}$, and $\overleftarrow{k_5}$ are the reaction rate coefficient for decomposition and desorption, which is given by the Arrhenius equation (eqs 1.4). The temperature is 293K to fit the fracture toughness test condition.

Based on the assumption that reactions I, II, and V are achieved equilibrium, the adsorbed species on the Fe (110) surface in the Case A are NH_3*, NH_2*, and $H*$ atom (from NH_3 and H_2), and the remaining sites are vacant. Therefore, the entire surface can be

considered into five parts, θ_{NH_3*} represents the fractional coverage of NH_3, θ_{NH_2*} represents the fractional coverage of NH_2, $\theta_{H*(NH3)}$ represents the fractional coverage of hydrogen atom from NH_3 decomposition, θ_{H*} represents the fractional coverage of hydrogen atom from H_2 dissociation, θ_v represents the fractional coverage of the vacant site. Thus, the entire surface will be given by the following equation 4.9.

$$\theta_{NH_3*} + \theta_v + \theta_{NH_2*} + \theta_{H*(NH_3)} + \theta_{H*(H_2)} = 1 \tag{4.9}$$

From equations 4.6 - 4.9, the fractional coverage of all adsorbed species can be calculated as equations as follows:

$$\theta_v = \frac{1}{K_1\rho_{NH_3}+2\sqrt{K_1K_2\rho_{NH_3}}+\sqrt{K_5\rho_{H_2}}+1} \tag{4.10}$$

$$\theta_{NH_3*} = \frac{k_1\rho_{NH_3}}{k_1\rho_{NH_3}+2\sqrt{k_1k_2\rho_{NH_3}}+\sqrt{K_5\rho_{H_2}}+1} \tag{4.11}$$

$$\theta_{NH_2*} = \theta_{H*(NH_3)} = \frac{\sqrt{k_1k_2\rho_{NH_3}}}{k_1\rho_{NH_3}+2\sqrt{k_1k_2\rho_{NH_3}}+\sqrt{K_5\rho_{H_2}}+1} \tag{4.12}$$

$$\theta_{H*} = \theta_{H*(NH_3)} + \theta_{H*(H_2)} = \frac{\sqrt{k_1k_2\rho_{NH_3}}+\sqrt{K_5\rho_{H_2}}}{k_1\rho_{NH_3}+2\sqrt{k_1k_2\rho_{NH_3}}+\sqrt{K_5\rho_{H_2}}+1} \tag{4.13}$$

Based on equations 4.10 - 4.13, the coverage of adsorbed species on the Fe (110) surface in the Case A can be calculated. The coverage of adsorbed species in the Case A is shown in Table 4.4.

Table 4.4 Adsorbed species coverage on Fe (110) in Case A

	Coverage (1,000 vppm NH_3)	Coverage (10,000 vppm NH_3)
θ_{NH_3*}	8.88%	20.60%
θ_{H_2*}	1.49%	4.37%
θ_{H*}	2.96%	4.37%

Case B: I assumed the reaction of NH_3 decomposition reaches the state which has the NH_2, NH, and H atom as products and has equilibrium (reaction I, II, III) competing with H_2 dissociation (V). Therefore, the equilibrium equations will be given by the following equations 4.14, 4.15, 4.16, and 4.17.

(I) $NH_3 + * \rightarrow NH_3*$

(II) $NH_3* + * \rightarrow NH_2* + H*$

(III) $NH_2* + * \rightarrow NH* + H*$

(V) $H_2 + 2* \leftrightarrow 2H*$

$$\overrightarrow{k_1}\rho_{NH_3}\theta_v = \overleftarrow{k_1}\theta_{NH_3*} \tag{4.14}$$

$$\overrightarrow{k_2}\theta_{NH_3*}\theta_v = \overleftarrow{k_2}\theta_{NH_2*}\theta_{H*(NH_3)} \tag{4.15}$$

$$\overrightarrow{k_3}\theta_{NH_2*}\theta_v = \overleftarrow{k_3}\theta_{NH*}\theta_{H*(NH_2)} \tag{4.16}$$

$$\overrightarrow{k_5}\rho_{H_2}\theta_v^{\,2} = \overleftarrow{k_5}\theta_{H*(H_2)}^{\,2} \tag{4.17}$$

Where θ_{NH_3*}, θ_{NH_2*}, θ_{NH*}, $\theta_{H*(NH_3)}$, $\theta_{H*(NH_2)}$, $\theta_{H*(H_2)}$ are denoted fractional coverage of NH_3, NH_2, NH, and H atom adsorbed on the Fe (110) surface, respectively. θ_v is denoted

fractional coverage of the vacant site. $\theta_{NH_{2}*}$ equal to $\theta_{H*(NH_3)}$ as equilibrium. θ_{NH*} equal to $\theta_{H*(NH_2)}$ as equilibrium. ρ_{NH3} is denoted the partial pressure of gaseous NH_3. $\overrightarrow{k_1}$, $\overleftarrow{k_1}$, $\overrightarrow{k_2}$, $\overleftarrow{k_2}$, $\overrightarrow{k_3}$, $\overleftarrow{k_3}$, $\overrightarrow{k_5}$, and $\overleftarrow{k_5}$ are the reaction rate coefficient for decomposition and desorption, which is given by the Arrhenius equation (eq 1.4). The temperature is 293K to fit the fracture toughness test condition.

Based on the assumption that reactions I, II, III, and V are achieved equilibrium, the adsorbed species on the Fe (110) surface in the Case B are NH_3*, NH_2*, NH*, and H* atom (from NH_3, NH_2, and H_2), and the remaining sites are vacant. Therefore, the entire surface can be considered into six parts, θ_{NH_3*} represents the fractional coverage of NH_3, θ_{NH_2*} represents the fractional coverage of NH_2, θ_{NH*} represents the fractional coverage of NH, $\theta_{H*(NH_3)}$ represents the fractional coverage of hydrogen atom from NH_3, $\theta_{H*(NH_2)}$ represents the fractional coverage of hydrogen atom from NH_2, $\theta_{H*(H_2)}$ represents the fractional coverage of hydrogen atom from H_2, θ_v represents the fractional coverage of the vacant site. Thus, the entire surface will be given by the following equation 4.18.

$$\theta_{NH_3*} + \theta_v + \theta_{NH_2*} + \theta_{H*(NH_3)} + \theta_{NH*} + \theta_{H*(NH_2)} + \theta_{H*(H_2)} = 1 \tag{4.18}$$

From equations 4.14 - 4.18, the fractional coverage of all adsorbed species can be calculated as equations as follows:

$$\theta_v = \frac{1}{K_1\rho_{NH_3}+2\sqrt{K_1K_2\rho_{NH_3}}+2\sqrt{K_3\sqrt{K_1K_2\rho_{NH_3}}+\sqrt{K_5\rho_{H_2}}+1}} \tag{4.19}$$

$$\theta_{NH_3*} = \frac{K_1\rho_{NH_3}}{K_1\rho_{NH_3}+2\sqrt{K_1K_2\rho_{NH_3}}+2\sqrt{K_3\sqrt{K_1K_2\rho_{NH_3}}+\sqrt{K_5\rho_{H_2}}+1}} \tag{4.20}$$

$$\theta_{NH_2*} = \frac{\sqrt{K_1K_2\rho_{NH_3}}}{K_1\rho_{NH_3}+2\sqrt{K_1K_2\rho_{NH_3}}+2\sqrt{K_3\sqrt{K_1K_2\rho_{NH_3}}+\sqrt{K_5\rho_{H_2}}+1}} \tag{4.21}$$

$$\theta_{NH*} = \frac{\sqrt{K_3\sqrt{K_1K_2\rho_{NH_3}}}}{K_1\rho_{NH_3}+2\sqrt{K_1K_2\rho_{NH_3}}+2\sqrt{K_3\sqrt{K_1K_2\rho_{NH_3}}}+\sqrt{K_5\rho_{H_2}}+1} \quad (4.22)$$

$$\theta_{H*} = \theta_{H*(NH_3)} + \theta_{H*(NH_2)} + \theta_{H*(H_2)}$$

$$= \frac{\sqrt{K_1K_2\rho_{NH_3}}+\sqrt{K_3\sqrt{K_1K_2\rho_{NH_3}}}+\sqrt{K_5\rho_{H_2}}}{K_1\rho_{NH_3}+2\sqrt{K_1K_2\rho_{NH_3}}+2\sqrt{K_3\sqrt{K_1K_2\rho_{NH_3}}}+\sqrt{K_5\rho_{H_2}}+1} \quad (4.23)$$

Based on the equations 4.19 - 4.23, the coverage of adsorbed species on the Fe (110) surface in the Case B can be calculated. The coverage of adsorbed species in the Case B is shown in Table 4.5.

Table 4.5 Adsorbed species coverage on Fe (110) in Case B

	Coverage (1,000 vppm NH_3)	Coverage (10,000 vppm NH_3)
θ_{NH_3*}	2.93%	9.80%
θ_{NH_2*}	0.49%	2.07%
θ_{NH*}	11.16%	19.67%
θ_{H*}	8.42%	15.20%

Case C: I assumed the reaction of NH_3 decomposition reaches the state which has the NH_2, NH, N, and H atom as products and has equilibrium (reaction I, II, III, IV) competing with H_2 dissociation (V). Therefore, the equilibrium equations will be given by the following equations 4.24, 4.25, 4.26, 4.27, and 4.28.

(I) $NH_3 + * \rightarrow NH_3*$

(II) $NH_3* + * \rightarrow NH_2* + H*$

(III) $NH_2* + * \rightarrow NH* + H*$

(IV) $NH* + * \rightarrow N* + H*$

(V) $H_2 + 2* \leftrightarrow 2H*$

$$\overrightarrow{k_1}\rho_{NH_3}\theta_v = \overleftarrow{k_1}\theta_{NH_3*} \tag{4.24}$$

$$\overrightarrow{k_2}\theta_{NH_3*}\theta_v = \overleftarrow{k_2}\theta_{NH_2*}\theta_{H*(NH_3)} \tag{4.25}$$

$$\overrightarrow{k_3}\theta_{NH_2*}\theta_v = \overleftarrow{k_3}\theta_{NH*}\theta_{H*(NH_2)} \tag{4.26}$$

$$\overrightarrow{k_4}\theta_{NH*}\theta_v = \overleftarrow{k_4}\theta_{N*}\theta_{H*(NH)} \tag{4.27}$$

$$\overrightarrow{k_5}\rho_{H_2}{\theta_v}^2 = \overleftarrow{k_5}{\theta_{H*(H_2)}}^2 \tag{4.28}$$

Where θ_{NH_3*}, θ_{NH_2*}, θ_{NH*}, θ_{N*}, $\theta_{H*(NH_3)}$, $\theta_{H*(NH_2)}$, $\theta_{H*(NH)}$, $\theta_{H*(H_2)}$ are denoted fractional coverage of NH_3, NH_2, NH, N, and H atom adsorbed on the Fe (110) surface, respectively. θ_v is denoted fractional coverage of the vacant site. θ_{NH_2*} equal to $\theta_{H*(NH_3)}$ as equilibrium. θ_{NH*} equal to $\theta_{H*(NH_2)}$ as equilibrium. θ_{N*} equal to $\theta_{H*(NH)}$ as equilibrium. ρ_{NH3} is denoted the partial pressure of gaseous NH_3. $\overrightarrow{k_1}$, $\overleftarrow{k_1}$, $\overrightarrow{k_2}$, $\overleftarrow{k_2}$, $\overrightarrow{k_3}$, $\overleftarrow{k_3}$, $\overrightarrow{k_4}$, $\overleftarrow{k_4}$, $\overrightarrow{k_5}$, and $\overleftarrow{k_5}$ are the reaction rate coefficient for decomposition and desorption, which is given by the Arrhenius equation (eq 1.4). The temperature is 293K to fit the fracture toughness test condition.

Based on the assumption that reactions I, II, III, IV, and V are achieved equilibrium, the adsorbed species on the Fe (110) surface in Case C are NH_3*, NH_2*, NH*, N*, and H* atom (from NH_3, NH_2, NH, and H_2), and the remaining sites are vacant. Therefore, the

entire surface can be considered into six parts, θ_{NH_3*} represents the fractional coverage of NH_3, θ_{NH_2*} represents the fractional coverage of NH_2, θ_{NH*} represents the fractional coverage of NH, $\theta_{H*(NH_3)}$ represents the fractional coverage of hydrogen atom from NH_3, $\theta_{H*(NH_2)}$ represents the fractional coverage of hydrogen atom from NH_2, $\theta_{H*(H_2)}$ represents the fractional coverage of hydrogen atom from H_2, θ_v represents the fractional coverage of the vacant site. Thus, the entire surface will be given by the following equation 4.29.

$$\theta_{NH_3*} + \theta_v + \theta_{NH_2*} + \theta_{H*(NH_3)} + \theta_{NH*} + \theta_{H*(NH_2)} + \theta_{N*} + \theta_{H*(NH)} \; \theta_{H*(H_2)} = 1 \tag{4.29}$$

From eqs 4.24 - 4.29, the fractional coverage of all adsorbed species can be calculated as equations as follows:

$$\theta_v = \frac{1}{K_1\rho_{NH_3}+2\sqrt{K_1K_2\rho_{NH_3}}+2\sqrt{K_3\sqrt{K_1K_2\rho_{NH_3}}}+2\sqrt{K_4\sqrt{K_3\sqrt{K_1K_2\rho_{NH_3}}}}+\sqrt{K_5\rho_{H_2}}+1} \tag{4.30}$$

$$\theta_{NH_3*} = \frac{K_1\rho_{NH_3}}{K_1\rho_{NH_3}+2\sqrt{K_1K_2\rho_{NH_3}}+2\sqrt{K_3\sqrt{K_1K_2\rho_{NH_3}}}+2\sqrt{K_4\sqrt{K_3\sqrt{K_1K_2\rho_{NH_3}}}}+\sqrt{K_5\rho_{H_2}}+1} \tag{4.31}$$

$$\theta_{NH_2*} = \frac{\sqrt{K_1K_2\rho_{NH_3}}}{K_1\rho_{NH_3}+2\sqrt{K_1K_2\rho_{NH_3}}+2\sqrt{K_3\sqrt{K_1K_2\rho_{NH_3}}}+2\sqrt{K_4\sqrt{K_3\sqrt{K_1K_2\rho_{NH_3}}}}+\sqrt{K_5\rho_{H_2}}+1} \tag{4.32}$$

$$\theta_{NH*} = \frac{\sqrt{K_3\sqrt{K_1K_2\rho_{NH_3}}}}{K_1\rho_{NH_3}+2\sqrt{K_1K_2\rho_{NH_3}}+2\sqrt{K_3\sqrt{K_1K_2\rho_{NH_3}}}+2\sqrt{K_4\sqrt{K_3\sqrt{K_1K_2\rho_{NH_3}}}}+\sqrt{K_5\rho_{H_2}}+1} \tag{4.33}$$

$$\theta_{N*} = \frac{\sqrt{K_4\sqrt{K_3\sqrt{K_1K_2\rho_{NH_3}}}}}{K_1\rho_{NH_3}+2\sqrt{K_1K_2\rho_{NH_3}}+2\sqrt{K_3\sqrt{K_1K_2\rho_{NH_3}}}+2\sqrt{K_4\sqrt{K_3\sqrt{K_1K_2\rho_{NH_3}}}}+\sqrt{K_5\rho_{H_2}}+1} \tag{4.34}$$

$$\theta_{H*} = \theta_{H*(NH_3)} + \theta_{H*(NH_2)} + \theta_{H*(NH)} + \theta_{H*(H_2)}$$

$$= \frac{\sqrt{K_1K_2\rho_{NH_3}} + \sqrt{K_3\sqrt{K_1K_2\rho_{NH_3}}} + \sqrt{K_4\sqrt{K_3\sqrt{K_1K_2\rho_{NH_3}}} + \sqrt{K_5\rho_{H_2}}}}{K_1\rho_{NH_3} + 2\sqrt{K_1K_2\rho_{NH_3}} + 2\sqrt{K_3\sqrt{K_1K_2\rho_{NH_3}}} + 2\sqrt{K_4\sqrt{K_3\sqrt{K_1K_2\rho_{NH_3}}} + \sqrt{K_5\rho_{H_2}}} + 1} \quad (4.35)$$

Based on the equations 4.30 - 4.35, the coverage of adsorbed species on the Fe (110) surface in the Case C can be calculated. The coverage of adsorbed species in the Case C is shown in Table 4.6.

Table 4.6 Adsorbed species coverage on Fe (110) in Case C

	Coverage (1000 vppm NH_3)	Coverage (10,000 vppm NH_3)
θ_{NH_3*}	2.93%	9.80%
θ_{NH_2*}	0.49%	2.07%
θ_{NH*}	11.16%	19.67%
θ_{N*}	9.48×10^{-6}%	1.84×10^{-7}%
θ_{H*}	8.42%	15.20%

The hydrogen coverage in each case was summarized in Table 4.7, from Case A to Case C, following the process of NH_3 decomposition, the hydrogen atom coverage on Fe (110) significantly increased from 2.96% to 8.42% (1,000 vppm NH_3), 4.73% to 15.20% (10,000 vppm NH_3). From the hydrogen atom coverage on Fe (110) surface, the coverage increased with NH_3 decomposition and an increase in NH_3 concentration. When NH_3 competitive adsorption with H_2 on Fe surface, the hydrogen atom coverage mainly came from NH_3 decomposition. However, as the fracture toughness test results in the H_2 + NH_3

showed, with increase in the NH_3 concentration, the J_{IC} value was increased from 47 N/mm (H_2 + 1,000 vppm NH_3 when $V = 2.0\times10^{-5}$ mm/s) increased to 87 N/mm (H_2 + 10,000 vppm NH_3 when $V = 2.0\times10^{-5}$ mm/s). Up to now, the theory and experiment results are opposite, which can be explained through the reaction rate of NH_3 decomposition, so the decomposition rate of NH_3 decomposition in each step will be calculated in the next section.

Table 4.7 Summary of hydrogen coverage on Fe (110) surface

	H Coverage 1,000 vppm NH_3 + H_2	H Coverage 10,000 vppm NH_3 + H_2
Case A	2.96%	4.37%
Case B	8.42%	15.20%
Case C	8.42%	15.20%

4.4.3 Reaction rate coefficient of ammonia decomposition in each step

In eq 1.4, the A is taken from Table 3.4, the E_a is taken from Table 3.2 and 4.3, R is the universal gas constant, and T is 293K for fitting with the fracture toughness test condition. Using eq 1.4, the reaction rate coefficient of NH_3 decomposition in each step can be calculated as shown in Table 4.8. The reaction rate coefficient of NH_3, NH_2, and NH is decreasing, which indicates that the reaction rate of NH_3 decomposition is decreasing and decreasing. When 1,000 vppm NH_3 competes with H_2, there is a great reduction in the reaction rate coefficient from NH_2 to NH, which demonstrates that the last step of NH_3 decomposition ($NH \rightarrow N + H$) is the slowest step, which is difficult to occur during the fracture toughness test. However, the first two decomposition steps ($NH_3 \rightarrow NH_2 + H$; $NH_2 \rightarrow NH + H$) are possible to occur during the test. However, when 10,000 vppm NH_3 competes with H_2, there is a great reduction in the reaction rate coefficient from NH_3 to NH_2, which demonstrates that although the last step of NH_3 decomposition ($NH \rightarrow N + H$) is still the slowest step, the $NH_2 \rightarrow NH + H$ already has a dramatic decrease of reaction rate, which is difficult to occur during the fracture toughness test. Thus, only the first decomposition step ($NH_3 \rightarrow NH_2 + H$) is possible to occur during the fracture toughness test.

Table. 4.8 Reaction rate coefficient k of NH_3 decomposition

	NH_3	NH_2	NH
k (1,000 vppm NH_3) (s^{-1})	1.36×10^{8}	7.28×10^{5}	2.13×10^{-1}
k (10,000 vppm NH_3) (s^{-1})	6.65×10^{8}	1.45×10^{-1}	1.98×10^{-2}

Theoretical results in section 4.4.2 showed that the hydrogen atom coverage on Fe (110) surface is increased with an increase in NH_3 concentration. However, the experiment results show a reversed trend, because, in reality, the NH_3 decomposition can achieve different steps during the fracture toughness test due to the reaction rate drop down. 1,000

vppm NH_3 competed with H_2, and the first two steps ($NH_3 \rightarrow NH_2 + H$; $NH_2 \rightarrow NH + H$) can occur, which can have 8.42% hydrogen atom coverage. On the other hand, 10,000 vppm NH_3 competed with H_2, only the first steps ($NH_3 \rightarrow NH_2 + H$) can occur, which can have 4.37% hydrogen atom coverage. As a result, the thematical result showed that increased NH_3 concentration increased hydrogen atom coverage on the Fe surface, while the fracture toughness showed the reverse result.

4.4.4 Reverse ammonia concentration effect on ammonia induced hydrogen embrittlement

As investigated in the chapter 3.4.3, the kinetic modeling of NH_3 has been established. Thus, based on the eqs 3.9, and 3.10, the coverage of adsorbed species on the Fe (110) surface in the Case A can be modified by Table 4.3 (relatively higher NH_3 concentration). The coverage of adsorbed species in the Case A is shown in Table 4.9.

Table 4.9 Adsorbed species coverage on Fe (110) in Case A

	Coverage (1000ppm NH_3)	Coverage (10,000ppm NH_3)
θ_{NH_3*}	9.51%	20.63%
θ_{NH_2*}	0.79%	2.18%
θ_{H*}	0.79%	2.18%

Based on the eqs 3.16 - 3.19, the coverage of adsorbed species on the Fe (110) surface in the Case B can be modified by Table 4.3 (relatively higher NH_3 concentration). The coverage of adsorbed species in the Case B is shown in Table 4.10.

Table 4.10 Adsorbed species coverage on Fe (110) in Case B

	Coverage (1000ppm NH_3)	Coverage (10,000ppm NH_3)
θ_{NH_3*}	3.00%	9.81%
θ_{NH_2*}	0.25%	1.04%
θ_{NH*}	3.80%	6.56%
θ_{H*}	4.06%	7.6%

Based on the eqs 3.26 - 3.30, the coverage of adsorbed species on the Fe (110) surface in the Case C can be modified by Table 4.3 (relatively higher NH_3 concentration). The coverage of adsorbed species in the Case C is shown in Table 4.11.

Table 4.11 Adsorbed species coverage on Fe (110) in Case C

	Coverage (1000 vppm NH_3)	Coverage (10,000 vppm NH_3)
θ_{NH_3*}	3.00%	9.81%
θ_{NH_2*}	0.25%	1.04%
θ_{NH*}	3.80%	6.56%
θ_{N*}	9.70×10^{-6}%	1.84×10^{-7}%
θ_{H*}	4.06%	7.60%

Based on the chapter 4.4.3 investigated, the theoretical results suggest hydrogen atom coverage on Fe (110) surface is increased with an increase in NH_3 concentration but experimental results suggest the other way. This happens because of dramatically drop in NH_3 decomposition reaction rate with an increasing NH_3 concentration. 1,000 vppm NH_3 competed with H_2, and the first two steps ($NH_3 \rightarrow NH_2 + H$; $NH_2 \rightarrow NH + H$) can occur, which can have 4.06% hydrogen atom coverage. On the other hand, 10,000 vppm NH_3 competed with H_2, only the first steps ($NH_3 \rightarrow NH_2 + H$) can occur, which can have 2.18% hydrogen atom coverage. As a result, the fracture toughness test result showed the reverse result compared with the theoretical result.

4.4.5 Future perspective

As described above, the effect of NH_3 mitigation and induction effect on HE has been characterized and the mechanism has been elucidated. However, it has been found that the *J*-Δa curve in H_2 + NH_3 ($V = 2.0\times10^{-3}$ mm/s) initially approaches to N_2 curve, but with crack propagation, the curve is close to H_2. The crack growth rate increased with crack propagation, and the crack opens were directly related to the crack growth rate. It is considered that insufficient NH_3 supply when the crack growth rate is high. Therefore, to further characterize the NH_3 effect on HE, it is necessary to conduct fatigue tests in the future. On the other hand, in this study, I investigated the process above the surface, which is the hydrogen coverage on the surface by Langmuir theory. However, HE also needed to consider the processing after hydrogen uptake, for example, hydrogen diffusion, fracture site, hydrogen concentration at the fracture site, and so on. Although there is no prediction equation of HE up to now, it is possible to link the hydrogen diffusion theory and Langmuir theory with the surface as the boundary. Therefore, establishing a predictive model of HE can be expected in the future by further investigation.

4.5 Conclusion

Fracture toughness tests of low-alloy steel SCM440 were conducted in H_2, N_2 mixed 1,000 vppm and 10,000 vppm NH_3 added H_2 and N_2 gas. To understand the mechanism of the NH_3 induction effect, the DFT calculations were also conducted. The main results achieved in this chapter are as follows:

1. According to theoretical results, as NH_3 concentration increased, the reaction rate of NH_3 decomposition ($NH_3 \rightarrow NH_2 + H$) increased, while the reaction rate of NH_3 decomposition ($NH_2 \rightarrow NH + H$; $NH \rightarrow N + H$) decreased. In particular, the reaction rate of the second step ($NH_2 \rightarrow NH + H$) decreased significantly. For the relatively lower concentration (1,000 vppm), NH_3 can achieve the first two steps for its decomposition when $V = 2.0 \times 10^{-5}$ mm/s. However, for the relatively higher concentration (10,000 vppm), NH_3 can only achieve the first step of its decomposition when $V = 2.0 \times 10^{-5}$ mm/s.

2. Under the testing condition is that H_2 + 1,000 vppm NH_3 environment and $V = 2.0 \times 10^{-5}$ mm/s, the NH_3 decomposition can reach two steps ($NH_3 \rightarrow NH_2+H$; $NH_2 \rightarrow NH+H$), and then the hydrogen atom coverage on Fe (110) surface was 8.42%. However, under the test conditions, H_2 + 10,000 vppm NH_3 and $V = 2.0 \times 10^{-5}$ mm/s, the NH_3 decomposition can reach the first step ($NH_3 \rightarrow NH_2+H$), and then the hydrogen atom coverage on Fe (110) surface was 4.37%. As a result, the fracture toughness test result that increased NH_3 concentration increased the J_{IC} value (47 N/mm → 87 N/mm) can be interpreted.

3. Under the testing condition is that N_2 + 1,000 vppm NH_3 environment and $V = 2.0 \times 10^{-5}$ mm/s, the NH_3 decomposition can reach two steps ($NH_3 \rightarrow NH_2+H$; $NH_2 \rightarrow NH+H$), and then the NH_3-derived hydrogen atom coverage on Fe (110) surface was 4.06%. However, under the test conditions, N_2 + 10,000 vppm NH_3 and $V = 2.0 \times 10^{-5}$ mm/s, the NH_3 decomposition can reach the first step ($NH_3 \rightarrow NH_2+H$), and then the NH_3-derived hydrogen atom coverage on Fe (110) surface was 2.18%. As a result, the fracture

toughness test result that showed increased NH_3 concentration increased the J_{IC} value (67 N/mm → 165 N/mm) with the increase of NH_3 concentration can be interpreted.

4.6 References

1. Staykov A., Komoda R., Kubota M., et al, Coadsorption of CO and H_2 on an Iron Surface and Its Implication on the Hydrogen Embrittlement of Iron. *The Journal of Physical Chemistry C*. Vol. 123, **2019**, pp. 30265 – 30273.
2. Somerday B. P., Sofronis P., Nibur K. A., et al, Elucidating the variables affecting accelerated fatigue crack growth of steel in hydrogen gas with low oxygen concentrations, *Acta Materials*, Vol. 61, **2013**, pp. 6153-6170.
3. Staykov A., Yamabe J., Somerday B. P., Effect of hydrogen gas impurities on the hydrogen dissociation on iron surface. *International Journal of Quantum Chem*istry, Vol. 114, **2014**, pp. 626-635.
4. Hermse G. M., Frechard F., et al, Combining density-functional calculations with kinetic models: NO/Rh(111), *Journal of Chemical Physics*, Vol. 118, **2003**, pp. 7081-7089.
5. Mafuné F., Bakker J. M., Kudoh S., Dissociative adsorption of NO introduces flexibility in gas phase Rh6+ clusters leading to a rich isomeric distribution, *Chemical Physics Letters*, Vol. 780, **2021**, pp. 138937.
6. John M. H., Ziegler T., Density Functional Theory and Kinetic Studies of Methanation on Iron Surface, *Journal of Physical Chemistry C*, Vol. 111, **2007**, pp. 11012-11025.

5. Conclusion

Creating a hydrogen society to protect the global environment is one of the promising solutions to reduce carbon dioxide emissions and promote the use of renewable energy. However, steel and alloy used for hydrogen gas containment can suffer from hydrogen embrittlement, and NH_3 can lead to the degradation of the material's mechanical properties. At the same time, it is considered a hydrogen carrier for the fuel cell. Therefore, NH_3 plays a critical role in hydrogen society. However, the mechanism of NH_3 mitigation and induction effect on HE was remain unclear based on the past study.

Considering this situation, the objective of this study is to characterize the mitigation and induction effect of NH_3 on the HE of the SCM440 low-alloy steel during a fracture toughness test and elucidate the mechanism by density functional theory. Practically, this study investigated the mechanism of NH_3 and H_2 competitive coadsorption on the Fe (110) surface.

The general conclusion derived from this thesis is that we clearly demonstrated the mechanism that NH_3 mitigated and induced HE depending on the test conditions. Theoretical study on the NH_3 effect of HE has great significance in Material Science and Mechanical Engineering when considering a safe carbon-neutral society that is provided by advanced hydrogen technologies. The conclusions of each chapter are as follows.

In Chapter 1, the motivation and societal relevance of this study are described based on the tendency of the hydrogen society and a survey of the past studies on NH_3 and the impurity mitigation effect on HE in hydrogen gas.

In Chapter 2, Fracture toughness tests of low-alloy steel SCM440 were conducted in an NH_3 added H_2 gas environment $V = 2.0\times 10^{-3}$ mm/s in order to characterize the effect of the NH_3 addition to H_2 gas on the HE. To understand the mechanism that NH_3 mitigated HE, the adsorption site, adsorption energy, the electron density, the reaction rate, and the

molecular coverage of NH_3 and H_2 were calculated by DFT and the Langmuir adsorption model. The main results achieved in this chapter are as follows:

1. The electron density of NH_3 on the Fe (110) surface was higher than that of H_2. Thus, the electronic interaction of the Fe (110) surface for NH_3 was higher than for H_2.

2. NH_3 was preferentially adsorbed on the Fe (110) surface because the reaction rate of NH_3 on the Fe (110) surface is significantly higher than H_2.

3. When coverage of NH_3 on the Fe (110) surface was 25.00%, the atomic hydrogen coverage on Fe (110) surface was 0.01%. In conclusion, preferentially adsorbed NH_3 can mitigate the HE at the loading rate was 2.0×10^{-3} mm/s in gaseous hydrogen by hindering hydrogen uptake.

In Chapter 3, Fracture toughness tests of low-alloy steel SCM440 were conducted in an NH_3 added N_2 gas environment in order to characterize the effect of the NH_3 itself on the HE. To understand the mechanism of the HE induction effect by NH_3, the whole processing of NH_3 decomposition on the Fe (110) surface was calculated by DFT. The main results achieved in this chapter are as follows:

1. The rate-limiting step of NH_3 decomposition is the reaction NH→N+H (11.11% NH_3 coverage), which has almost no contribution to hydrogen coverage on Fe (110) surface.

2. Compared with the NH_3 adsorption rate, the NH_3 decomposition rate was very slow. Therefore, NH_3 had no effect on HE at a relatively high loading rate, however, NH_3 significantly decreased fracture toughness and induced HE at a relatively low loading rate.

3. With 1 NH_3 adsorbed on 9 Fe (110) surface (11.11% NH_3 coverage), NH_3-derived hydrogen coverage on Fe (110) surface was 4.06% at a slower loading rate, thus, NH_3 induced the HE by its decomposition at the slower loading rate.

In Chapter 4, Fracture toughness tests of low-alloy steel SCM440 were conducted in H_2, N_2, 1,000 vppm, and 10,000 vppm NH_3 added N_2 and H_2 gas. To understand the mechanism of the NH_3 mitigation and induction effect, the DFT calculations were also conducted and kinetic modeling of competitive coadsorption between NH_3 and H_2 was established. The main results achieved in this chapter are as follows:

1. With NH_3 concentration increases, the reaction rate of NH_3 decomposition decreases. For the relatively lower concentration (1,000 vppm), NH_3 was stopped at NH→N+H of its decomposition. However, for the relatively higher concentration (10,000 vppm), NH_3 was stopped at NH_2→NH+H of its decomposition because the reaction rate of NH_3 decomposition $NH_2 \rightarrow NH + H$ was dramatically decreased with increased NH_3 concentration. Because increased NH_3 concentration results in fewer vacant sites on the surface for NH_3 decomposition, as a result, the activation energy barrier of NH_3 decomposition $NH_2 \rightarrow NH + H$ was increased.

2. Under the test conditions that $H_2 + NH_3$ and $V = 2.0 \times 10^{-5}$ mm/s, the hydrogen atom coverage on Fe (110) surface was decreased with increased NH_3 concentration because the NH_3 decomposition rate (NH_2→NH+H) was dramatically decreased, as a result, insufficient time for NH_3 further decomposition even NH_3 concentration was increased. Therefore, the fracture toughness test results showed that increased NH_3 concentration increased the J_{IC} value.

3. Under the test conditions that $N_2 + NH_3$ and $V = 2.0 \times 10^{-5}$ mm/s, the NH_3-derived hydrogen atom coverage on Fe (110) surface was decreased with increased NH_3 concentration because the NH_3 decomposition rate (NH_2→NH+H) was dramatically decreased, as a result, insufficient time for NH_3 further decomposition even NH_3 concentration was increased. Therefore, the fracture toughness test results showed that increased NH_3 concentration increased the J_{IC} value.

In Chapter 5, the general outline of this thesis is described.